PRECISION MEASUREMENTS OF THE MAGNETIC FIELD DEPENDENCE OF THE PENETRATION DEPTH IN YBCO: AN EXPERIMENTAL STUDY OF THE NONLINEAR MEISSNER EFFECT

By

Christopher Paul Bidinosti

B. Sc. (Physics) Brandon University, 1993

M. Sc. (Physics) University of British Columbia, 1995

A THESIS SUBMITTED IN PARTIAL FULFILLMENT OF

THE REQUIREMENTS FOR THE DEGREE OF

DOCTOR OF PHILOSOPHY

in

THE FACULTY OF GRADUATE STUDIES

DEPARTMENT OF PHYSICS AND ASTRONOMY

We accept this thesis as conforming

to the required standard

THE UNIVERSITY OF BRITISH COLUMBIA

October 2000

Department of Physics and Astronomy
The University of British Columbia
6224 Agricultural Road
Vancouver, B.C., Canada
V6T 1Z1

Date: December 19/2000

Abstract

Motivated by a well established body of theoretical work on the nonlinear Meissner state electrodynamics of type II superconductors, we have developed a high sensitivity ac susceptometer to measure the magnetic field dependence of the penetration depth λ in single crystal $YBa_2Cu_3O_{7-\delta}$. The susceptometer is capable of measuring changes in the penetration depth in typical sized crystals to within a few tenths of an Angstrom. This represents a significant increase in the resolution of such a device, and offers increased functionality over superconducting microwave resonators in its ability to measure $\Delta\lambda$ as a function of field as well as temperature. In addition, we have developed appropriate procedures to ensure that our field dependent measurements remained free of unwanted magnetic flux penetration into the sample, and that subsequent results represented the intrinsic nonlinear Meissner response of the sample. This has allowed us to test present ideas about the nature of high temperature superconductivity through an accurate comparison of $\Delta\lambda(H)$ measurements with theory.

In particular, the theory predicts that a d-wave superconductor will exhibit a field dependent penetration depth that is linear in field near $T = 0$ and crosses over to a weak quadratic field dependence with increased temperature. Furthermore, the magnitude of this effect should depend on the direction of the applied field with an anisotropy that reflects the symmetry of both the superconducting order parameter and the crystal structure.

Measurements presented in this thesis were made on three high quality single crystals of $YBa_2Cu_3O_{7-\delta}$. In all cases, the field dependence of the penetration depth could not be described in full by the theory of the Nonlinear Meissner Effect. The anisotropy seen in

$\Delta\lambda(H)$ may be a result of the orthorhombic crystal structure and the strong anisotropy in the zero temperature, in-plane penetration depth $\lambda_{a,b}(0)$, and as such *may* be consistent with theory. However,theory also predicts a strong suppression of $\Delta\lambda(H)$ with increasing temperature, in stark constast to the measurements which show a small increase.

We believe the $d_{x^2-y^2}$ symmetry of $YBa_2Cu_3O_{7-\delta}$ to be well established by other experiments, and do not think that our results represent evidence contrary to this fact. Rather, it is our contention that present theories of the Nonlinear Meissner Effect simply do not describe in full the nonlinear behaviour of the penetration depth in a d-wave superconductor. Our results are also compared with a very recent idea of a field induced gap suppression in a d-wave superconductor; this theory showed some success in its ability to correctly predict the direction in which $\Delta\lambda(H)$ evolves with temperature. We also show that there is evidence for a possible c-axis contribution to $\Delta\lambda(H)$. Overall, at present there appears to be no single theory that can explain the field dependence of the penetration depth measured here for $YBa_2Cu_3O_{7-\delta}$.

Table of Contents

List of Tables

List of Figures

Preface

In the fall of 1992, S.K. Yip and J.A. Sauls published a paper entitled *Nonlinear Meissner Effect in CuO Superconductors.* It was a theory paper proposing experiments based on the nonlinear effects of an applied magnetic field on the Meissner state supercurrent that would differentiate between s-wave and d-wave superconductors.[1] This is discussed at much greater length in Chapter 3, along with the several theoretical ideas that have built on the original work. Throughout the entire thesis I reserve the term the Nonlinear Meissner Effect (NLME) to refer specifically to the Yip and Sauls theory and all the subsequent extensions of this theory as described in Chapter 3. The unifying concept between these theories is the quasi-particle energy shift as the origin for nonlinearities that arise in Meissner state electrodynamics. Of course, it is entirely accurate to say that any field dependent Meissner state penetration depth is by definition a *nonlinear Meissner effect*, and there is another theory (to be discussed in Chapter 6) that suggests a different mechanism (from Yip and Sauls) for how it could come about. As it stands, there is no clear explanation for the $\Delta\lambda(H)$ we have measured in $YBa_2Cu_3O_{7-\delta}$ in this thesis, so I let the original theory remain as *the* Nonlinear Meissner Effect and leave it for future researchers in this area to decide who ultimately gets this title.

In Chapters 1 and 2, I review basic concepts of superconductivity, introduce the high-T_c compound YBCO, and discuss the linear local electrodynamics that should precede the topic of nonlinear electrodynamics. This will certainly be a review for many people who

[1]The debate over the symmetry of the pairing state in the cuprate superconductors was still raging at that time, and the theory of Yip and Sauls showed that a shift in quasi-particle energies due to the applied magnetic field would give rise to a field dependent penetration depth (among other things) that would be depend uniquely on the nature of the pairing.

read this thesis, but I hope it will give those unfamiliar with the topic a reasonable feel for what superconductivity is all about. With regard to the introduction in Chapter 1, I tried hard not to sound like every other introduction I have ever read about superconductivity. But the truth of the matter is that superconductivity in itself is far more interesting than the history of our knowledge of it, and there is precious little that one can do to spice this up. So I didn't. One might also notice in these two chapters that I exclusively showed microwave data originating from our lab. My primary reason for doing this: a souvenir. I want to keep for myself some account of what my friends were up to in the lab. This may appear to be rather unscientific, but I am vindicated by the fact that this data also happens to represent some of the best measurements of the linear, low frequency electrodynamics in high-T_c superconductors. Any reader serious about this subject will find the field well documented within the few references I present.

Chapters 4 and 5 described the ac susceptometer and the measurement techniques used in this thesis. This represents only the pleasant details of success that followed a very long struggle to develop an instrument sensitive enough to measure very small changes in the penetration depth as a function of magnetic field. There were in fact four versions of the ac susceptometer built over a four year period. It also took another year after that to work the kinks out of the experiment and to get some good data. By this time, the original impetus for studying the Nonlinear Meissner Effect had passed; several other experiments had convincingly shown that the cuprates were indeed d-wave superconductors. However, the superconducting mechanism is still not known for these materials, so any experiment that can provide any information about the way they behave is certainly worth doing. I look forward to seeing how it all turns out one day.

Acknowledgement

It has been an enjoyable and very interesting seven years in Vancouver, and there are many people I would like to thank for having made this such a wonderful experience for me.

Physics was a big part of that seven years, and I've enjoyed very much the opportunity I've had to explore superconductivity at such a fundamental level. For this I thank, first and foremost, my supervisor, Dr. Walter Hardy. His knowledge of physics is astounding, and he's always willing to share what he knows. With great patience too! He is also a very caring and generous supervisor, which made grad student life much more pleasant. It was always a great relief to know that your supervisor would look out for you, and would keep your best interests in mind. Thanks again, Walter.

I also want to thank Doug Bonn and Ruixing Liang. In a way, I had three great supervisors, who would always answer my questions and pass along their knowledge of physics. I thank Beat Meyer and Phil Akers in the machine shop for their help in the building and design of parts of the susceptometer. And I really want to thank my labmates throughout the years: Pinder Dosanjh, Saeid Kamal, Pat Turner, Ahmad Hosseini, Richard Harris, Rob Knobel, Kuan Zhang, Andre Wong, Kaspar Mossman, Bruce Gowe, Yonas Bisrat, Marty Kurylowicz, and Darren Peets; I thank them for their friendship and for all the assistance they have given me.

I would like to thank the Natural Science and Engineering Research Council and the Canadian Institute for Advance Research for their financial support. A special note of gratitude must be given to the CIAR for their strong support of superconductivity research in Canada, especially the summer school program. I was fortunate to attend the

superconductivity summer school several times between 1996 and 2000. It was a great place to exchange ideas and meet fellow students from across the country.

From the greater physics community, I would like to acknowledge the assistance of Stephen Julian (for the low temperature transformers), and Peter Hirschfeld (for sending us code for the numerical solution of his theory). I also appreciate the discussions with Thomas Dahm, Doug Scalapino, Jim Sauls, Oriol Valls, and Klaus Halterman.

Physics has been a big part of my life, but physics isn't everything. There are, in fact, more people outside this circle to whom I owe credit for this thesis than those directly involved. Without all the support from family and friends, this would have been a much larger task. And without all the laughs and smiles that I shared with family and friends, this certainly would have been an unbearable task. So, thanks be to: my parents, Rudy and Rosemarie; my siblings Raeleta (& Ken, Katrien, Rebecca, and Abby), Anna (& Chris, Robyn, Jordan, and Benjamin), Angela (& Lancer), Michael, and Lisa - thanks Mom, Dad and Ange for coming to my PhD defense; Susan and Wayne for taking me in when I arrived in Vancouver; the Chaboyers for Christmas, Easter, and Thanksgiving dinners; my friends, Bruce and Jon, Saskia, Pat and Holly, Cam (& the friends we've met through 4130 Blenheim St. - Sabrina, Abby, Shari, Orrin, Brad...); my UBC friends (Anna, Paul, Hash, Christian...); my Brandon friends (too many to mention); Dan and the book club; and San, Edge and Ol' Yeller (our '72 VW Westfalia purchased with the assistance of NSERC). And I must thank my grandfather, Romeo Bidinosti, for instilling in me a sense of wonder and curiosity about the world. I took to heart his advice that one learns more by walking different paths (even if that did mean carrying his suitcase through San Daniele.)

Chapter 1

Introduction

When telling a story, it is generally easiest to just start at the beginning. For superconductivity, the story began in 1911 with Heike Kamerlingh-Onnes, who discovered that the dc electrical resistance of mercury sharply dropped to zero at some critical temperature T_c [1]. This *perfect conductivity* may be the most well known and most sought after property of a superconductor, but it alone does not define superconductivity; a superconductor also exhibits *perfect diamagnetism* in the presence of a small magnetic field. This property was discovered by W. Meissner and R. Ochsenfeld in 1933 [2]; known as the Meissner Effect it distinguishes superconductivity as a phenomena quite disparate from just the absence of electrical resistance. In 1935, the brothers Fritz and Heinz London were able to set down two equations that describe the macroscopic electrodynamics of superconductors [3], and despite the fact that they were derived from purely classical considerations, there exists in the London Equations a subtle suggestion that superconductivity is in fact a quantum phenomenon. Twenty-two years later John Bardeen, Leon Cooper and J. Robert Schrieffer showed this to be true, and provided a microscopic explanation of conventional superconductivity (BCS theory) [4] that was based on the instability at the Fermi Surface caused by phonon mediated attraction between electrons.

The nearly fifty years between the first observation of superconductivity and the development of a successful theory to explain it epitomizes human resolve to learn the secrets of an often reticent universe. It also seems that the greater the mystery the more intent we become on discovery, and if the Nobel Prize can be used as a measure of that intrigue then there is little doubt that superconductivity has always caught our attention. In 1913, Kamerling-Onnes received the award (for his work on low temperature physics including superconductivity), as eventually did Bardeen, Cooper and Schrieffer in 1972. The following year it was Brian Josephson and Ivar Giaever for their work on tunneling in superconductors [5, 6], and in 1987, J. Georg Bednorz and K. Alexander Müller became Nobel recipients for their discovery, just one year prior, of superconductivity at 35 K in the compound $La_{2-x}Ba_xCuO_4$ [7].

This discovery touched off an explosion of research in the area of high temperature superconductivity. Before 1986, the highest known T_c was 23 K in the compound Nb_3Ge, but by the start of 1987 superconductivity was discovered above 90 K in $YBa_2Cu_3O_{7-\delta}$, and by the following year at temperatures in excess of 100 K in compounds such as $Bi_2Sr_2Ca_2Cu_3O_{10}$ and $Tl_2Ba_2CaCu_2O_8$.[1] These high temperature superconductors are all characterized by the presence of CuO_2 planes, which has garnered them a more succinct name, the cuprates. It is in fact a cuprate, $HgBa_2Ca_2Cu_3O_{8+\delta}$, that presently holds the record for the highest T_c, about 160 K under pressure, and while the push to find compounds with even higher transition temperatures has presently stalled, a massive experimental and theoretical research effort to understand the cuprates still continues. Much has been learned about these materials in the last fourteen years - in some aspects they show the conventional traits of BCS superconductivity, while in others they appear to be quite unconventional - but a successful explanation for how they come to superconduct is still missing. The greatest certainty right now is that once again our curiosity has been captured by the strange phenomena of superconductivity.

[1]See the handbook by Poole [8] for an extensive reference on superconducting materials, and their transition temperatures and other physical parameters.

1.1 Superconductivity Basics

Perfect diamagnetism implies that the ground state of a superconductor in a magnetic field is one where the magnetic field in the interior of the superconductor is equal to zero. This is achieved by currents that flow just inside the surface of the superconductor and produce a magnetic field that precisely cancels the applied field within the bulk of the material. The length scale over which these currents exist, and the total field is driven to zero, is set by a material specific parameter known as the penetration depth λ. Another important length scale is the coherence length ξ, which can be thought of as the size of the wavepacket of the superconducting charge carriers (after Pippard [9]), or in a related notion as the length over which the ordered state of superconductivity reaches its full value (after Ginzburg and Landau [10]). The size of the coherence length is also specific to a given superconductor.

The phenomenological theory of Ginzburg and Landau expresses the free energy of a superconductor in terms of a complex order parameter that has a magnitude related to the density of superconducting electrons. The Ginzburg-Landau parameter $\kappa = \lambda/\xi$ sets the dividing line between two distinct types of superconductor: a superconductor with κ less than $1/\sqrt{2}$ is considered type I; type II if $\kappa > 1/\sqrt{2}$. For a type I superconductor in a magnetic field, it is energetically unfavorable to remain in the superconducting state when the field reaches some thermodynamic critical value H_c, and the system exits the flux free Meissner state and becomes normal.[2] In contrast, a type II superconductor finds it can keep a lower energy by letting the field enter its bulk slowly, starting at a lower critical field $H_{c1} < H_c$, and is only driven normal at some upper critical field $H_{c2} > H_c$. A type II superconductor is said to be in the mixed or vortex state when $H_{c1} < H < H_{c2}$, and the field enters the sample in *tubes* or *vortices* of quantized flux $\Phi_o = h/2e$. The

[2] This discussion ignores shape dependent effects of real superconductors.

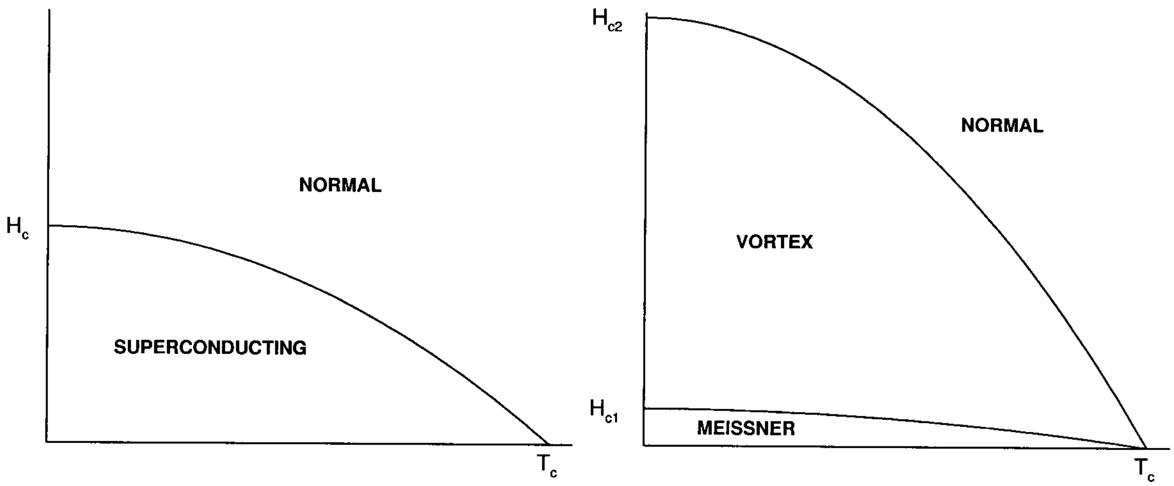

Figure 1.1: The phase diagram, H versus T, for type I (left) and type II (right) superconductors.

phase diagram, magnetic field versus temperature, for both types of superconductor is shown in Figure 1.1.

The factor $2e$ in the flux quantum points to the fact that electron pairs actually comprise the superconducting charge carriers. This charge quantity, well known from BCS theory, is also apparent in the tunneling effects predicted by B.D. Josephson [5]. He showed that the superconducting current that would tunnel through a barrier (junction) between two superconductors was given by $j = j_c \sin(\Delta\phi)$, where $\Delta\phi$ is the phase difference between the two. If, in addition, there is a voltage V applied across the junction, the current oscillates at a frequency that is proportional to the charge of this electron pair and is given by $\omega = 2eV/\hbar$.

Prior to BCS, pairing was hinted at experimentally by far-infrared and specific heat measurements. Results from these experiments could only be consistent with one another if the former was considered to be a measure of the energy needed to break apart a pair of electrons and the latter a measure of the energy per single constituent of a broken pair [11, pp. 8-9]. At about that same time, Cooper [12] was able to show theoretically that two electrons, in the presence of a *Fermi-sea* of other electrons, would in fact form a bound pair (or Cooper pair) for any finite attractive interaction. In a generalization of Cooper's idea, BCS theory [4] had each electron playing the dual role of (1) restricting the available momentum states to the other electrons, *i.e.* being a part of the *Fermi-sea*, and (2) participating in a bound state as part of the $N/2$ set of Cooper pairs[3] that form to lower the energy of the system. A BCS wave function describing the entire state is constructed from $N/2$ two-electron wavefunctions, each of which must be antisymmetric (as is the overall wavefunction) to comply with the Pauli exclusion principle. The main consequence of BCS pairing is the formation of an energy gap Δ_k, and an excitation spectrum $E_k = \sqrt{\epsilon_k^2 + \Delta_k^2}$, where the energy E_k is referenced with respect to the Fermi surface (which corresponds to $\epsilon_k = 0$).

In the original theory, the attractive potential required for pairing arises from electron interactions with the lattice. This had been shown by the *isotope effect* [13], which was a correlation between T_c and isotope mass for a given element, and suggestively linked superconductivity with phonons. BCS also chose the two-electron wavefunctions to be a singlet state (*i.e.* opposite spins for the pair) and the energy gap to be isotropic (*i.e.* independent of k, see Figure 3.1). This theory, with few modifications, was sufficient to describe all known superconductors until the 1980's.

1.2 YBCO and High Temperature Superconductivity

The crystal structure of the most studied high-T_c compound, $YBa_2Cu_3O_{7-\delta}$ (YBCO), is shown in Figure 1.2, and displays the sheets of copper and oxygen (CuO_2 planes) that are common to all the cuprates. The superconductivity occurs in these sheets, and

[3]The coherence length from BCS theory can be thought of as the spatial extent of the Cooper pairs.

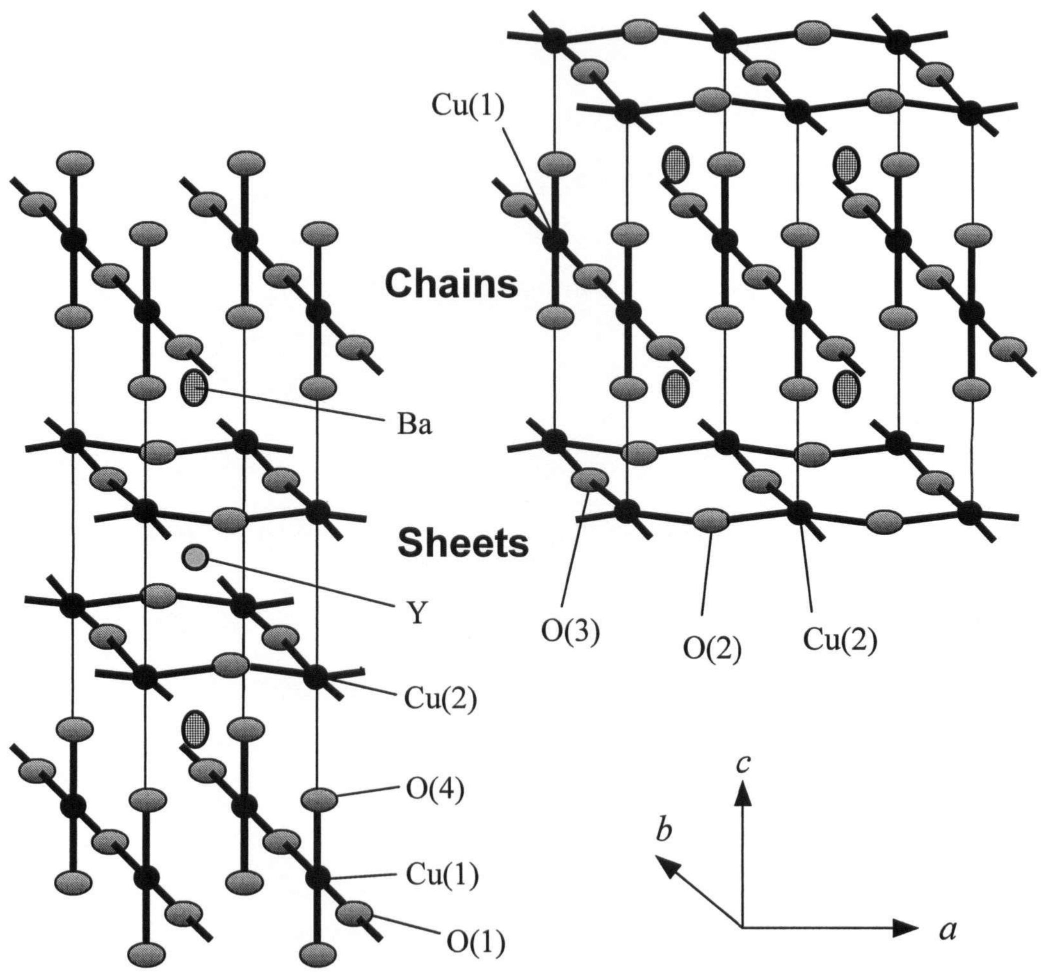

Figure 1.2: The lattice structure of $YBa_2Cu_3O_7$ (courtesy of R. Liang). The planes (or sheets) of CuO_2 are formed by the copper sites Cu(2) and oxygen sites O(2) and O(3). The CuO chains are comprised of sites Cu(1) and O(1). The chain and plane layers are separated by the BaO layer containing the apical oxygen site O(4); adjacent plane layers are separated by a layer of Yttrium. The O(1) oxygens dope the CuO_2 layers with *holes* by changing the oxidation state of the Cu(2) coppers from Cu2+ to Cu3+. A minimum occupation of O(1) sites is required for hole doping of the layers (and hence superconductivity) to occur. Below this, all Cu(2) coppers are in Cu2+ state, and their unpaired spins order antiferromagnetically.

can often be treated as a 2-dimensional phenomenon. Unique to YBCO are the chain layers of copper and oxygen (CuO) that run along the b-axis. The presence of these chains is often an added complication to sorting out the physics behind high temperature superconductivity. However, this material has its own merits, and unlike most cuprates, such as the commonly studied $Bi_2Sr_2Ca_1Cu_2O_y$ (BSCCO), the cations (Y, Ba, and Cu in this case) have a fixed ratio and do not substitute for each other. This allows one to grow very high purity samples of YBCO that have exceptionally good crystalline qualities, and this ultimately provides an advantage to which YBCO owes its popularity.

Another common feature of the cuprate superconductors is that they are often formed by the *doping* of a parent compound that is initially an insulating antiferromagnet. For example, in the original high-T_c compound, $La_{2-x}Ba_xCuO_4$ discovered by Bednorz and Müller, La_2CuO_4 is doped with Ba and first becomes superconducting at a concentration of $x = 0.05$ [8]. The generic phase diagram (temperature versus doping concentration) for the cuprates is shown in Figure 1.3: the transition temperature of the antiferromagnetic phase (AF) drops quickly with doping; farther along, the superconducting phase (SC) appears and has a peak transition temperature at some optimal doping level. The dashed line in Figure 1.3 identifies a region known as the pseudogap (PG), which is associated with a sort of pre-pairing of electrons that occurs well before the onset of superconductivity [14]. The remainder of the phase diagram is labelled as the normal state (N), in analogy with conventional superconductivity, where a normal (well understood) metal exists at temperatures above T_c. In the cuprates, however, the *normal* state is far from being normal; in particular, it exhibits a linear resistivity along the a and b-axes that exists over a very large temperature range, and a c-axis resistivity that appears to be anything but metallic [15].

The triumph of BCS theory came about partially through a good understanding of the normal state properties of conventional superconductors, and it is clear that a similar

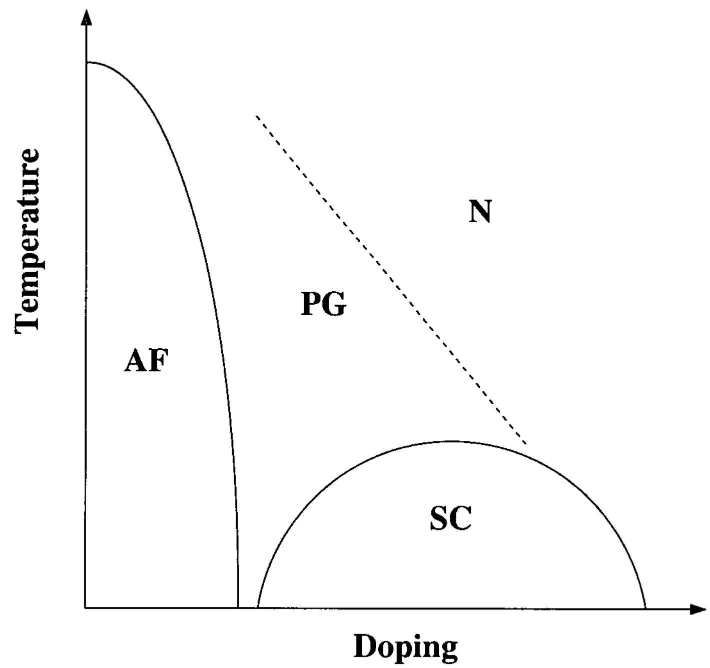

Figure 1.3: Generic phase diagram of the high temperature superconductors.

understanding of the cuprate phase diagram will also be crucial to the determination of the mechanism for high temperature superconductivity. Also, from this point of view, the puzzle of superconductivity is more correctly seen as a sub-problem of the larger issue of systems of stongly correlated electons. For conventional superconductivity, the normal metallic state could be understood as a Fermi-liquid - a collection of quasiparticles, subject to the Pauli exclusion principle, that behave essentially as independent electrons albeit with an effective mass m^* not necessarily equal to the bare electron mass. However, it is becoming clear in condensed matter physics that a collection of electrons in a solid more often than not behaves in a manner that is much, much different from just the sum of its parts. The cuprate phase diagram is a prime example of this. As the single doping parameter is tuned, the system passes through a rich array of very different types of behaviour: antiferromagnetic insulator, strange *metal*, superconductor.

In several cuprates, including YBCO, the doping level is determined by the oxygen content (as discussed in the caption of Figure 1.2), and can be altered subsequent to crystal growth. For example, in YBCO, whose stoichiometry can be equivalently written as $YBa_2Cu_3O_{6+x}$, the oxygen content in the chain layer can be set to a specific level by annealing at an appropriate temperature and oxygen partial pressure [16]. Superconductivity first appears at $x \simeq 0.33$ [8], and optimal doping at $x \simeq 0.91$ gives a maximum T_c of 93.7 K [17]. At $x = 1$, there are no oxygen vacancies in the chains, as shown Figure 1.2, the T_c is about 88 K and the system is said to be *slightly overdoped.* There is also a structural change with doping, the YBCO lattice goes from tetragonal to orthorhombic at $x \simeq 0.3$.

In terms of the superconducting state, some very important facts about the cuprates have been learned so far. The observation of the $2e$ flux quantum Φ_o, the presence of the ac Josephson effect and the results of several other experiments have all provided conclusive evidence for the usual formation of Cooper pairs in a spin singlet state [18] [11, p. 374]. The form of the orbital part of the pairing wave function remained a contentious issue for quite some time, but there is now almost universal consensus that the cuprates exhibit d-wave pairing and not the s-wave pairing of conventional superconductors.[4] In particular, the cuprate pairing state (or order-parameter) has $d_{x^2-y^2}$ symmetry, and changes sign in the ab-plane as $\cos 2\theta$, where θ is measured from the axes; this is quite unlike the conventional s-wave state which is isotropic.

The strongest evidence for the $d_{x^2-y^2}$ state came from Josephson junction experiments, which directly reflect the sign change in the order parameter. Most notable were the double junction rings comprised of single sections of conventional and cuprate superconductor [19], and the bi and tri-crystal junctions comprised of single cuprate rings

[4]The names for the different pairing states have been adopted from analogy with the well known electronic orbital symmetries of hydrogen.

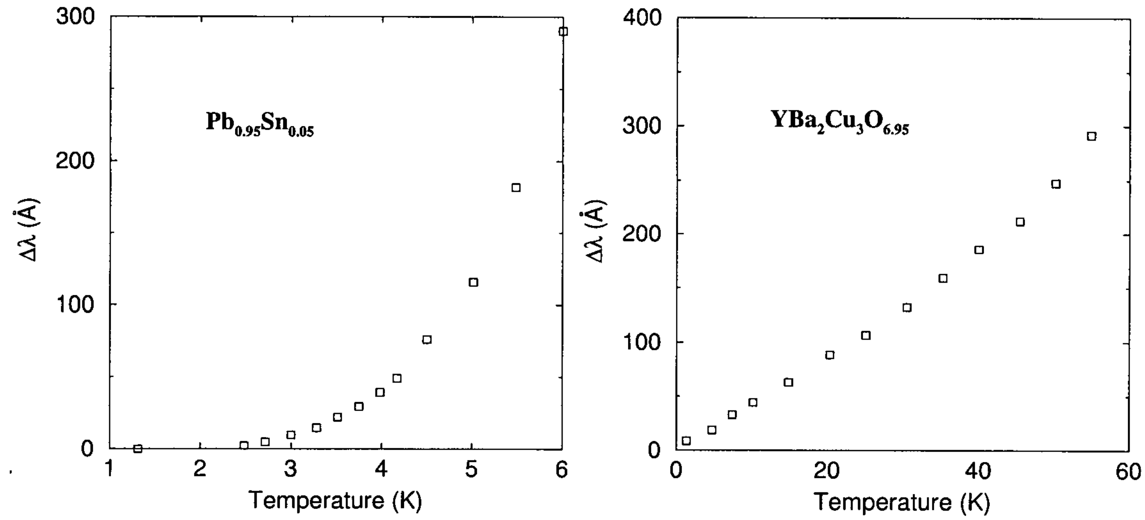

Figure 1.4: The temperature dependence of λ in an s-wave ($Pb_{0.95}Sn_{0.05}$) and d-wave ($YBa_2Cu_3O_{6.95}$) superconductor (from Hardy *et al.* [22]).

that had two (and three) sections with different crystalline orientation [20]. For each of these experiments, the characteristics of the flux within the ring could only be explained if the phase of the cuprate order-parameter had the $d_{x^2-y^2}$ symmetry.

Slightly less direct evidence for d-wave pairing can also be found in experiments that measure the energy gap of the superconductor through its excitations.[5] The energy gap reflects the symmetry of the pairing state, so for an s-wave superconductor the gap is finite and isotropic, and quite distinct from the d-wave gap which goes to zero at four nodes at angles $\theta = (2n+1)\pi/4$ (see Figure 3.1). A consequence of these nodes is the existence of low lying states in the excitation spectrum. The measurements by Hardy *et al.* [22] of the temperature dependence of the penetration depth in YBCO provided some of the first evidence for the presence of these nodes. Their results are shown in Figure 1.4

[5]A very thorough review of the different experimental tests of the pairing symmetry in cuprate superconductors can be found in Reference [21].

for both $YBa_2Cu_3O_{6.95}$ and the conventional superconductor $Pb_{0.95}Sn_{0.05}$. In both supercondutors, λ increases with temperature signaling a reduction in its ability to screen fields as Cooper pairs are lost to the excitations. However, the temperature dependence of $\Delta\lambda$ is significantly different between the two. In $Pb_{0.95}Sn_{0.05}$ the response is thermally activated going as $e^{-\Delta/T}$ (a consequence of the finite gap), while in $YBa_2Cu_3O_{6.95}$ the low lying states are accessible at all temperatures, which gives rise to the characteristic linear $\Delta\lambda(T)$ of a d-wave superconductor.

Chapter 2

Microwave Electrodynamics of Superconductors

The hallmark properties of superconductivity are a vanishing dc resistivity and an essentially perfect diamagnetism, so it is of little surprise that research on the electrodynamics of superconductors has always been important. In particular, the response to low frequency fields is a good probe of the superconducting energy gap and its excitations, which ultimately provides information on the pairing state of the electrons. This is of great importance in the high-T_c superconductors where the mechanism for pairing is still unknown. In this case, it also turns out that the properties of these materials create particular difficulties for other research methods traditionally used to study excitations in superconductors. For example, tunneling measurements are made difficult by a short coherence length, and the high temperatures involved introduce strong phonon contributions to the thermal conductivity, ultrasonic attenuation, and heat capacity [23]. On the other hand, with respect to charge transport, the small coherence length ensures local electrodynamics[1] (which makes interpretation of results rather straight forward), and the presence of phonons is not of immediate experimental concern. This leaves a niche in the high-T_c research effort that has been particularly well filled by microwave measurements using cavity perturbation.

In this Chapter, a quick review will be given of the low frequency, local, linear electrodynamics needed to understand the basics of the microwave measurements; some data

[1] In certain directions the coherence length can become quite large, and nonlocal effects may become important at very low temperatures (see Section 3.4.2). For the ensuing discussion, however, only the local limit will be considered.

from the literature will also be shown. This serves several purposes in this thesis. It gives a suitable background for the nonlinear electrodynamics to be described in Chapter 3, and by showcasing the success of the microwave research effort, provides a credible basis for pushing ahead and looking at the higher order nonlinear effects. To a certain degree, it also provides a yardstick by which experimental progress on the Nonlinear Meissner effect can be gauged.

2.1 Electrodynamics at a Conducting Boundary

Maxwell's equations written as

$$\begin{aligned} \nabla \cdot \boldsymbol{D} = \rho \qquad \nabla \times \boldsymbol{E} = -\frac{\partial \boldsymbol{B}}{\partial t} \\ \nabla \cdot \boldsymbol{B} = 0 \qquad \nabla \times \boldsymbol{H} = \frac{\partial \boldsymbol{D}}{\partial t} + \boldsymbol{J} \end{aligned} \tag{2.1}$$

are sufficient to describe linear macroscopic electromagnetic phenomena. Electromagnetic fields in homogeneous, linear media with conductivity σ and zero free charge ($\rho = 0$) are governed by the following wave equations

$$\begin{aligned} \nabla^2 \boldsymbol{E} &= \mu\epsilon \frac{\partial^2 \boldsymbol{E}}{\partial t^2} + \mu\sigma \frac{\partial \boldsymbol{E}}{\partial t} \\ \nabla^2 \boldsymbol{B} &= \mu\epsilon \frac{\partial^2 \boldsymbol{B}}{\partial t^2} + \mu\sigma \frac{\partial \boldsymbol{B}}{\partial t} \\ \nabla^2 \boldsymbol{J} &= \mu\epsilon \frac{\partial^2 \boldsymbol{J}}{\partial t^2} + \mu\sigma \frac{\partial \boldsymbol{J}}{\partial t} \end{aligned} \tag{2.2}$$

which are easily derived from Equations 2.1 along with the empirical relations $\boldsymbol{J} = \sigma \boldsymbol{E}$, $\boldsymbol{D} = \epsilon \boldsymbol{E}$, and $\boldsymbol{B} = \mu \boldsymbol{H}$. The coefficients ϵ and μ are the permittivity and permeability respectively and, like σ are specific to the given medium and independent of $\boldsymbol{E}$ and $\boldsymbol{B}$ at low excitation levels.

For harmonically oscillating fields, the coefficients of the two terms on the right hand side of Equations 2.2 become $-\mu\omega^2\epsilon$ and $i\mu\omega\sigma$. For a good conductor, $\sigma >> \epsilon\omega$ up to optical frequencies ($\omega \sim 2\pi \times 10^{14}$ Hz), so that in the microwave range ($\omega \sim 2\pi \times 10^{10}$ Hz) it is a very good approximation to ignore the first term allowing Equations 2.2 to be rewritten in the form

$$\nabla^2 \boldsymbol{B} = i\mu\omega\sigma\boldsymbol{B} \tag{2.3}$$

The solution of this differential equation depends in detail on the boundary conditions present. A simple, but very informative case to present is that of a semi-infinite conductor in a uniform applied magnetic field of amplitude $\mathrm{B_o}$. If the conductor is considered to occupy the positive z half-space, and the direction of $\boldsymbol{B}$ is chosen along the y-axis, then by Equation 2.3 the field inside the conductor will depend on z as

$$\boldsymbol{B} = \mathrm{B_o} e^{-\gamma z}\, \hat{\jmath} \tag{2.4}$$

with the complex propagation constant $\gamma = \sqrt{i\mu\omega\sigma}$. The amplitude of the electric field $\boldsymbol{E}$ and current density $\boldsymbol{J}$ have an identical dependence on z inside the conductor, but with direction parallel to the x-axis.

From Equation 2.4 it is clear that a finite real component of γ will lead to an exponential decay of the applied fields (and current density) within the conductor. This will be shown explicitly in the following section for a good conductor, as well as for a superconductor. However, it is convenient for the purpose at hand to first develop the concept of a *surface impedance* Z_s. By analogy with the familiar impedance ($Z = V/I$) experienced by a current flowing through the bulk of a wire, Z_s is associated with currents that, because of the spatial damping described by Equation 2.4, only flow near the surface of the conductor. Here, the definition of impedance is the ratio of the tangential electric and magnetic fields at the surface of the material [24], so for the geometry specified above, $Z_s = \mathrm{E}_{ox}/\mathrm{H}_{oy}$. This may be re-written in terms of σ and ω by replacing

E_o with J_o/σ and recognizing that in this case $dH/dz = J$, and therefore by integration $H_o = J_o/\gamma$. Substitution gives a useful definition for the surface impedance:

$$Z_s = \frac{\gamma}{\sigma} = \sqrt{\frac{i\mu\omega}{\sigma}} \tag{2.5}$$

Separating Z_s into real and imaginary parts gives

$$\begin{aligned} Z_s &\equiv R_s + i\,X_s \\ &= \mathrm{Re}\left\{\sqrt{\frac{i\mu\omega}{\sigma}}\right\} + i\,\mathrm{Im}\left\{\sqrt{\frac{i\mu\omega}{\sigma}}\right\} \end{aligned} \tag{2.6}$$

and defines a surface resistance R_s and a surface reactance X_s that respectively characterize energy loss and energy storage in the surface current.

2.2 Complex Conductivity - The Drude Model

To fully unveil the behavior of electromagnetic fields inside a conductor, μ and σ must be known. Most metals are only weakly magnetic, so it is suitable to replace μ with μ_o except in the case where the material is ferromagnetic. A useful form for the conductivity can be developed through the simple Drude Model, which considers the equation of motion of an electron in an applied electric field:

$$m\dot{\boldsymbol{v}} = -m\boldsymbol{v}/\tau - e\boldsymbol{E} \tag{2.7}$$

The damping term $-m\boldsymbol{v}/\tau$ characterizes the electrical resistance through τ, the relaxation time or scattering time, which is the average interval between scattering events for the electron within the conductor. Solving Equation 2.7 for a steady state driving force $-e\boldsymbol{E}e^{i\omega t}$, noting that the total current density $\boldsymbol{J} = -en\boldsymbol{v}$ where n is the electron density, gives

$$\boldsymbol{J} = \frac{ne^2\tau}{m}\frac{1 - i\omega\tau}{1 + \omega^2\tau^2}\boldsymbol{E} \tag{2.8}$$

The complex conductivity is identified as

$$\sigma(\omega) \equiv \sigma_1 - i\sigma_2 = \sigma_o \frac{1 - i\omega\tau}{1 + \omega^2\tau^2} \tag{2.9}$$

with real and imaginary parts

$$\sigma_1 = \sigma_o \frac{1}{1 + \omega^2\tau^2} \tag{2.10}$$

$$\sigma_2 = \sigma_o \frac{\omega\tau}{1 + \omega^2\tau^2} \tag{2.11}$$

and a dc conductivity $\sigma_o = ne^2\tau/m$.

Two relevant concepts, the skin depth in normal metals and the penetration depth in superconductors, fall neatly from the Drude Model conductivity with the appropriate choice of τ. For normal metals, dc resistivity measurements show typical relaxation times of order $10^{-14} - 10^{-13}$ seconds [25, p. 10]. At microwave frequencies then, $\omega\tau \ll 1$ and $\sigma \simeq \sigma_1$ is predominantly real. Recognizing that $\sqrt{i} = (i+1)/\sqrt{2}$, the magnetic field inside the metal, from Equation 2.4, becomes

$$\mathrm{B} = \mathrm{B}_o e^{-z/\delta} e^{-iz/\delta} \tag{2.12}$$

and it is clear that the amplitude of the field decays exponentially from the surface on a length scale given by the skin depth δ, where

$$\delta = \sqrt{\frac{2}{\mu_o \omega \sigma_1}} \tag{2.13}$$

In a normal metal the surface resistance and reactance are equal:

$$R_s = X_s = \sqrt{\frac{\mu_o \omega}{2\sigma_1}} = \frac{\mu_o \omega \delta}{2} \tag{2.14}$$

At low temperatures, where in some metals τ can become a few orders of magnitude larger, $\omega\tau$ is no longer insignificant and the contribution from σ_2 cannot be ignored. In the extreme case of a superconductor, zero dc resistivity and the existence of permanent currents implies perfect conductivity, ie. $\tau \to \infty$. In this case,

$$\sigma = \frac{ne^2}{m}\left(\frac{\pi}{2}\delta(\omega) - \frac{i}{\omega}\right) \tag{2.15}$$

and is purely imaginary at finite frequency.[2] Substitution into Equations 2.3 and 2.4 gives the familiar screening equation from the London brothers [3]

$$\nabla^2 \mathrm{B} = \frac{1}{\lambda^2}\mathrm{B} \tag{2.16}$$

along with its solution

$$\mathrm{B} = \mathrm{B}_o e^{-z/\lambda} \tag{2.17}$$

The field decays exponentially with the frequency independent length scale of the London penetration depth λ, where

$$\lambda = \sqrt{\frac{m}{\mu_o n e^2}} \tag{2.18}$$

Substituting $\sigma = -ine^2/m\omega$ into the Equation 2.6 shows of course that $R_s = 0$ and all the energy associated with the surface current is stored in the reactance

$$X_s = \sqrt{\frac{\mu_o m \omega^2}{ne^2}} = \mu_o \omega \lambda \tag{2.19}$$

It is important to realize that the Drude Model was used here primarily as pedagogical tool - it was useful in developing the idea of a complex conductivity and for highlighting two important limiting cases at microwave frequencies, the normal metal (real σ) and the superconductor (imaginary σ). In general, the conductivity $\sigma(\omega)$ is more complicated than the Drude form. However, the results in Equations 2.12 to 2.14 will still hold for a metal of purely real conductivity $\sigma_1(\omega)$, and similarly, Equations 2.16 to 2.19 will adequately describe the electrodynamics of a superconductor if it has a purely imaginary conductivity $\sigma_2(\omega)$.

[2] The delta function at zero frequency arises naturally from taking the limit as $\tau \to \infty$ and noting that the area under the σ_1 curve remains constant. It can also be shown as the necessary consequence of satisfying the Kramers-Kronig relation [11, 24].

2.3 The Two Fluid Model for Superconductivity

That a superconductor can carry an electrical current without dissipation is only strictly true at zero frequency. This may seem to contradict the derivation of Equation 2.16, which is known to aptly describe the Meissner state screening of both dc and low frequency ac magnetic fields in a superconductor, and yet was arrived at here through the assumption of an infinite τ, ie. zero resistance. However, superconductor electrodynamics are not fully characterized by a purely imaginary conductivity. Not all the charge carriers are 'superconducting', and those that are not tend to behave much as the charge carriers do in a normal metal. This is summarized in a two fluid model where the total charge density n is separated into two parts, a *superfluid* of density n_s and a *normal fluid* of density n_n, such that $n = n_s + n_n$ at all temperatures. Above the transition temperature $n_n = n$, while below T_c there is a proportional decrease in n_n as n_s builds up and becomes equal to n at zero temperature.

The total conductivity is the superposition of the normal fluid and superfluid conductivities, so assuming (for now) the Drude Model form for the conductivity of each component, σ at finite frequency (dropping the δ-function at $\omega = 0$) is given as

$$\sigma = \frac{e^2 n_n}{m} \frac{\tau}{1+\omega^2\tau^2} - i \left(\frac{e^2 n_n}{m} \frac{\omega\tau^2}{1+\omega^2\tau^2} + \frac{e^2 n_s}{m\omega} \right) \tag{2.20}$$

The important result here is that the superfluid contributes only to σ_2, while in general the normal fluid will contribute to both σ_1 and σ_2. If, again, interest is limited to the microwave range where $\omega\tau \ll 1$, then the real (imaginary) component of the conductivity depends only on n_n (n_s). In general then, without reference to any specific model of σ_1, the low frequency conductivity of a superconductor in the two fluid model is expected to have the form

$$\sigma = \sigma_1(\omega, \tau, n_n(T)) - i\,\sigma_2(\omega, n_s(T)) \tag{2.21}$$

Here, σ_1 depends in some way on frequency, a scattering time (that will also depend on other parameters), and the temperature dependent normal fluid density, while at low frequencies σ_2 retains the form $e^2 n_s(T)/m\omega$ previously mentioned, where $n_s(T)/m$ is a well defined experimental quantity.

The propagation constant can be written as

$$\gamma = \sqrt{\mu_o \omega (i\sigma_1 + \sigma_2)} \tag{2.22}$$

and the surface impedance

$$Z_s = \sqrt{\frac{\mu_o \omega (i\sigma_1 - \sigma_2)}{\sigma_1^2 + \sigma_2^2}} \tag{2.23}$$

Well below the transition temperature, $n_s \gg n_n$ and the imaginary part of the conductivity dominates, $\sigma_2 \gg \sigma_1$. In this limit $\gamma \simeq \sqrt{\mu_o \omega \sigma_2}$, and if $\omega\tau \ll 1$ as well, then the pertinent length scale for the decay of the magnetic field inside the sample is just the London penetration depth λ, as expected. From Equation 2.23 the components of the surface impedance in this regime are easily shown to be

$$\begin{aligned} R_s &= \frac{\mu_o^2 \omega^2 \lambda^3 \sigma_1}{2} \\ X_s &= \sqrt{\frac{\mu_o \omega}{\sigma_2}} = \mu_o \omega \lambda \end{aligned} \tag{2.24}$$

2.4 Microwave Cavity Perturbation: Basic Technique and High-T_c Results

The generic configuration of a resonant cavity measurement on a single crystal superconductor is show in Figure 2.1. Here, the sample is introduced into the cavity on a thin sapphire plate, and the resonant mode within the cavity is chosen such that the sample sits predominantly in a uniform magnetic field. This also helps to avoid exposure of the sapphire plate to electric fields, which in turn limits the signal from the dielectric response of the sapphire. The perturbation of the resonant frequency f_o and quality factor

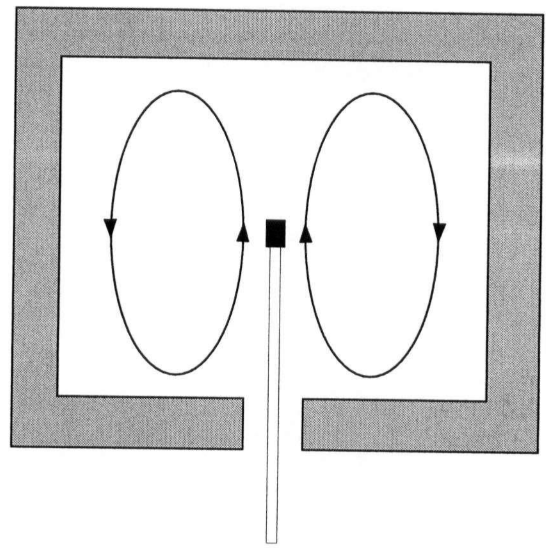

Figure 2.1: The microwave cavity resonator.

Q_o of the unloaded cavity is controlled by the surface impedance of the sample.

Energy loss in the cavity is governed by the value of $1/Q$, so it is very straightforward that any additional losses from the surface resistance of the sample will be proportional to the shift in $1/Q$:

$$\Delta(1/Q) \propto R_s$$

A change in the effective volume of the cavity due to the diamagneic shielding of the sample will result in a shift in resonant frequency proportional to the *effective* volume of the sample V_s:

$$\Delta f = f - f_o \propto V_s$$

For a thin platelet sample, $V_s \simeq V - 2A\lambda(T)$, where V is the geometrical sample volume, A its surface area, and $\lambda(T)$ its temperature dependent penetration depth. The absolute value of $\lambda(T)$ is difficult to measure reliably, because the first term in V_s is so dominant, and it is not possible to measure V and Δf with sufficient accuracy. However, a subsequent frequency shift $\Delta f'$ due to a change in sample temperature allows precision measurements of $\Delta\lambda(T)$:

$$\Delta f' = f(T_2) - f(T_1) \propto \lambda(T_2) - \lambda(T_1) = \Delta\lambda(T)$$

A knowledge of $\Delta\lambda$ and R_s as a function of temperature can be combined with a known value of λ_o (measured by a different technique) and through Equations 2.24 provide a complete picture of the sample's conductivity throughout the superconducting state. Interpreting σ through the two-fluid model allows one to then build up a picture of the superconducting condensate n_s and its excitations n_n.

Some microwave data on YBCO are shown below. In Figure 2.2 measurements of the penetration depth are shown for all three crystallographic directions and shows the strong anisotropy of the high-T_c materials [26].

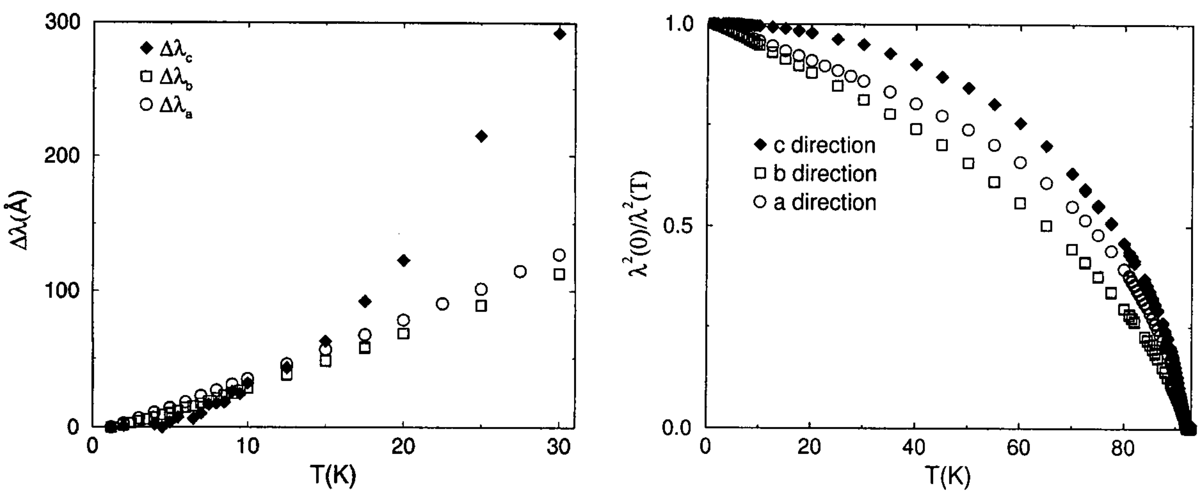

Figure 2.2: The anisotropy of the penetration depth in $YBa_2Cu_3O_{6.95}$ (from Hossieni *et al.* [26]). Left graph: $\Delta\lambda(T)$. Right graph: the superfluid density fraction $\lambda^2(0)/\lambda^2(T)$.

In Figure 2.3, the real part of the conductivity σ_1 is shown as a function of temperature (left panel) and as a function of frequency (right panel). The peak seen at about 25 K (for the low frequency data) is a result of competition between the decreasing normal fluid density n_n and an increase in quasi-particle lifetime τ. The data fits quite well to the Drude model below 20 K, and the narrow width of about 9 GHz indicates a very long τ, which is a result of the very high quality of the samples.

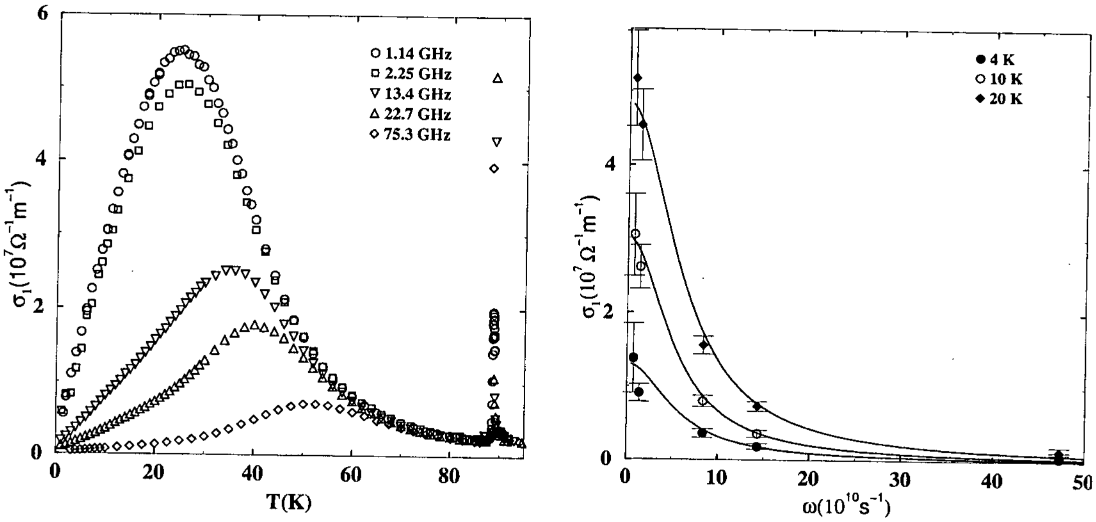

Figure 2.3: The microwave conductivity σ_1 of $YBa_2Cu_3O_{6.993}$ (from Hossieni *et al.* [27]). Left graph: as a function of temperature. Right graph: as a function of frequency.

Chapter 3

The Nonlinear Meissner Effect

In high-T_c superconductors, experiments studying the energy gap and its symmetry, and therefore the symmetry of the pairing state, have always been of central importance. However, for some time after the discovery of these materials, experiments produced conflicting results and left much debate as to whether or not the pairing state had the conventional s-wave symmetry of BCS theory. Yip and Sauls [28] proposed experiments based on the nonlinear effects of an applied magnetic field on the Meissner state supercurrent that would differentiate between s-wave and d-wave superconductors (the d-wave state with $d_{x^2-y^2}$ symmetry having long been the favoured alternative to s-wave for the cuprates.) This debate has now been largely settled by a number of other experiments [19, 20, 29], which have left little doubt that for HTSC's the pairing state exhibits a predominantly $d_{x^2-y^2}$ symmetry [21]. However, the nonlinear Meissner effect (NLME) remains experimentally undertested, although there has been a considerable amount of theoretical work (see Section 3.4).

The NLME leads to a field dependent penetration depth and magnetization, and for a $d_{x^2-y^2}$ gap these effects depend on the orientation of the field relative to the nodes. As we shall see later in this chapter, theory predicts that at sufficiently low temperatures there is a linear field dependence of λ of the form

$$\Delta\lambda(H) = \alpha\lambda\,|H|\,/H_o$$

where α is equal to unity for fields along a node in the energy gap and $1/\sqrt{2}$ when fields are along an antinode; the quantity $\mathrm{H_o}$ is a characteristic field of order the thermodynamic critical field [30]. In contrast, a superconductor with a conventional gap would show an H^2 dependence of $\Delta\lambda$, with a thermally activated prefactor and with no anisotropy with respect to field direction. This is the real heart of the Yip and Sauls theory: nonlinearities in the Meissner state screening currents behave quite differently for a superconductor with an isotropic s-wave gap versus one with a $d_{x^2-y^2}$ gap. Furthermore, the theory offers the prospect of using electrodynamic measurements as a probe to determine the positions of the nodes in the gap. This is the main reason researchers have remained interested in this theory.

In this Chapter, the fundamental ideas of the Yip and Sauls theory of the Nonlinear Meissner Effect will be presented. We begin with the linear London equations, and from there describe in general how nonlinearities (in the supercurrent) lead to a field dependent penetration depth. The NLME theory considers the energy shift in the quasiparticle excitation spectrum in the presence of superfluid flow as the source of this nonlinearity. There is now in the literature a large and varied body of other theoretical work that all start with this main premise (from Yip and Sauls) and expand on the various aspects of the original theory. The pertinent details of these theories will also be described here, and an overview of the experimental situation will also be given.

3.1 The Linear London Equation

Ignoring the damping term in Equation 2.7, the free acceleration of an electron in an applied electric field leads directly to the first London equation:

$$\frac{\partial \boldsymbol{J}}{\partial t} = \frac{ne^2}{m}\boldsymbol{E} \tag{3.1}$$

where the relation between the charge current and velocity is linear, $\boldsymbol{J} = -en\boldsymbol{v}$. Taking the curl of both sides of Equation 3.1 and substituting Faraday's Law $\nabla \times \boldsymbol{E} = -\dot{\boldsymbol{B}}$ gives the relation between the current density and the magnetic field in a superconductor:

$$\frac{\partial}{\partial t}\left(\nabla \times \boldsymbol{J} + \frac{ne^2}{m}\boldsymbol{B}\right) = 0 \tag{3.2}$$

As the Londons noticed, the existence of the Meissner effect requires that this equation hold for time dependent fields as well as the trivial static case, and this requires that the term in brackets be identically zero. This gives the second London equation:

$$\nabla \times \boldsymbol{J} = -\frac{ne^2}{m}\boldsymbol{B} \tag{3.3}$$

This equation combined with Ampere's Law $\nabla \times \boldsymbol{B} = \mu_o \boldsymbol{J}$ returns Equation 2.16, namely $\nabla^2 \boldsymbol{B} = \boldsymbol{B}/\lambda^2$, that governs the shielding of magnetic fields within a superconductor.

A relation between the current density $\boldsymbol{J}$ and vector potential $\boldsymbol{A}$ is obtained by substituting $\boldsymbol{B} = \nabla \times \boldsymbol{A}$ into the second London equation, which gives

$$\boldsymbol{J} = -\frac{ne^2}{m}\boldsymbol{A} \tag{3.4}$$

or

$$\boldsymbol{v} = \frac{e}{m}\boldsymbol{A} \tag{3.5}$$

Interestingly enough, Equation 3.4 summarizes the London equations in a single compact form: taking its time derivative gives Equation 3.1, while its curl returns Equation 3.3. To have $B = 0$ inside the superconductor, one must choose the London gauge $\nabla \cdot \boldsymbol{A} = 0$. Now, the vector potential also has the form of Equation 2.16, as does v:

$$\nabla^2 \boldsymbol{v} = \frac{1}{\lambda^2}\boldsymbol{v} \tag{3.6}$$

The superfluid velocity decays exponentially from the surface of the superconductor on the length scale of the penetration depth.

Even more interesting, however, is that this simple treatment of the Meissner state phenomenon alludes to the underlying quantum nature of superconductivity [11, p. 5].

Given that the canonical momentum $\boldsymbol{p} = m\boldsymbol{v} - e\boldsymbol{A}$, Equation 3.5 implies that the net momentum of the superfluid is always zero. This prompted Fritz London to note, prior to BCS theory, that the long range order in the average momentum cannot be the result of some mechanism which could be constructed by classical mechanics [31, p. 146]. Of course, London's assertion was correct, superconductivity is a macroscopic quantum state. The zero net momentum subsequently implies that the fundamental relation linking the charge flow in a superconductor to an applied field is between $\boldsymbol{v}$ and $\boldsymbol{A}$ via Equation 3.5. Only in the low field limit, is the linear relation between $\boldsymbol{J}$ and $\boldsymbol{A}$ of Equation 3.4 valid.

3.2 The Nonlinear London Equation

In general, the supercurrent $\boldsymbol{J}_s$ need not be a linear in superfluid velocity $\boldsymbol{v}_s$ and may include higher order terms such that

$$\boldsymbol{J}_s = -en_s\boldsymbol{v}_s(1 - \alpha\,|\boldsymbol{v}_s| - \beta\boldsymbol{v}_s^2 - ...) \tag{3.7}$$

Here, the notation of the two-fluid model (Section 2.3) has again been adopted with the quantity n_s referring to the zero-field, temperature dependent superfluid density. The supercurrent is related to the vector potential through Ampere's Law, $\nabla \times (\nabla \times \boldsymbol{A}) = \mu_o\boldsymbol{J}_s$, which becomes

$$\nabla^2\boldsymbol{A} = -\mu_o\boldsymbol{J}_s$$

under the London gauge. Substituting for $\boldsymbol{A}$ (from Equation 3.5) on the left hand side and for $\boldsymbol{J}_s$ (from Equation 3.7) on the right gives the following nonlinear (London) equation for the superfluid velocity:

$$\nabla^2\boldsymbol{v}_s = \frac{\mu_o n_s e^2}{m}\boldsymbol{v}_s(1 - \alpha\,|\boldsymbol{v}_s| - \beta\boldsymbol{v}_s^2 - ...) \tag{3.8}$$

Re-writing this as

$$\nabla^2 \boldsymbol{v}_s = \frac{\mu_o \tilde{n}_s e^2}{m} \boldsymbol{v}_s \tag{3.9}$$

with $\tilde{n}_s = n_s(1 - \alpha |\boldsymbol{v}_s| - \beta \boldsymbol{v}_s^2 - ...)$ and comparing to Equation 3.6, it is clear that the penetration depth now depends on the superfluid velocity:

$$\frac{1}{\lambda^2} = \frac{\mu_o \tilde{n}_s e^2}{m} \tag{3.10}$$

In words, the effect of a finite $\boldsymbol{v}_s$ is to reduce the overall superfluid density with a consequent increase in the penetration depth. Or equivalently, an applied field breaks pairs, which reduces the ability of the superconductor to screen the field and results in a larger penetration depth. To determine the field dependence of λ, one first seeks the appropriate form of Equation 3.7 for $\boldsymbol{J}_s$ and then solves Equation 3.8. This is the approach taken by Yip and Sauls [28] (and later by Xu, Yip, and Sauls [30]) in their seminal work on the Nonlinear Meissner Effect.

3.3 The Yip and Sauls Theory

The theory of the Nonlinear Meissner Effect considers first that a shift in quasparticle energy occurs in finite field due to the induced superfluid velocity $\boldsymbol{v}_s$. This energy shift is given as $\boldsymbol{p}_f \cdot \boldsymbol{v}_s$, where $\boldsymbol{p}_f$ is the Fermi momentum.[1] The total supercurrent is then determined by the sum in momentum over all the shifted quasiparticle states. As first shown in Ref. [28], this can be written as

$$\boldsymbol{J}_s = -eN_f \int d^2 s\, n(s)\, \boldsymbol{v}_f \left\{ \boldsymbol{p}_f \cdot \boldsymbol{v}_s + 2\int_0^\infty d\xi \left[f(E + \boldsymbol{p}_f \cdot \boldsymbol{v}_s) \right] \right\} \tag{3.11}$$

where N_f is the total density of states at the Fermi level, $n(s)$ is the angle-resolved density of states at a point s on the Fermi surface normalized to unity, $\boldsymbol{v}_f$ is the s-dependent Fermi

[1] This idea first came from John Bardeen [32], who considered that the excitations in a superconductor are relative to the momentum of the condensate, analogous to the situation in superfluid helium.

velocity, f is the Fermi function, and $E = \sqrt{\xi^2 + |\Delta(s)|^2}$ is the BCS excitation energy for a superconductor with gap $\Delta(s)$. Equation 3.11 is the specific form of Equation 3.7 as determined by the Yip and Sauls theory. The first term is the unperturbed supercurrent of the total condensate, namely $\boldsymbol{J}_s = -en\boldsymbol{v}_s$; the second term, represents changes in $\boldsymbol{J}_s$ due to excitations. In the linear limit ($\boldsymbol{v}_s \to 0$), it accounts for the temperature dependence of the superfluid density, whereby n is reduced to $n_s(T)$ at $T \neq 0$, and when $\boldsymbol{v}_s$ is finite, it also gives the nonlinearities that arise in the supercurrent.

In the linear limit, the temperature dependence of n_s depends on the symmetry of the gap. This is reflected in measurements of $\Delta\lambda(T)$ shown in Figure 1.4; the full gap of an s-wave superconductor will produce a much different $\Delta\lambda(T)$ than a d-wave superconductor, where the gap goes to zero along four nodal lines. The symmetry of the gap also determines the nature of the nonlinear terms in $\boldsymbol{J}_s$ and therefore the field dependence of λ as well. However, in this case an anisotropy in the gap will also produce a similar anisotropy in $\Delta\lambda(H)$, and as a result the field dependent measurements should provide more direct information on the pairing state itself.

Yip and Sauls worked this out for two pertinent cases: the isotropic s-wave gap of conventional superconductivity and the $d_{x^2-y^2}$ gap, which was the leading candidate for proposed unconventional superconductivity in the high-T_c materials. A diagram of these two gap functions is shown in Figure 3.1 along with schematic description of the Nonlinear Meissner Effect, which complements the following discussion.

For the conventional gap, Equation 3.11 becomes

$$\boldsymbol{J}_s = -en_s(T)\boldsymbol{v}_s \left[1 - \beta(T)\left(\frac{v_s}{v_c}\right)^2\right] \tag{3.12}$$

For a flat superconducting slab with a field H applied parallel to the its surface, the magnitude of the supercurrent at the surface is proportional to the field in the linear limit, $\mathrm{J}_s = H/\lambda \propto \mathrm{v}_s$. For the nonlinear case, the leading order correction in λ will be quadratic in H. The exact form[2] is

$$\lambda(T,H) = \lambda(T)\left\{1 + 3\beta(T)\left[\frac{H}{H_o}\right]^2\right\} \tag{3.13}$$

where $H_o = 2cv_c/e\lambda(T)$ is of order the thermodynamic critical field H_c, and the critical velocity $v_c = \Delta(T)/p_f$. At low temperatures, the coefficient $\beta(T) \sim exp(-\Delta/T)$, so the consequence of the finite gap is that the Nonlinear Meissner Effect in conventional superconductors becomes very weak once one is well below T_c and disappears as $T \to 0$.

For the unconventional superconductor, Yip and Sauls treat the problem as being essentially 2D. As a result, the $d_{x^2-y^2}$ gap in the xy-plane can be written as $\Delta = \Delta_o\,|\cos 2\theta|$, where Δ_o is the gap maximum and θ is the angle measured from the x-axis. At $T = 0$, Equation 3.11 becomes

$$\boldsymbol{J}_s = -en_s(T)\boldsymbol{v}_s\left[1 - \alpha\frac{|v_s|}{v_o}\right] \tag{3.14}$$

and one expects, therefore, a penetration depth that is linear in field. The exact form is

$$\lambda(T,H) = \lambda(T)\left\{1 + \alpha\frac{|H|}{H_o}\right\} \tag{3.15}$$

Here, $H_o = 3cv_o/2e\lambda(T) \sim H_c$ and $v_o = \mu\Delta_o/p_f^*$ where $\mu \equiv 1/\Delta_o \mathrm{d}(\Delta/d\theta)$ is the angular slope of the nodes in the gap, Δ_o is the gap maximum, and p_f^* is the Fermi momentum at the nodes. The coefficient α is independent of temperature and in particular does not disappear at zero temperature, which is a consequence of there being nodes in the gap.

The reason for the different NLME in s-wave and d-wave superconductors is abundantly clear from Panels III and IV in Figure 3.1. In finite field, the energy levels are shifted by the amount $\boldsymbol{p}_f \cdot \boldsymbol{v}_s$, which means that states on opposite sides of the Fermi surface will be shifted in opposite directions. Excitation states that have a momentum component counter-moving (co-moving) to the superfluid velocity $\boldsymbol{v}_s$ are shifted to lower

[2]The precise details for solving the nonlinear London equation for the both the s-wave and the d-wave case can be found in Appendix A.

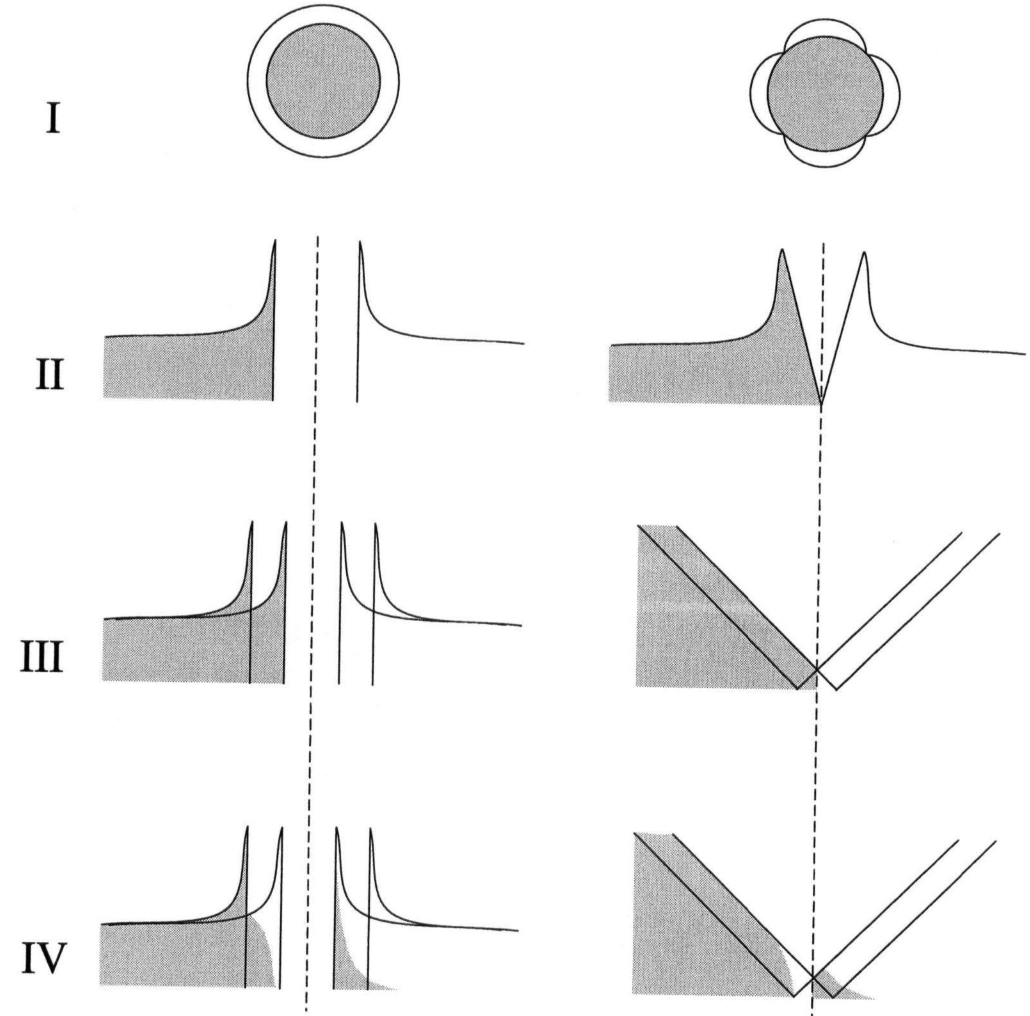

Figure 3.1: Diagram showing the origin of the NLME in s-wave (left side) and d-wave (right side) superconductors. **I.** The conventional isotropic gap and the unconventional $d_{x^2-y^2}$ gap. **II.** The density of states at $T, H = 0$. All excited states above the Fermi energy (dashed line) are unoccupied. **III.** The density of states at $T = 0, H \neq 0$ at opposing points (nodes) on the s-wave (d-wave) Fermi surface (for clarity in the d-wave picture, the view has been expanded around the nodes). Co-moving states are shifted up in energy by $+\boldsymbol{p}_f \cdot \boldsymbol{v}_s$, counter-moving states are shifted down by $-\boldsymbol{p}_f \cdot \boldsymbol{v}_s$. Quasiparticle backflow current (NLME) is present for d-wave, but not s-wave. **IV.** The density of states at $T, H \neq 0$. Thermal excitations lead to a finite NLME in the s-wave case, and weaken the effect at low fields in the d-wave case.

(higher) energies. The counter-moving states are now energetically favoured for population over the co-moving states, and as a result thermal or field-induced excitations give rise to a quasiparticle current that opposes the supercurrent. This backflow current, as it is often called [30], is the microscopic origin of the NLME, the source of nonlinearity in $\boldsymbol{J}_s$. In an s-wave superconductor, the quasiparticle states are still separated from the condensate by a finite energy gap, so a field dependent λ can only occur in finite temperature. In the d-wave case, where the gap is zero at the node, part of the co-moving branch of the condensate is always shifted to higher energy than some of the counter-moving excitation states. This results in a NLME that persists to zero temperature. At finite temperature, the linear $\lambda(H)$ of a d-wave superconductor actually turns over to a weak quadratic field dependence at low fields, but this is distinguishable from s-wave in that the effect goes as $1/T$.

Another interesting feature of the d-wave NLME is its anisotropy with respect to the direction of $\boldsymbol{v}_s$. Consider the two special situations shown in Figure 3.2, where the superfluid velocity is directed either along a node (left panel) or antinode (right panel) in momentum space. When $\boldsymbol{v}_s$ is along a node, the only states that contribute to the backflow current occupy a small wedge within the angle $\vartheta_c = p_f v_s/\mu\Delta_o$ centred about the node on the opposite side of the Fermi surface. When $\boldsymbol{v}_s$ is along an antinode, there will be two nodes that contribute to the backflow current. However, in this case the energy shift is a factor of $\sqrt{2}$ less than above for a given $|\boldsymbol{v}_s|$, and the wedge of contributing states is defined by the smaller angle $\vartheta_c/\sqrt{2}$ about each node. Furthermore, the backflow current at each node is no longer antiparallel to $\boldsymbol{v}_s$, and the component along this direction is only $1/\sqrt{2}$ of the total current. The overall effect is that the coefficient α from Equation 3.15 differs by a factor $1/\sqrt{2}$ between the two cases:

$$\lambda(T,H) = \lambda(T)\left\{1+\frac{|H|}{H_o}\right\}, \qquad H\,||\,\text{node} \tag{3.16}$$

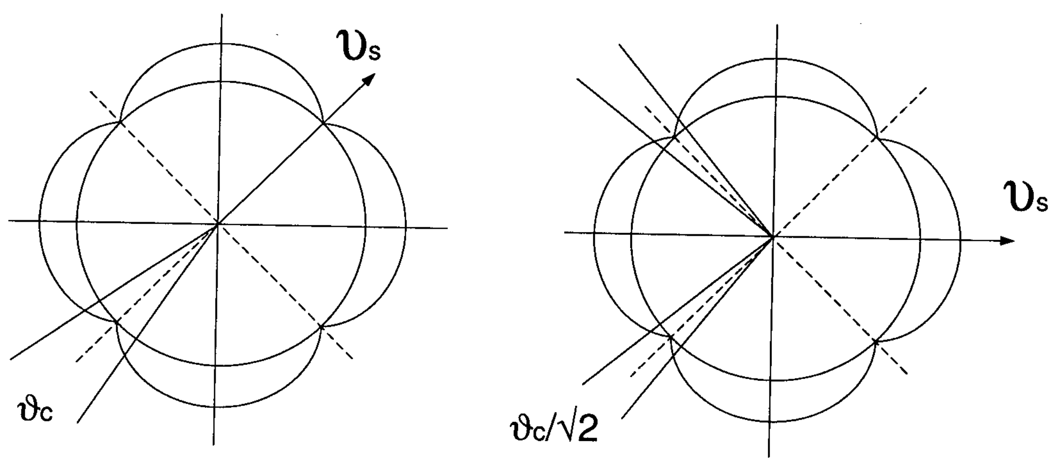

Figure 3.2: The quasiparticle backflow currents at $T = 0$ for $\boldsymbol{v}_s$ parallel the node (left) and antinode (right) of a $d_{x^2-y^2}$gap (after Xu *et al.* [30]). The wedge of states contributing to the backflow current is less when $\boldsymbol{v}_s$ is along an antinode.

$$\lambda(T,H) \;=\; \lambda(T)\left\{1+\frac{1}{\sqrt{2}}\frac{|H|}{H_o}\right\}, \quad H\,||\,\text{antinode} \tag{3.17}$$

It is this anisotropy that allows the possibility of determining the position of the nodes by measuring $\Delta\lambda(H)$ for different field orientations. In general, the coefficient $\alpha = (1/2\sqrt{2})\sum_{l=\pm1}|\cos\theta + l\sin\theta|^3$ where θ is the angle between $\boldsymbol{v}_s$ and an antinode [33].

If v_s is not directed along a node or an antinode (ie. $\theta \neq n\pi/4$), there will be a finite component of the total quasiparticle backflow current that is perpendicular to the superfluid velocity. This results in another interesting manifestation of the NLME in d-wave superconductors, the formation of a transverse magnetic moment in the superconducting sample. As mentioned above, when $\boldsymbol{v}_s$ is along a node ($\theta = \pi/4$) the backflow current is directly opposite to it. When $\boldsymbol{v}_s$ is along an antinode ($\theta = 0$) there will be two identical backflow 'jets' contributing to this current, but their perpendicular components exactly cancel each other and the net result is still a strictly antiparallel backflow current. However, at all other orientations a perpendicular component will survive, and this gives rise to a transverse magnetic moment $\boldsymbol{M}_\perp$ (and thus a magnetic torque $\boldsymbol{\tau} = \boldsymbol{M}_\perp \times \mu_o\boldsymbol{H}$)

that is also dependent on θ, the relative orientation of $\boldsymbol{v}_s$ with respect to the antinodes. At $T = 0$ the magnitude of $\boldsymbol{M}_\perp$ is quadratic in H, so $\boldsymbol{\tau} \propto \mathrm{H}^3$, and both $\boldsymbol{\tau}$ and $\boldsymbol{M}_\perp$ vary as $|\sin\theta\cos\theta\,(\cos\theta - \sin\theta)|$ over the range $0 < \theta < \pi/2$ [30, 34].

For a $d_{x^2-y^2}$ superconductor, the crystal axes in the ab-plane coincide with the antinodal directions in momentum space shown in Figure 3.2. For a field applied in the ab-plane of a thin slab shaped superconductor, the superfluid velocity $\boldsymbol{v}_s$ of the in-plane screening current will be perpendicular to H. As a result, and to recap the basics of the Yip and Sauls theory, measurements of λ, $\boldsymbol{M}_\perp$, or $\boldsymbol{\tau}$ in high-T_c single crystals as a function of field strength and its relative orientation to the crystal axes in the *ab*-plane should reveal the underlying anisotropy of the superconducting gap in these materials. For example, in $YBa_2Cu_3O_{7-\delta}$, ignoring its orthorhombicity and assuming $\lambda_{ab} \sim 1500$Å and $H_o \sim 2.5 \times 10^4$ gauss, a field of 250 gauss ($\sim H_{c1}$) will produce a $\Delta\lambda \sim 11$Å if it is applied along the crystal axes, and ~ 15Å if the field is at 45° to this direction [30].

3.4 Extensions of the Yip and Sauls Theory

The promise that a bulk measurement, of the magnetic moment for example, could be used to trace out the symmetry of the underlying order parameter of a high-T_c superconductor has kept many researchers interested in the Yip and Sauls theory of the Nonlinear Meissner Effect. Unfortunately, this sort of *node spectroscopy*, as it was dubbed by Žutić and Valls [35], has been extremely difficult to realize in the lab, and only a brief summary (Section 3.5) will be needed to cover all of the published experimental work to date. In relative contrast to this situation, the theoretical front has flourished. Spurred on in part to explain the apparent failure of experiments to observe the basic NLME, there have been several efforts to build upon the original theory and incorporate other effects (such as those of impurities, nonlocality, orthorhombicity, etc.) that may be present in the unconventional high-T_c superconductors. The details of much of this work will be described below with a specific emphasis on the field dependence of λ, which is most pertinent to this thesis.

3.4.1 Finite Temperature and Impurity Scattering

The effects of finite temperature and impurity scattering are briefly discussed in the original paper [28], but were first thoroughly explored by Stojković and Valls [34] and subsequently by Xu, Yip, and Sauls [30]. As mentioned in the previous section, the field dependence of the $d_{x^2-y^2}$ penetration depth shows a cross-over from linear to quadratic behaviour when $T \neq 0$. This effect can be visualized, in a very simple way, by considering what is happening in Panel IV (right side) of Figure 3.1 if the field is being increased from zero at some fixed finite temperature. At small H (or v_s) the thermal excitations would be nearly equally shared by both the co-moving and counter-moving quasiparticle branches. As the field increases and the branches separate, the thermal excitations begin to reside more and more in the counter-moving branch; the result being an H^2 dependence in λ (similar to the s-wave case). This continues with increasing field until the counter-moving quasiparticle branch starts to overlap with the still occupied states in the co-moving condensate branch, recovering the effect depicted in Panel III. This cross-over will take place when the thermal energy $k_B T$ is of order the energy shift $\boldsymbol{p}_f \cdot \boldsymbol{v}_s$, so for a given T there will be some field H_T above which the linear $\lambda(H)$ is recovered. Below the cross-over field H_T, where $\boldsymbol{p}_f \cdot \boldsymbol{v}_s \ll k_B T$, the supercurrent from Equation 3.11 can be expanded in a power series in $p_f v_s$ that has a leading order correction term $(p_f v_s)/T\Delta_o$. As a result, in this limit $\lambda(H)$ is weakly quadratic and decreases with temperature as $1/T$. Similarly, the field effects on τ and $M_\perp$ are reduced with temperature [28, 30, 34]. Numerical results for $\Delta\lambda(H)$ and $\tau(\theta)$ at various temperatures are shown in Figure 3.3. A result of this cross-over is that the signature linear $\lambda(H)$ of a d-wave superconductor

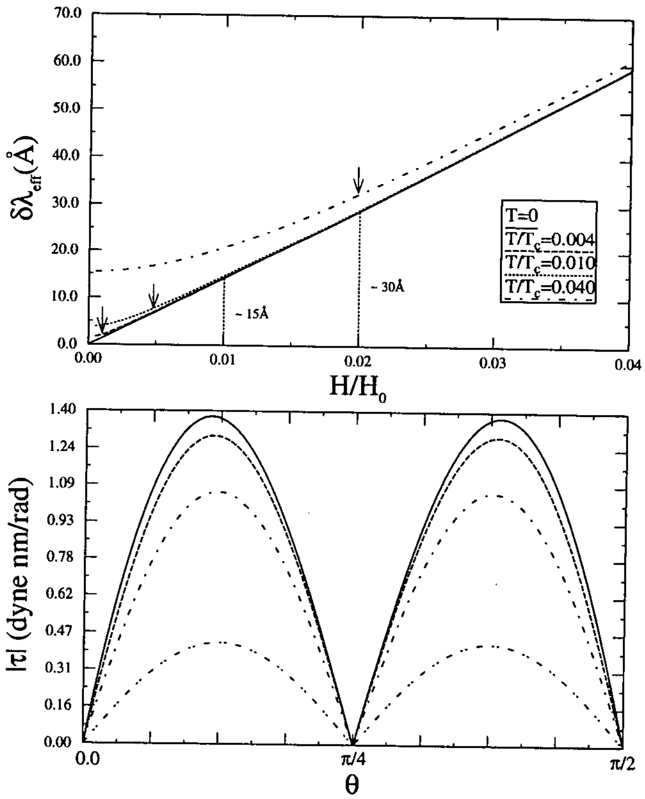

Figure 3.3: Thermal effects on $\lambda(H)$ and $\tau(\theta)$ for a d-wave supercondcutor (from Xu *et al.* [30]). Top graph: The change in penetration depth versus the normalized field H/H_o for several normalized temperatures T/T_c; the arrows indicate the cross-over field. Bottom Graph: The torque versus θ at a fixed field of 400G for the same temperatures. $|\tau|$ decreases with increasing T/T_c.

may not be observable if the temperature is not low enough. The reason being that the applied fields are limited to values below H_{c1} (to remain in the Meissner state), and may not be arbitrarily increased to recover the linear behaviour.

The effects of impurities are considered in a similar manner to that of finite temperature: there is an energy scale ε^* associated with the impurity scattering that sets a cross-over field when of order $\boldsymbol{p}_f \cdot \boldsymbol{v}_s$. The result is again that $\lambda(H)$ crosses-over to weaker,

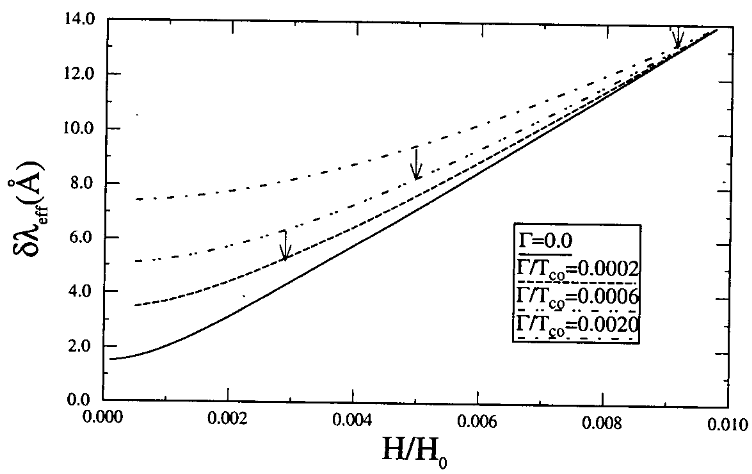

Figure 3.4: Impurity effects on $\lambda(H)$ for a d-wave superconductor at temperature $T/T_c = 0.04$ (from Xu *et al.* [30]). $\Delta\lambda$ versus H/H_o shows a cross-over (denoted by the arrows) that increases with impurity concentration, Γ/T_{co}.

quadratic dependence at low fields; the cross-over field increases with impurity concentration Γ/T_{co} as shown in Figure 3.4. However, for impurity levels typical in the high quality $YBa_2Cu_3O_{7-\delta}$ single crystals grown by Ruixing Liang at UBC, $\Gamma/T_{co} \sim 0.0002$ and this effect should be quite small [30]. Results showing a similar reduction in $M_\perp$ with impurity concentration were obtained in Ref. [34].

Work by Dahm and Scalapino [36, 37] has concentrated almost exclusively on the high temperature limit of the NLME for the $d_{x^2-y^2}$ gap. Here $\boldsymbol{p}_f \cdot \boldsymbol{v}_s \ll k_B T$ and the field dependence of the penetration depth can be expressed as

$$\Delta\lambda(T,H) = \lambda(T)\frac{\beta}{2}\left(\frac{H}{H_o}\right)^2 \tag{3.18}$$

The temperature and impurity dependence of the coefficient β are shown in Figure 3.5. At low temperatures β goes as $1/T$ as previously mentioned. This divergence in $\beta(T)$ is usually cut off by the cross-over to the linear $\lambda(H)$, but impurity scattering will have a similar effect and it was also shown that this can cause the quadratic field dependence to

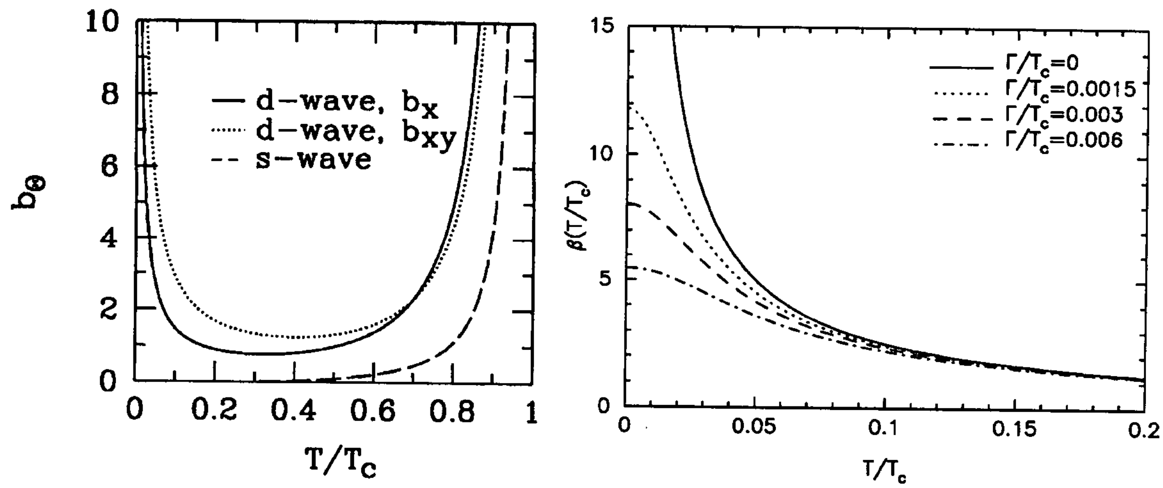

Figure 3.5: Temperature dependence of the nonlinear coefficient β (from Dahm and Scalapino [36, 37]). Left graph: β ($\equiv b_\theta$) versus normalized temperature for fields along the antinodes (b_x) and nodes (b_{xy}) contrasted by the isotropic s-wave case. Right graph: β versus normalized temperature for different impurity concentrations.

persist to zero temperature. It was suggested by Dahm and Scalapino that the resulting peak in $\beta(T)$ at $T = 0$ is as much a signature of a $d_{x^2-y^2}$ gap as is the linear $\lambda(H)$, and whereas the latter can be masked by impurity scattering and nonlocal effects the former is a much more robust indicator of the d-wave NLME [37]. However, if again one assumes $\lambda_{ab} \sim 1500$Å and $H_o \sim 2.5 \times 10^4$ gauss for $YBa_2Cu_3O_{7-\delta}$ and takes a modest value of $\beta = 6$, then an applied field of 250 gauss only gives $\Delta\lambda \sim 0.5$Å. This pushes the required experimental resolution up by another order of magnitude, and is probably inaccessible even with the state-of-the-art measurement technique to be presented in this thesis!

3.4.2 Nonlocality

High-T_c superconductors, being extreme Type II with $\lambda \gg \xi$, have generally been assumed to follow local electrodynamics. The coherence length is much smaller than the penetration depth, which characterizes spatial variations of the fields within the sample, so as a result the Cooper pairs behave essentially as point particles reacting to the local value of the field only. The coherence length is given by BCS theory as $\xi_o = \hbar v_f/\pi\Delta_o$, and it was essentially taken for granted that this definition was valid for the cuprates as well, using the gap maximum for Δ_o. In 1997, Kosztin and Leggett [38] made the seemingly simple observation that a coherence length should actually take on the anisotropy of the gap by generalizing the above definition to $\xi_o(\boldsymbol{k}) = \hbar v_f/\pi\Delta(\boldsymbol{k})$. This would imply that near the gap nodes $\xi_o \gg \lambda_o$, and the Cooper pairs in this region would be objects extending well beyond spatial variations in the field and could be expected to behave nonlocally. From this idea Kosztin and Leggett were able to show that the linear temperature dependence of the penetration depth in a d-wave superconductor would become quadratic in T at low T. In fact, quadratic behaviour is often seen in $\Delta\lambda(T)$ measurements (Ref. [23] for example), and previously has been attributed solely to the effect of impurity scattering [39].

Incorporating this idea along with the energy shift $\boldsymbol{p}_f \cdot \boldsymbol{v}_s$ in the quasiparticle states, Li *et al.* [33, 40] were able to arrive at a form for the penetration depth in a $d_{x^2-y^2}$ superconductor that included both nonlocal and nonlinear effects. Following the method laid out in Ref. [11, Appendix 3] for finding the exact solution of λ via Fourier analysis, they write the general penetration depth as

$$\begin{aligned} \lambda &= \frac{2}{\pi}\int_0^\infty \frac{\mathrm{d}q}{4\pi\mathcal{K}(\boldsymbol{q},\boldsymbol{v}_s,T)+q^2} \\ &\simeq \lambda_o - \frac{8}{c}\int_0^\infty \mathrm{d}q \frac{\delta\mathcal{K}(\boldsymbol{q},\boldsymbol{v}_s,T)}{(\lambda_o^{-2}+q^2)^2} \end{aligned} \tag{3.19}$$

where $\mathcal{K}(\boldsymbol{q},\boldsymbol{v}_s,T)$ is the coefficient relating the qth Fourier component of the current inside the superconductor to that of the vector potential. The exact form of $\mathcal{K}(\boldsymbol{q},\boldsymbol{v}_s,T)$ is not given here, but by writing $\mathcal{K}(\boldsymbol{q},\boldsymbol{v}_s,T) = c/(4\pi\lambda_o^2) + \delta\mathcal{K}(\boldsymbol{q},\boldsymbol{v}_s,T)$ Li *et al.* were able to treat the nonlinear, nonlocal effects as a small perturbation and separate them from the $T = 0$ linear, local response in Equation 3.19. This expression reduces exactly to the nonlocal result of Kosztin and Leggett [38] if the $\boldsymbol{v}_s$ dependence is ignored and gives the linear $\lambda(H)$ of Yip and Sauls [28] if the q dependence is ignored [33]. The effect of nonlocality on $\lambda(H)$ is shown in Figure 3.6. Here H is considered to be along the c-axis (the effect is strongest in this regime) and the supercurrent flows at some angle θ to the a-axis. At low fields, the nonlocal effects dominate, which washes out the linear field dependence and reduces the expected $1/\sqrt{2}$ anisotropy in $\Delta\lambda(H)$. Li *et al.* [33] proposed, in fact, that nonlocality might actually make the NLME unobservable, arguing that the cross-over field between the nonlocal and nonlinear regimes would be roughly equal to the lower critical field H_{c1}, and as a result, one would always run into the vortex state before detecting the signature linear $\Delta\lambda(H)$ of the NLME. When the field is applied in the ab-plane, Li *et al.* [40] still estimate this cross-over to be $\sim H_{c1}$. However, their estimate for the latter quantity is much smaller than what has been experimentally determined for that geometry [41], and as a result one must be cautious about accepting their claim.

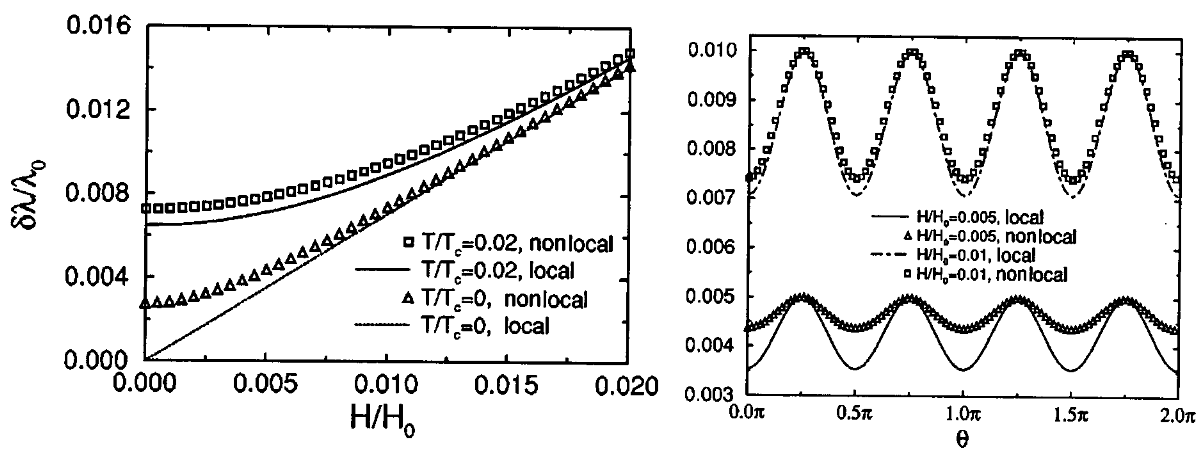

Figure 3.6: Nonlocal effects on $\lambda(H)$ for a d-wave superconductor, with H applied along the c-axis (from Li *et al.* [40]). Left graph: Normalized change in penetration depth versus normalized field (labeled top to bottom). Right graph: The angular dependence of the normalized change in penetration depth for T=0.

3.4.3 Orthorhombicity and Anisotropy

The CuO_2 planes in most cuprate superconductors are actually orthorhombic rather than tetragonal, and in the $YBa_2Cu_3O_{7-\delta}$ system there is a further anisotropy because of the conducting CuO chains in the b-direction [42]. The presence of this orthorhombic distortion means that the symmetry of the system cannot in fact be purely s-wave or purely d-wave. For the high-T_c superconductors where a predominant $d_{x^2-y^2}$ character has been well established, one would then expect orthorhombicity to lead to a state such as $d+s$ or $d+is$. The s-component, if present, is considered to be quite small, and in the former case leads to shift of the gap nodes away from $\pi/4$, while the latter case it will produce a small finite gap resulting in deep 'quasinodes' at $\pi/4$. Extensive work has been done by Žutić and Valls [35, 43, 44] to calculate the effects of mixed symmetry on the transverse magnet moment. Halterman and Valls [45] expanded this work to the pure p-wave state to motivate measurements of $M_\perp$ in Sr_2RuO_4. More recently however, they returned to the high-T_c system and worked out the effects of orthorhombicity and anisotropy on the field dependence of the penetration depth [46, 47] at $T=0$.

Their results for YBCO like orthorhombicity (assuming $d+s$ symmetry) are shown in Figure 3.7, where the normalized $\Delta\lambda(H)$ (which is essentially just the coefficient α from Equation 3.15) is plotted against the angle ψ that the applied field makes with the a-axis. Two parameters are needed to characterize the effect here: $\Lambda \equiv \lambda_a/\lambda_b$, the anisotropy of the in plane penetration depth, and the angle ϕ that the Fermi velocity (at a node) forms with the crystal axis. In the tetragonal limit of the standard Yip and Sauls theory, $\Lambda = 1$ and $\phi = \pi/4$, and the coefficient α varies between a value of $1/\sqrt{2}$ for fields along an antinode and unity for fields along a node. The effects of orthorhombicity and anisotropy will alter this in general, as can be seen in Figure 3.7.

This result is of great consesquence to the interpretation of measurements of $\Delta\lambda(T,H)$

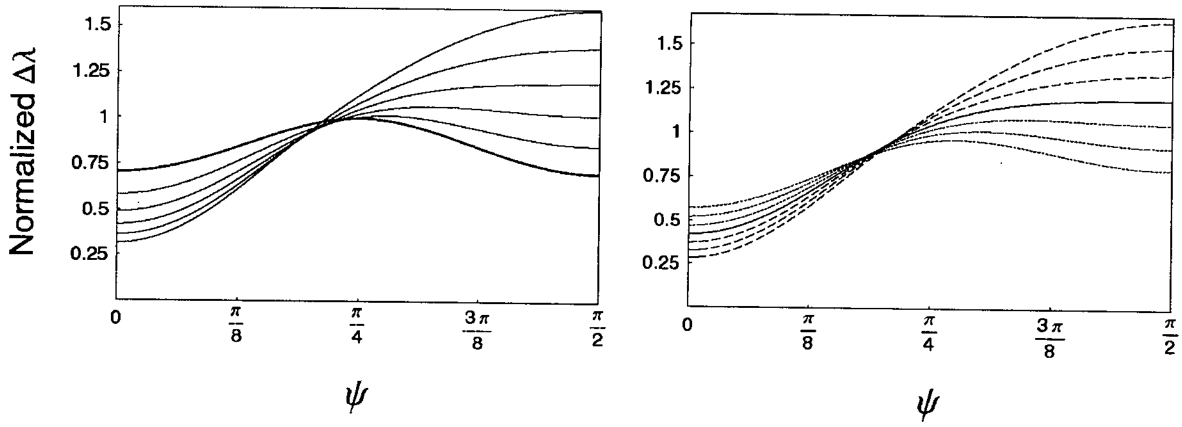

Figure 3.7: The effect of YBCO-type orthorhombicity on the angular dependence of $\Delta\lambda(H)$ (from Halterman and Valls [46]). Left graph: Normalized $\Delta\lambda$ versus the angle ψ for $\Lambda = 1.0\,(\text{tetragonal}), 1.1, 1.2, 1.3, 1.4, 1.5$ with $\phi = \pi/4$. The tetragonal limit (bold curve) gives the $1/\sqrt{2}$ variation from Yip and Sauls. Right graph: As above, but with fixed $\Lambda = 1.3$ and variable $\phi = \pi/4 \pm n\pi/80$ with $n = -3, -2, -1, 0, 1, 2, 3$ (bottom to top at $\psi = 0$).

made for different orientations of the field in the *ab*-plane. Consider first the low field linear limit, where the *effective* penetration depth with respect to the angle ψ is just $\lambda_{lin} = \lambda_a \sin^2\psi + \lambda_b \cos^2\psi$. At $\psi = 45°$ a measurement of $\Delta\lambda(T)$ would *see* the average temperature dependence of $\Delta\lambda_a$ and $\Delta\lambda_b$, as expected. One might then expect that for the NLME with H is along the nodes, a measurement of $\Delta\lambda_{45}(H)$ would simply be $\sqrt{2}$ times the average of $\Delta\lambda_a(H)$ and $\Delta\lambda_b(H)$. While this is true for a tetragonal crystal, it is not true in general. For something like $YBa_2Cu_3O_{7-\delta}$, Figure 3.7 shows that it *may* be incorrect to interpret these measurements in such a simple fashion.

3.4.4 Harmonic Generation and Intermodulation

As will be discussed in Chapter 4, the quantity an ac susceptometer actually measures is the magnetic moment m of the sample. To extract the penetration depth from such a measurement, one must first appropriately model m in terms of λ. For thin platelets of single crystal $YBa_2Cu_3O_{7-\delta}$, this is done be treating the sample as a thin slab. The magnetic moment of a slab shaped superconductor of thickness $t \gg \lambda$ in a field H can be written as $m = -H(V - 2A\lambda)$, where V is its volume and A its area. It is clear from this that a field dependent penetration depth will lead to a nonlinear magnetic moment. Furthermore, if $H(t)$ is sinusoidal then $m(t)$ will acquire higher harmonic components, and if the applied field has the form $H(t) = H_1(\cos(\omega_1 t) + \cos(\omega_2 t))$, the nonlinearity of the material would give rise to intermodulation products, most notably the third order intermodulation terms at frequencies $2\omega_1 - \omega_2$ and $2\omega_2 - \omega_1$. (See Appendix B for a more complete treatment of this model.) With this in mind, Dahm and Scalapino [37] proposed that as a possible alternative one could probe the third harmonic response of the superfluid for the existence of the low temperature peak in $\beta(T)$, which is a signature of the d-wave NLME (see Section 3.4.1). They also suggested that intermodulation could be used for the same purpose. Their proposals were partly intended to motivate the search for the NLME in high-T_c thin films, since microwave filter circuits made from these thin films were already tested for harmonic generation and intermodulation as a routine characterization of their performance. (In fact, much of the work by Dahm and Scalapino [36], was motivated by modeling the behaviour of such filters assuming a field dependence of λ given by the Yip and Sauls theory.)

Žutić and Valls [44] examined harmonic generation in the transverse magnetic moment $M_\perp$ within the context of the NLME. They discussed how ac measurements could be performed so as to enhance and maximize the nonlinear signal expected from the Yip and Sauls theory. In particular, they found it would be most favourable to measure the third harmonic of $M_\perp$ if there was little or no superimposed dc field, and the second harmonic if the superimposed dc field was larger than or equal magnitude to the ac field.

3.5 Overview of Experimental Results on the NLME

Experimental studies of nonlinear electrodynamics in superconductors date back to measurements of the magnetic field dependence of the microwave surface impedance of tin by Pippard in 1950 [48]. Spiewak in 1958 measured an H^2 dependence in the surface reactance (and hence λ) of single crystal wires of tin [49], which Bardeen suggested could possibly be explained by his idea of a counterflow of normal fluid [32].[3] Garfunkel built on this idea, and tried to try to explain a host of experiments done on conventional superconductors in the 1960's [50] by means of a quasiparticle energy shift, $\mathbf{p} \cdot \mathbf{v}$. Of course, Yip and Sauls based their theory of the Nonlinear Meissner Effect on this idea as well.

3.5.1 Single Crystals

The scattered results that predate the Yip and Sauls theory are not of much interest here. This is primarily because the work was done exclusively on type I conventional superconductors where the local electrodynamics of the NLME are not valid. The one exception is a measurement by Sridhar *et al.* [51] on a $YBa_2Cu_3O_{7-\delta}$ single crystal in 1989. They observed a quadratic field dependence in λ that increased with temperature in a manner that the authors interpreted as being consistent with conventional BCS superconductivity. In fact, their observations of $\Delta\lambda(T)$ and $H_{c1}(T)$ also appeared to be consistent with an s-wave description, which is now known to be incorrect for the cuprates. Sample quality of high-T_c superconductors in 1989 was generally not good enough to reveal much of what is known today about the intrinsic behavior of these materials, and it is most certain that the crystals used here (by virtue of their $\Delta\lambda(T)$) were also of poor quality. As a result, these early measurements on $\Delta\lambda(H)$ can no longer

[3]Even though Bardeen did not expand on this idea himself, it is quite interesting to see that the point of creation for the idea of a NLME was a couple of sentences from his 1958 paper.

be regarded as meaningful.

The first specific study of the NLME came in 1995/96, when Maeda *et al.* [52] published results for $\Delta\lambda(H)$ in the high-T_c compounds $Bi_2Cu_2CaCu_2O_y$, $YBa_2Cu_3O_{7-\delta}$, and $Tl_2Ba_2CaCu_2O_y$. Work in the same group was also done on the electron-doped cuprate $Nd_{1.84}Ce_{0.16}CuO_4$ [53], as well as the conventional type II superconductor V_3Si [54]. In the three hole-doped high-T_c materials, the behaviour of $\Delta\lambda(H)$ appeared to be qualitatively consistent with several aspects of the Yip and Sauls theory. These are: (1) at low temperatures there was a linear field dependence in $\Delta\lambda$, (2) the linear behaviour in this regime crosses over to quadratic at low fields, and (3) the temperature dependence of the coefficients of both the linear and quadratic terms, as well as the temperature dependence of the cross-over field between the two regimes, were all consistent in form with the theory. However, despite the seeming success of these results, there are several points of contention that must be raised. First, the resolution of the experiment was only ~ 20 Å, and the size of the effect quoted here was typically an order of magnitude larger than the zero temperature prediction [30] of $10 - 15$ Å over the entire field range up to H_{c1}. Next, the lowest temperature at which these experiments were carried out was 10 K, where as the theory would suggest that the linear $\Delta\lambda(H)$ could not be seen above 2 K [30]. And lastly, the measurement geometry used here had the applied fields perpendicular to the plane of the crystals, resulting in a large demagnetizing effect that could easily drive flux into the sample along its edges. Independent measurements on $YBa_2Cu_3O_{6.95}$ (by Tony Carrington [55] and our group [56]) several years later confirmed that, at least for the YBCO system, Maeda's result were certainly due to some extrinsic effect and could not be representative of the NLME. While this finding does not necessarily negate his results on $Bi_2Cu_2CaCu_2O_y$ or $Tl_2Ba_2CaCu_2O_y$, it does give cause for skepticism.

The results for $Nd_{1.84}Ce_{0.16}CuO_4$ and V_3Si were also claimed to be consistent with the NLME for a $d_{x^2-y^2}$ and s-wave superconductor respectively. However, similar concerns exist here; primarily, that the measurement geometry used results in a large demagnetizing effect which could lead to flux entering the sample at its edges. For example, the results for V_3Si were 20 times larger than prediction [30], and may actually be an extrinsic signal associated with flux entry. It has been shown experimentally [56, 57], and will be discussed in detail in Chapter 5, that even in the case where the demagnetizing effects are small and the field levels are very low, data can still be contaminated by flux entry. Another concern is that data was only taken at temperatures as low as 7 K, and given that T_c is around 20 K for both materials this may not be sufficiently low to make a stringent test the NLME.

The measurements of $\Delta\lambda(H)$ in $YBa_2Cu_3O_{6.95}$ by Carrington [55] and Bidinosti [56] from 1999 are shown in Figure 3.8. Both groups developed precision measurement techniques that had a resolution of about $\delta\lambda \sim 0.1$ Å for a crystal area of $1-2$ mm^2 and with the field applied in the plane of the sample. This represented a very significant advance in the experimental study of the NLME: the ability to make in-plane measurements minimized possible problems associated with a large demagnetizing factor and allowed the possibility of examining $\Delta\lambda(H)$ as a function of field direction, which is the main tenet of the Yip and Sauls theory. Also, there was an increase in resolution[4] by a factor of ~ 200 with these new techniques. Both groups measured a $\Delta\lambda(H)$ at ~ 1.2 K that agreed well with the theory (at that temperature), in stark contrast with the results of Reference [52] that were much too large. However, both groups also noted that $\Delta\lambda(H)$ increased with temperature (see, for example, the data from Carrington *et al.* [55] in Figure 3.8) which does not agree with the NLME. Bidinosti *et al.* [56] also found further discrepancy with theory in their measurements on the angular dependence of $\Delta\lambda(H)$.

[4]The actual improvement in sensitivity is much higher, because the effective volume of the superconductor will scale with the demagnetizing factor. For example, in Reference [52] the typical crystal volume was $1 \times 1 \times 0.3$ mm^3 giving a typical demagnetizing factor $1/(1-N) \sim 25$; the quoted resolution here was 20 Å. Therefore, these high precision measurements (where $1/(1-N) \sim 1$) actually offer a sensitivity greater by a factor of $\sim 20/0.1 \times 25 \sim 5000$.

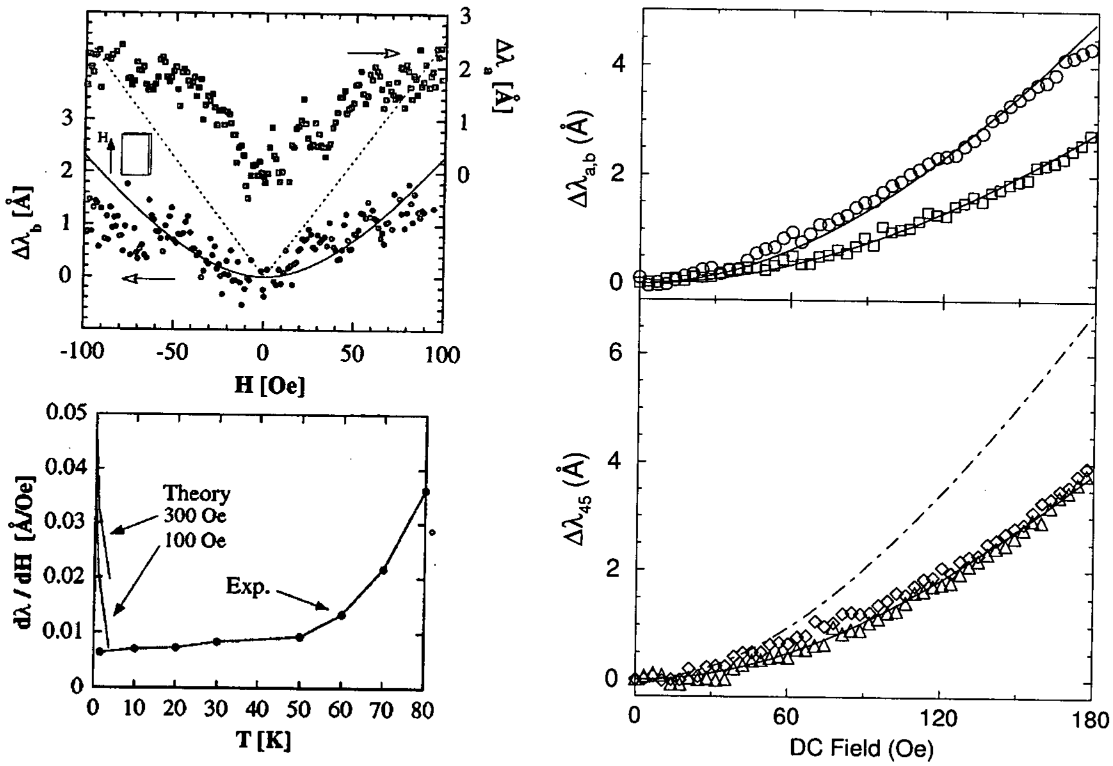

Figure 3.8: Precision measurements of $\Delta\lambda(H)$ in $YBa_2Cu_3O_{6.95}$. Left: $\Delta\lambda_{a,b}$ at 1.4 K with theoretical fits for 0 K (dashed line) and 1 K (solid line); temperature evolution of $d\lambda/dH$ (from Carrington *et al.* [55]). Right: $\Delta\lambda_a$ (circles) and $\Delta\lambda_b$ (squares) at 1.2 K with theoretical fits; $\Delta\lambda_{\pm 45}$ (diamonds, triangles) at 1.2 K with theoretical prediction (dashed line), and average of curves in top panel (solid line) (from Bidinosti *et al.* [56]).

Here, it was found that the field dependencies of λ for fields applied $\pm 45°$ to the crystal axes (ie. H roughly parallel the nodes), were exactly the average of the results for fields along the crystal axes (ie. H parallel antinodes). The enhancement expected in the nodal direction was not seen and, ignoring the possible effects of orthorhombicity, it was concluded that NLME of Yip and Sauls was suppressed by a factor of the order of 10 or larger. (In light of the subsequent work by Haltermann and Valls [46, 47] discussed in Section 3.4.3, this conclusion will be re-examined in Chapter 6 along with a full analysis of all our measurements.)

A complementary experimental test of the NLME has been carried out by a group at the University of Minnesota on the angular dependence of the transverse magnetization $M_\perp$. In this experiment, on which they have worked since 1994, the sample is rotated in fixed field while measurements of the magnetic moment are made in the direction perpendicular to the field (the predicted angular depedence of $M_\perp$ is the same as τ shown in Figure 3.3). Early results for $LuBa_2Cu_3O_{7-\delta}$ did not support a pure d-wave pairing state, but measurements were dominated by the geometric demagnetization factor and trapped flux [58]. Subsequently, efforts were made to alleviate the problems associated with sample geometry[59], and improved measurements of $M_\perp$ for a disk shaped single crystal of $YBa_2Cu_3O_{6.95}$ were published by Bhattacharya *et al.* [60] in 1999. Within their experimental uncertainty, they did not observe the 4-fold symmetry in $M_\perp$ expected for the NLME in a $d_{x^2-y^2}$ superconductor, and concluded a 30% suppression in the theoretical prediction. While one cannot easily compare the sensitivity of the $M_\perp$ measurements to $\Delta\lambda(H)$ measurements, results from both types of experiment should ultimately complement each other under a single consistent explanation. At the moment, there is at least a consistent observation (between the precision measurements of Carrington [55], Bidinosti [56] and Bhattacharya [60]) that for single crystal $YBa_2Cu_3O_{6.95}$ the Nonlinear Meissner Effect, if present, is a much weaker effect than predicted.

3.5.2 Thin Films

There has also been research done on the nonlinear electrodynamics in high-T_c thin films and thin film devices, which, for the sake of completeness, should be mentioned here as well. Theoretically, the use of thin films has been proposed for the direct study of the NLME [30, 37], however it has been more typical to investigate nonlinearities in thin films from a very practical point of view. This leads to the opposite approach where the behaviour of a certain thin film device is modelled on the supposed existence of the NLME. For example, this has been done for microstrip resonators [36, 61, 62] and disk resonators [63]. Experimentally, the situation is somewhat similar in that the emphasis of most research is to characterize a certain device or thin film material, rather than to explore the fundamental intrinsic properties of the material itself. A notable exception is the work on THz nonlinear transmission in BSCCO films by Orenstein *et al.* [64], which was intended as a direct study of the NLME. They concluded that the nonlinear transmission was a result of an intrinsic, supervelocity induced, pairbreaking mechanism. However, they did not see the expected $1/\sqrt{2}$ anisotropy of the Yip and Sauls theory, which leaves some doubt as to whether this could be the mechanism responsible for their results.

A survey of some other pertinent experiments is as follows. Willemsen *et al.* [65] observed 2:1 behaviour[5] in the intermodulation products of TBCCO and YBCO microstrip resonators at temperatures between 25 and 77 K. They noted that 2:1 behaviour can arise from a linear $\lambda(H)$, but they concluded that it would be unlikely at these elevated temperatures for this to have come from the NLME. They suggested weak links as the possible origin for the nonlinearity, which has support from other measurements performed on TBCCO films [66]. On the other hand, Booth *et al.*. [67] saw 3:1 behaviour in YBCO transmission lines, and Classen *et al.* [68] measured a quadratic dependence of λ on the current density in YBCO films at 77 K. They found the effect to be larger than could be explained by either BCS theory or the NLME, and suggested planar defects as the possible source of the nonlinearity. More recently, there has been some direct research into the origin of the nonlinear electrodynamic response of YBCO films: one study concluded that it was vortices in weak links, as well as lattice distortions in grains and at grain

[5] See, for example, the analagous situation for a slab superconductor worked out in Section B.2 of Appendix B. The definitions of 2:1 and 3:1 behaviour are also given here.

boundaries that were responsible [69]; another study cited only vortices in weak links as the most important source of nonlinearity [70]. This all goes to suggest that at the present thin films are probably not as useful as single crystals for studying the Nonlinear Meissner Effect. In many ways, the situation here is reminiscent of early temperature dependent measurements, where high-T_c thin films still tended to show a T^2 dependence in $\Delta\lambda$ at low temperatures, while single crystal quality had already sufficiently progressed so as to exhibit the linear $\Delta\lambda(T)$ intrinsic to a $d_{x^2-y^2}$ superconductor [24].[6] As a result, one is hard pressed not to conclude that the intrinsic nonlinear response of high-T_c materials will first be sorted out in single crystals, and that research on the NLME must focus on this avenue.

[6]Eventually, thin flim quality did improve and began to show this characteristic as well.

Chapter 4

AC Susceptibility and the AC Susceptometer

As mentioned in Chapter 2, microwave cavity perturbation has proven to be a popular and successful technique for studying the electrodynamics of high-T_c superconductors [24, 71]. However, high precision measurements of the surface resistance and magnetic field penetration depth in these materials usually requires the use of high Q superconducting resonators, which then limits experiments to low microwave power and zero dc field. The growing body of theoretical work described in Chapter 3 has provided strong impetus to study the nonlinear electrodynamic response of superconductors in the Meissner state, thereby pushing researchers to develop techniques that can operate in finite magnetic field and yet maintain the high sensitivity of cavity perturbation. Recently, three different experimental approaches have been taken to meet this difficult challenge: a SQUID susceptometer [60], a tunnel diode oscillator [55], and the ac susceptometer designed and built by Walter Hardy and myself [56, 57] as the research apparatus used in this thesis.

The use of ac techniques to study superconductor electrodymanics dates back to Shoenberg in 1937 [72], and the simplicity of ac susceptibility measurements naturally lends itself to the study of high-T_c materials [73], particularly the strong diamagnetism associated with their superconductivity. However, to the best of our knowledge, no ac susceptometer (prior to this one) has had the resolution necessary to detect the small changes in the penetration depth in single crystals that are relevant to the interesting physics. This chapter describes in detail the principles of the technique, the design of our high precision ac susceptometer, and the method in which it is used to measure $\Delta\lambda$

as a function of temperature and magnetic field.

4.1 Principles of the Technique

The macroscopic magnetic field in the presence of a material of magnetization $\boldsymbol{M}$ is given as $\boldsymbol{B} = \mu_o (\boldsymbol{H} + \boldsymbol{M})$. In general, M is a function of H, and the two are related through the magnetic susceptibility χ. For linear media in a dc field this relationship is simply

$$\chi = \frac{M}{H} \tag{4.1}$$

For nonlinear media or in the case where one applies a time dependent field a more relevant definition is

$$\chi = \frac{\mathrm{d}M}{\mathrm{d}H} \tag{4.2}$$

where χ is now referred to as the differential or ac susceptibility.

Consider the latter case where a sample is in a periodic external magnetic field $H(t) = H_{dc} + H_1 e^{i\omega t}$. In response to the field, the sample will develop a periodic magnetization $M(t)$, which can be expressed as a Fourier series

$$M(t) = H_1 \sum_{n=0}^{\infty} M_n e^{in\omega t} \tag{4.3}$$

From the definition of the ac susceptibility in Equation 4.2,

$$\begin{aligned} \frac{\mathrm{d}M}{\mathrm{d}H} &= \frac{\mathrm{d}M(t)}{\mathrm{d}t} \left(\frac{\mathrm{d}H(t)}{\mathrm{d}t} \right)^{-1} \\ &= \sum_{n=1}^{\infty} nM_n \, e^{i(n-1)\omega t} / H_1. \end{aligned} \tag{4.4}$$

Each coefficient nM_n/H_1 is identified as $\chi_n = \chi_n^{'} - i\chi_n^{''}$, the complex magnetic susceptibility of the nth harmonic, and will be given by

$$\begin{aligned} \chi_n^{'} &= \frac{\omega}{\pi H_1} \int_{\frac{-\pi}{\omega}}^{\frac{\pi}{\omega}} M(t) \cos n\omega t \, \mathrm{d}t \\ \chi_n^{''} &= \frac{-\omega}{\pi H_1} \int_{\frac{-\pi}{\omega}}^{\frac{\pi}{\omega}} M(t) \sin n\omega t \, \mathrm{d}t \end{aligned} \tag{4.5}$$

The fundamental component of the magnetization $M(t) = H_1(\chi_1^{'} \cos\omega t + \chi_1^{''} \sin\omega t)$ has a real part in-phase with the applied field $H(t)$ and an imaginary part that is 90° out-of-phase with $H(t)$. This attaches very obvious physical meaning to the fundamental susceptibility: $\chi_1^{'}$ corresponds to the inductive response (energy storage) of the sample, and $\chi_1^{''}$ corresponds to losses (energy dissipation) in the sample. The higher harmonics are generally associated with hysteresis and nonlinearity in the magnetization [74].

For example, a superconductor in the full Meissner state will have a magnetization that is of equal amplitude but opposite direction to that of the applied field. From Equation 4.5 this gives $\chi_1^{'} = -1$ and $\chi_1^{''} = 0$ reflecting the *perfect diamagnetism* and *perfect conductivity* of the material. In the normal state (neglecting core diamagnetism and the real conductivity), the external field will completely penetrate the sample, and $\chi_1^{'} = \chi_1^{''} = 0$. At intermediate temperatures $\chi_1^{'}$ will be a negative number (> -1), and $\chi_1^{''}$ will be a small positive number reflecting ac losses [75].

A typical experimental set-up for measuring ac susceptibilities is shown in Figure 4.1. In general, the ac susceptometer is comprised of a set of co-axial coils: a primary coil to produce a small ac magnetic field, a dc coil to produce a superimposed dc magnetic field, and a pair of secondary coils across which an induced voltage signal is detected. The secondary coils are wound as identically as possible and connected in series with opposite polarity, so that in the absence of a sample the total voltage across the pair will be close to zero. With a sample present, this coarse voltage compensation leads to an output signal that is directly proportional to the time rate of change of the sample's magnetization:

$$v(t) \propto \mathrm{d}M/\mathrm{d}t$$

The voltage compensation circuit is present to null out any inherent voltage imbalances (for example due to coil imperfections), but more importantly to remove the bulk signal of the sample itself thereby allowing precise measurements on very small changes in its magnetization or susceptibility. For the research done in this thesis, focusing on the NLME in $YBa_2Cu_3O_{7-\delta}$, it is most essential to directly relate the voltage measured at the lock-in amplifier to a change in penetration depth λ rather than M or χ. The manner in which this is done will be discussed in Section 4.4.

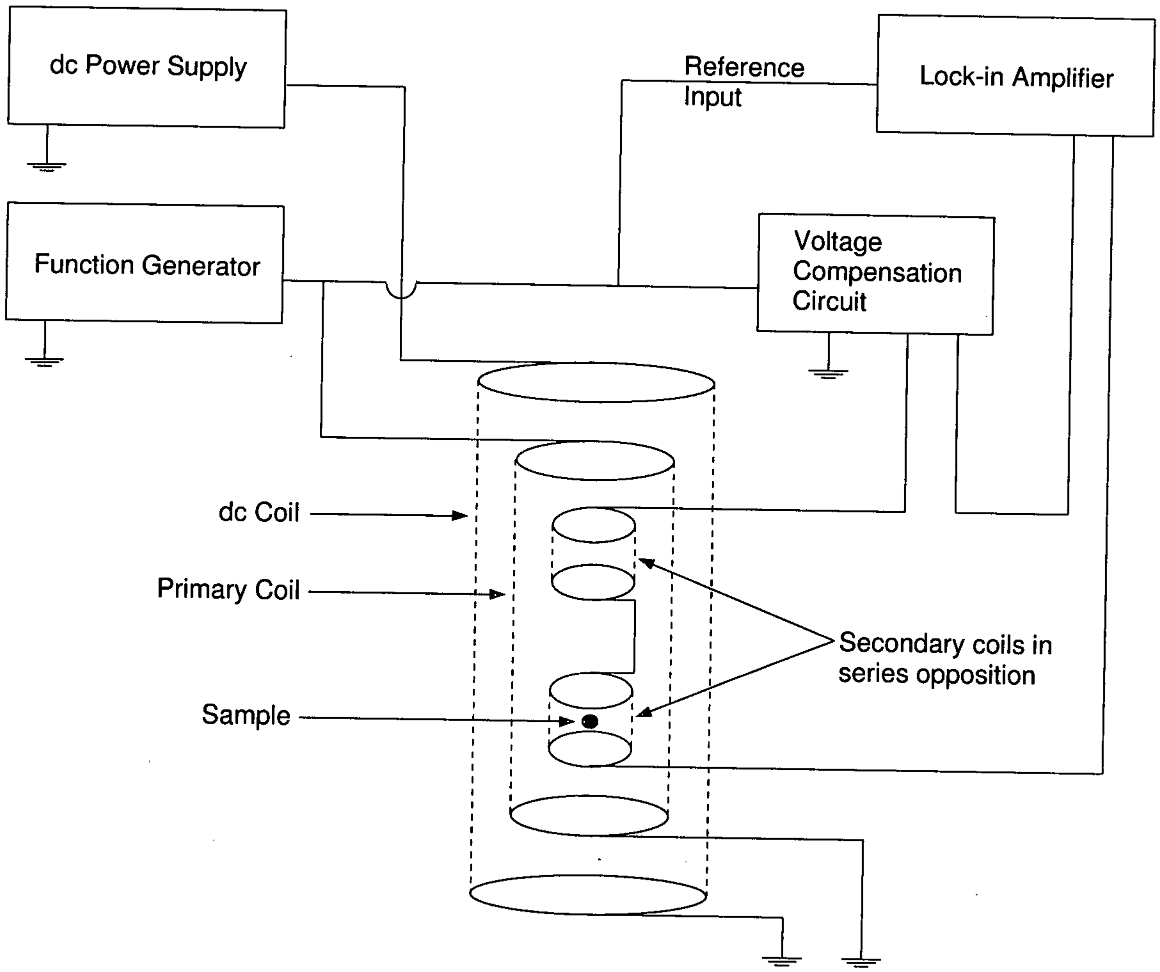

Figure 4.1: The general experimental set-up for ac susceptibility measurements.

4.2 Design and Construction of the ac Susceptometer

The first step towards achieving good resolution with an ac susceptometer is to have a high degree of symmetry in the arrangement of the coils with respect to each other and their immediate surroundings. This is shown in Figure 4.2: the center of the primary coil coincides with the center of the dc magnet, the two inner secondary coils are spaced symmetrically about this center point, and all coils share the same central axis. In addition, the copper flange that holds the primary coil has been made with a central bore that resembles the sample aperture in the dc coil form. These steps ensure that each secondary coil will *see* the same applied field, and therefore produce induced voltages of equal magnitude that cancel in the absence of a sample. It should be noted that the skin depth in the copper at 12 kHz and 4 K is about 70 μm, which is much smaller than the dimensions of the components themselves.

To measure $\Delta\lambda$ as a function of temperature, the sample is thermally isolated from the rest of the apparatus by mounting it on a slender sapphire plate in vacuum (see Figure 4.2). This is a popular and widely used technique [76]. A small quantity of Dow Corning high vacuum grease is used to hold the sample in place. The plate, which is 0.1 mm thick, roughly 0.8 mm wide and 2.5 cm long, is held in place on a sapphire block, also with vacuum grease. A 220 Ω chip resistor and a Cernox$^{\mathrm{TM}}$ resistor [77] mounted on the underside of this block act as sample heater and thermometer respectively. A thin quartz tube forms the thermal break between the sample system and a copper base that is in contact with the helium bath at $T_B = 1.2$ or 4.2 K.

A much more problematic aspect of the susceptometer design concerned the ablity to make measurements of $\Delta\lambda$ as a function of field. As Figure 4.2 clearly shows, it is not possible to avoid exposing certain parts of the apparatus to the exciting fields. It was important, therefore, to use only *nonmagnetic* materials in the construction of the

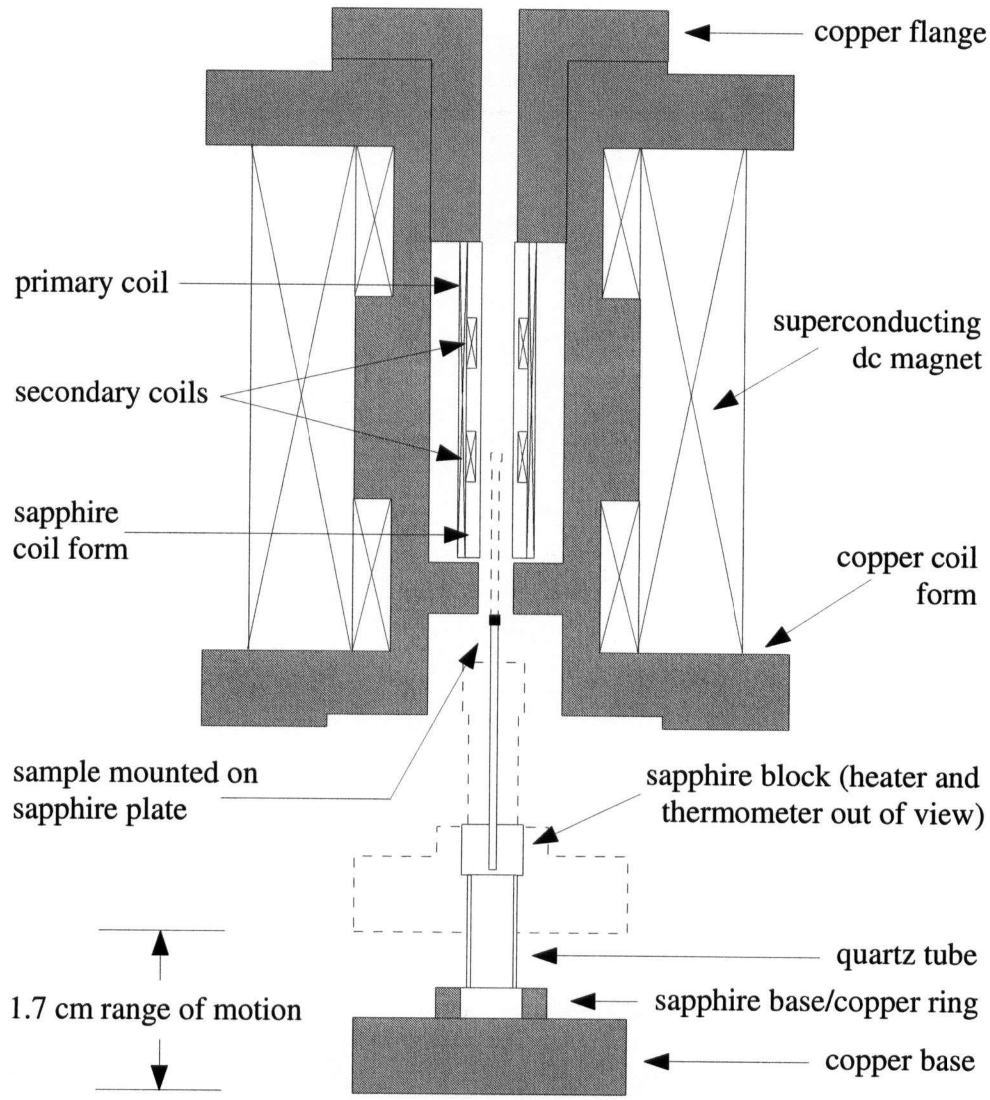

Figure 4.2: The ac susceptometer design. The ac susceptometer is constructed only from materials with very small magnetic susceptibilities. The sample is shown fully extracted from the secondary coil; the dashed outline shows the sample in the measurement position.

susceptometer to limit any field dependent background. To this end the following steps were taken: copper was used for all metallic parts in the region of the coils, the copper parts were etched with nitric acid after machining to remove any contamination from steel tools, and the primary and secondary coils were wound from high purity wire on a high purity sapphire form (specific details are given below in Section 4.2.1). However, at the level of sensitivity required for our measurements, these steps alone did not sufficiently suppress a field dependent background signal, and to overcome this problem a custom made retractable sample holder was developed. The mechanism providing the linear motion was an adaptation of a compound linear spring [78], and is described in greater detail in Section 4.2.2. A range of motion of about 1.7 cm was enough to fully *extract* the sample from the ac susceptometer. At this distance the magnetic coupling of the sample to the system is reduced by over five orders of magnitude to a level not detectable above the noise. This allows an immediate determination of the background signal which can then be properly subtracted from the data.

4.2.1 The ac Coil Set

Important details of the ac coil set are shown in Figure 4.3, which gives a schematic view of its construction, along with the field profile of the primary coil. Here the copper flange, shown in full in Figure 4.2, is shown cut away. Stycast 1266 epoxy was used to butt join the sapphire form to the copper flange and to hold all coil windings in place. The coil form, precision ground from very high quality sapphire [79], is 0.64 cm in diameter, has a central bore of 0.32 cm to accept the sample, and two grooves, 0.76 mm deep and 0.50 cm wide, in which the secondary coils were wound. A picture of the actual piece with the secondary coils in place is shown in Figure 4.4. High purity niobium wire [80] was used for these coils with the idea that a) any contaminants within the wire would be magnetically shielded by the Meissner state screening of the niobium and b) the applied

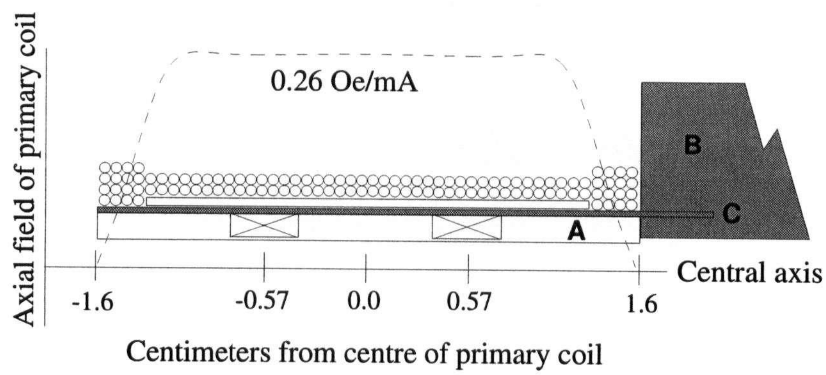

Figure 4.3: The construction of the ac coil set. (A) sapphire coil form; (B) copper flange; (C) Faraday shield

fields to be used in this experiment would not be large enough to disrupt this Meissner state. Immediately covering the sapphire coil form is a Faraday shield, which reduces the capacitive coupling between the primary and secondary coils. The shield was constructed from the same high purity copper wire [80] used for the primary coil, and was made by winding a single layer on a large diameter teflon form and setting it in 1266 epoxy. Before the epoxy fully cures, this coil is cut perpendicular to the windings and freed from the form to leave a fairly flexible sheet of parallel wires electrically insulated from each other. The sheet is epoxied around the sapphire form such that the wires run along the length of the form; silver epoxy electrically grounds the Faraday shield inside a groove in the copper flange. The primary coil is a continuous winding of 4 layers sitting directly on top of the Faraday shield. The first and fourth layers have windings only on either end; a mylar spacer supports the second and third layers which are complete. The field profile of such a coil design is both symmetric about the secondary coils and homogeneous over their length.

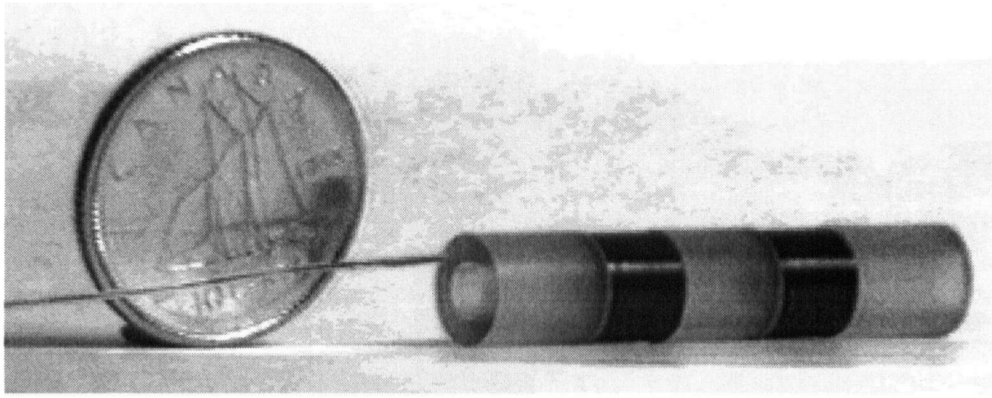

Figure 4.4: Secondary coils wound on the sapphire coil form. The coil leads, protected inside a teflon tube, extend from the coil form.

4.2.2 The Retractable Sample Stage

The motion of the sample stage must be very linear to successfully extract (and replace) the sample from within the small bore of the sapphire coil form. The low operating temperature of the apparatus (1.2 or 4.2 K) presents the further difficulty of increased friction, which makes the use of sliding parts a poor design choice. Both these concerns were overcome by the designing of a retractable stage based on the principles of the compound linear spring [78] shown in Figure 4.5. The diagram shows a side view of the spring; the two slabs **A** and **B** are connected to each other and to a base stand by two sets of flexures. When **A** is pushed horizontally it travels in that direction confined to a single plane. There is no vertical translation of **A** as the bending of the two sets of flexures exactly compensates for the other, and there is no rotation since the flexures run the entire width of the slabs.

A photograph of the retractable sample stage is shown in Figure 4.6 held in a vice; the wall of the vacuum pot (which bolts to the bottom of the dc magnet in Figure 4.2) has been removed to expose the compound spring. The spring sits on its side to provide

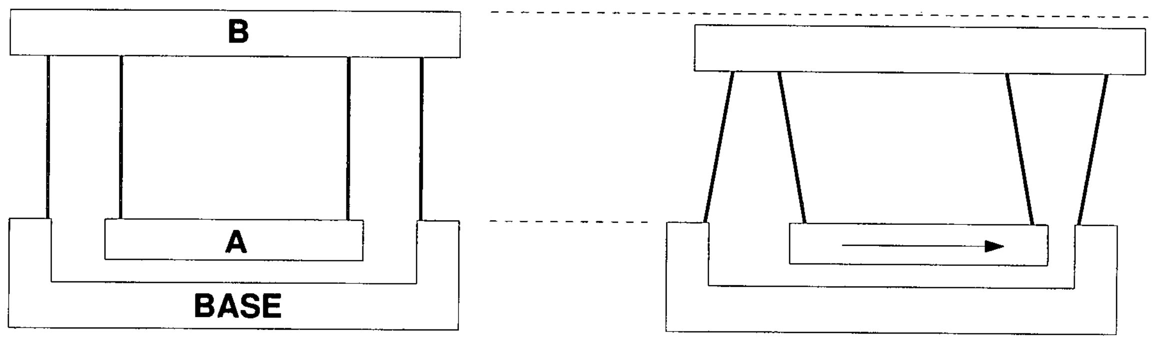

Figure 4.5: Diagram of a compound linear spring.

linear motion in the vertical direction. The main parts of the spring are labelled as per Figure 4.5. Holes were drilled out of the brass components of the spring to remove excess weight. The flexures are 0.4 mm thick strips of stainless steel foil soldered into the edges of the thin brass plates. The motion comes from a brass rod that pushes at the centre of the copper base on which the sample stage sits; in this way the presence of the spring is really just to constrain the motion of the stage to a straight line. A simple lever actuated from outside the dewar is what moves the push-rod. Also in view in the photograph are: the sample stage (showing the sapphire sample block and thermometer, the quartz tube and the copper ring and base from Figure 4.2), heavy braids of copper wire to thermally connect the copper base to the helium bath, a feed-through for the electronics, and a copper bellows to maintain vacuum inside the pot while allowing movement of the push-rod.

4.3 Electronic Circuitry

The method of voltage compensation and detection is shown in the circuit diagram in Fig. 4.7. The current through the primary coil is driven by a Hewlett-Packard 3324A function generator via a 100 Ω resistor, which dominates any small resistance changes

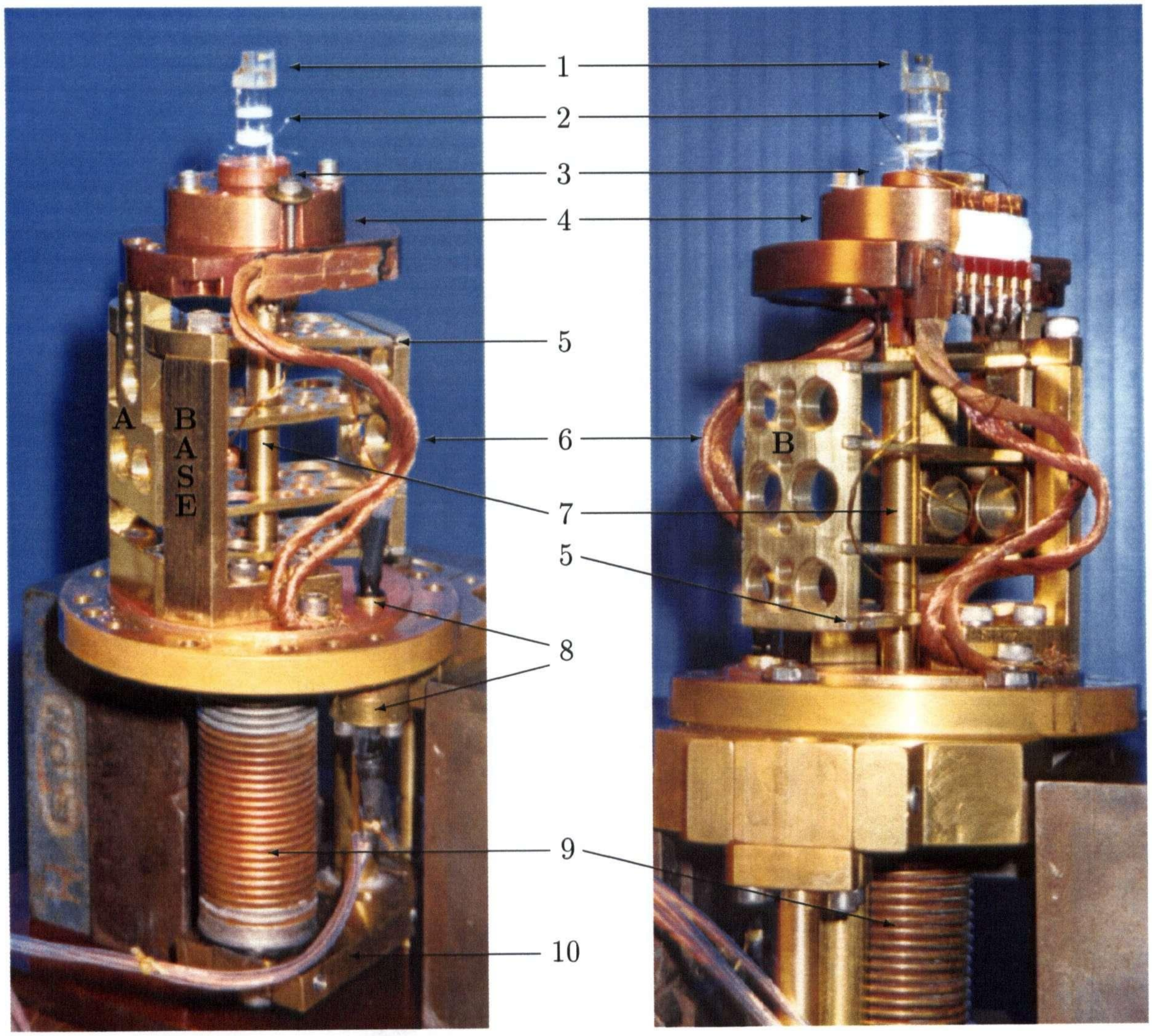

Figure 4.6: The retractable sample holder; the components of the compound linear spring are labeled as per Figure 4.5. (1) sapphire mounting block (thermometer is chip in view); (2) quartz tube (white bands are string tying down electrical leads); (3) copper ring (sapphire base out of view); (4) copper base; (5) flexures; (6) copper braid; (7) push rod; (8) electrical feed through; (9) bellows; (10) lever

in the primary circuit, thereby providing a relatively constant current. Also in series with the primary coil are a small resistor and a small inductor across which voltages V_i and V_o, in- and out-of-phase with the drive current respectively, are *picked off* to be used for voltage compensation. Each of these voltages is input to an Electro Scientific Industries DT 72A decade transformer (not shown), which can provide seven orders of voltage resolution. The output voltages, V_i and V_o, from the decade transformers provide the final fine compensation needed to null the signal from the sample's bulk magnetization and any other imbalances due to small imperfections in the winding of the coils. The compensation voltages are injected into the secondary circuit across the 16 Ω resistor via two small ferrite core transformers and two 420 Ω resistors. These large resistors are present to dominate the resistance of the leads which change with cryogen level and would otherwise result in a substantial drift signal. The remaining components in series with the secondary coils are a 62 nF capacitor and a shielded toroidal transformer. The susceptometer is operated at 12 kHz, the resonant frequency of the secondary coils/capacitor combination, used to remove the large inductive impedance of the coils from the circuit. The cooled transformer provides very low noise voltage amplification of the signal before it goes to a Princeton Applied Research 119 preamp. The transformer is wound on an amorphous metal core [81] and magnetically shielded inside a superconducting can. As many electrical components as possible were housed at liquid helium temperatures to limit thermal noise. The remaining components at room temperature were mounted on an aluminum bed thermally regulated by a water bath and housed inside a styrofoam container to provide further stability.

It is important to note that current flowing in the secondary coils can substantially alter the field applied by the primary. Such effects are largely avoided by the combination of using a high impedance amplifier and working close to a null in the voltage presented to the amplifier. The largest *off-null* signal is incurred during calibration (see Section 4.4)

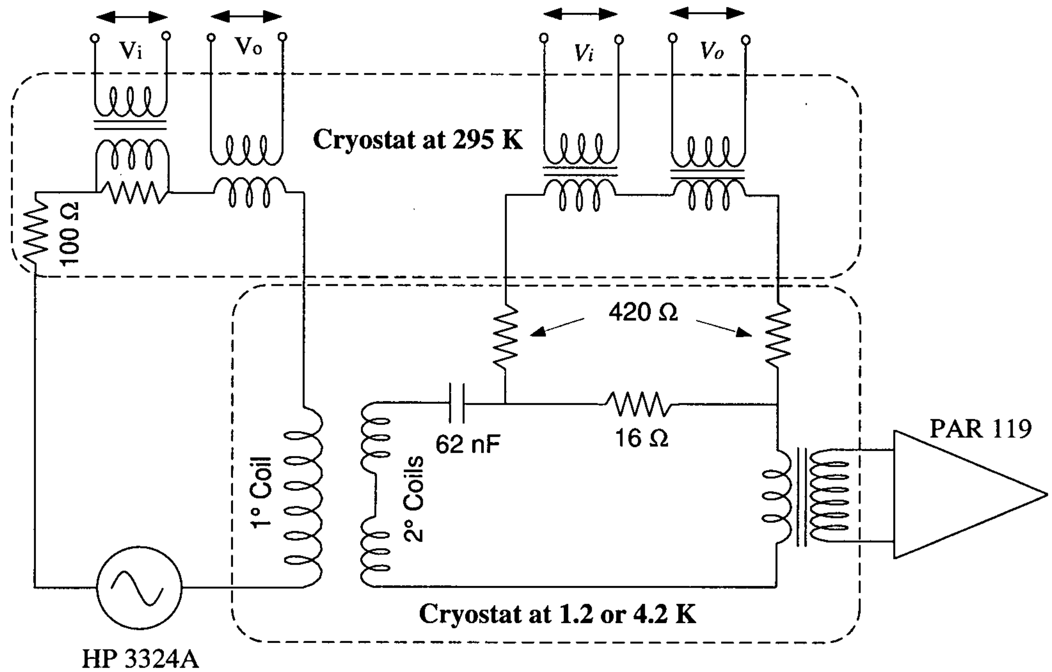

Figure 4.7: The circuit diagram of the ac susceptometer.

where the full magnetic volume of the sample is detected. This results in a reduction in the primary field of approximately $V_s/V_c \times X_L/Z_S$, the ratio of the sample to pick-up coil volumes times the ratio of the pick-up coil reactance to secondary circuit impedance, and is about 1 % for a large $YBa_2Cu_3O_{7-\delta}$ single crystal ($V_s \sim 2$ mm$^2 \times 0.1$ mm). The use of a series resonance as opposed to a parallel resonance to tune out the reactive impedance of the secondary coils is imperative; a parallel resonance would result in a large current flowing in the secondary with the consequence that the total applied field would be much larger than the primary H (and of opposite sign). Of course, resonating the secondary coils also changes the phase of the signal, but this is taken care of by the *in situ* phase setting and calibration process described below.

4.4 Calibration and Phase Setting

The signal from the preamp is detected using a Stanford Research Systems SR850 lock-in amplifier, which has two outputs, X and Y, for simultaneous measurements in quadrature. The most accurate and convenient way to set the phase of the lock-in is to use the large diamagnetic signal of the superconducting sample itself. With the sample held at base temperature, either 1.2 or 4.2 K, and with zero applied dc field the output signal is nulled using the decade transformers. The amplitude of the 12 kHz ac field is typically no more than 2.5 gauss peak, and at this very low temperature, field amplitude and frequency there are no losses in the superconductor. The sample is then heated above its transition temperature T_c. At 12 kHz the sample thickness t is much less than the normal state skin depth δ and therefore the net signal v_{sn} of the sample going from the superconducting state into the normal state is due entirely to the non-dissipative Meissner screening of the sample. (It should be noted that the same signal v_{sn} is found if one just extracts the sample from the ac susceptometer while it is at the base temperature.) The phase of the lock-in is adjusted so that the entire magnitude of v_{sn} appears in only one output, say output Y, which is then taken to be the inductive response of the sample (stored energy). Output X will then measure any losses. Under the conditions the desired research is to be done, losses in the sample are unmeasurable, and the following discussion focuses on the inductive response only.

Typically, single crystals of $YBa_2Cu_3O_{7-\delta}$ grow as very thin platelets. In the measurement geometry used here, the applied fields lie in the plane of the crystal and the experiment can be reasonably well approximated by the classic problem of a flat slab superconductor in a parallel magnetic field. The well known solution for the magnetic moment of such a sample is $m = -HV\,[1-(2\lambda/t)\tanh(t/2\lambda)]$, where H is the applied field, V the sample volume, and λ the magnetic field penetration depth [11]. (Development of this model and its limitations are discussed in Appendix B.) The induced voltage across the secondary coils is proportional to the time rate of change of m and so, to within a constant $1/k$, the lock-in will measure a change in voltage from the nulled position of

$$\mathrm{Y} = \frac{1}{k}\left[\lambda_2 \tanh(t/2\lambda_2) - \lambda_1 \tanh(t/2\lambda_1)\right] \tag{4.6}$$

where λ_1 is the low temperature, zero dc field penetration depth ($\simeq \lambda_0$, the $T, H = 0$ value) and λ_2 is the penetration depth after changing the sample conditions. Now, if the sample is heated above T_c, as was done when setting the phase, then $\lambda_2 \to \infty$, $\mathrm{Y} = v_{sn}$, and only a knowledge of t and λ_0 is needed to determine the calibration constant k. For $YBa_2Cu_3O_{7-\delta}$ crystals, where $\lambda_0 \sim 1500$ Å is generally much less than half the sample thickness, k reduces to the particularly simple form

$$k = (t - 2\lambda_0)/2v_{sn} \simeq t/2v_{sn} \tag{4.7}$$

Clearly, a sample of larger area A will allow better resolution, since $v_{sn} \propto V = At$. Notice also, that if $\lambda_2 << t/2$, which is true until very close to T_c, then Equation 4.6 reduces to the very simple relationship

$$\Delta\lambda = kY \tag{4.8}$$

For convenience, all measurements shown in this thesis will be converted to an equivalent $\Delta\lambda$ and quoted in units of Angstroms.

A more general calibration for a slab shaped superconductor that also includes losses associated with the normal fluid response in a superconductor is discussed in Section B.1 of Appendix B. Other calibration techniques for samples of different shapes are discussed in References [82, 83].

Chapter 5

Characterization of the AC Susceptometer

For the newly constructed susceptometer, it was of course desirable to perform a number of test experiments to see if meaningful physics research could be done with it. Making measurements as a function of temperature was rather trivial and results for $\Delta\lambda(T)$ of a $YBa_2Cu_3O_{7-\delta}$ sample could easily be checked against the penetration depth measurements done on the same sample in our lab using superconducting microwave resonators. For field dependent measurements the story was quite different. There did not exist any reliable $\Delta\lambda(H)$ measurements on high quality single crystals at the time this apparatus was constructed, so no external checks could be made. There was also the added problem that high-T_c superconductors generally have a a very small critical field H_{c1}. This meant that the very quantity under investigation, $\Delta\lambda(H)$ in the Meissner state, was naturally cut-off at some rather low field (see Figure 1.1). Furthermore this cut-off, due to the entry of vortices into the sample, is strongly dependent on the sample material, shape, temperature, and orientation within the applied field. As a result a very large part of this thesis work went towards characterizing these types of measurements. As will be shown in this chapter, we have been successful in developing the appropriate criteria by which the intrinsic field dependence of the Meissner state penetration can be measured.

5.1 Measurements as a Function of Temperature

Automated measurements of $\Delta\lambda(T)$ were made with the temperature controller (Conductus LTC-20) and lock-in (SR850) under computer control. The peak drive field was fixed at 2.5 Oersted.[1] Control experiments were done with only the sapphire sample plate and the equivalent amount of vacuum grease required to hold the sample to the plate. No signal from the magnetic susceptibilities of these materials was detected above the noise of the system.[2] However, as can be seen in Figure 5.1 there is the development of a small *radiative* signal as the temperature is raised above 50 K. This signal is associated with slight radiative heating of the ac coil set; the temperature dependence of this signal is observed to vary as $\sim T^5$ when the base temperature is 1.2 K and $\sim T^7$ when $T_B = 4.2$ K, suggesting some overall process that at least includes the T^4 of the Stefan-Boltzman radiation law. At present, a more in depth characterization and understanding of this effect is not a pressing concern. For the work to be done here, the thermal conductivity of the sapphire coil form and its contact to the copper flange is sufficient to reduce this effect to a negligible level. For example, heating from $T_B = 1.2$ K (4.2 K) to about 80 K, the radiative signal is equivalent to about a 6 Å (0.6 Å) change in λ for an averaged sized crystal, but the penetration depth of the sample itself will have typically doubled, a change of order 10^3 Å.

A collection of representative data of $\Delta\lambda(T)$ for $YBa_2Cu_3O_{7-\delta}$ is shown in Figure 5.2 and highlights the capabilities of this ac susceptometer and some of the physics that can be studied with it. The bottom left inset shows low temperature data measured with the ac susceptometer (12 kHz) alongside data on the same sample taken in a superconducting microwave cavity (1 GHz). It is clear from this plot that the former technique can achieve a resolution comparable to the microwave methods using superconducting cavities. The main graph summarizes the entire superconducting phase of $YBa_2Cu_3O_{7-\delta}$ through a plot of superfluid density fraction $(\lambda_0/\lambda(T))^2$ versus temperature. (Note: $\lambda(T)$

[1] A lower drive field of 0.4 Oersted is used near T_c to avoid prematurely driving a sample normal.

[2] One searches for this at low temperature, where the $1/T$ dependence of the Curie Law [25] would be most noticeable.

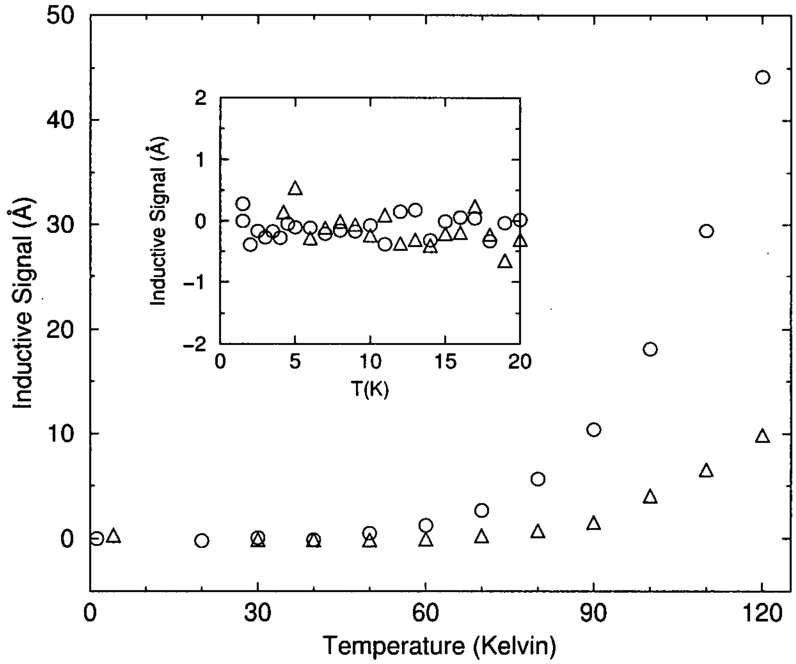

Figure 5.1: Temperature dependent signal of the empty sample holder with the ac susceptometer at 1.2 K (circles) and 4.2 K (triangles). *Radiative* signal shows dependence greater than T^4. Inset: at low temperature, no magnetic signal from the sapphire plate and vacuum grease is detected.

cannot be determined directly, only $\Delta\lambda(T)$; a value for λ_0 was taken from infrared measurements [84].) In the top right inset, data near T_c is plotted log-log as $\lambda(t)$ versus the reduced temperature $t = (1 - T/T_c)$ for the purpose of extracting a critical exponent. The data show a slope of -0.30 nearer T_c and -0.36 slightly farther from T_c. The average slope of -0.33 ± 0.03 (solid line) is similar to what has been seen in microwave measurements [85] and may suggest that the critical behavior of the superfluid density at 12 kHz follows the 3D XY universality class [86].

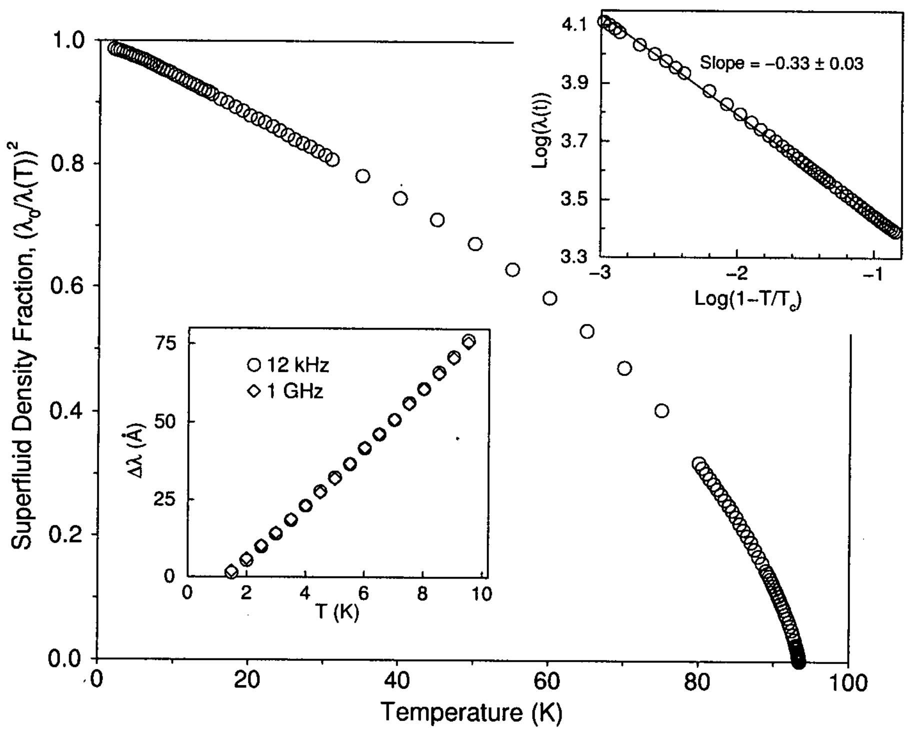

Figure 5.2: Various presentations of $\Delta\lambda(T)$ data for $YBa_2Cu_3O_{7-\delta}$. Bottom left inset: comparison with results from 1 GHz cavity. Main graph: full temperature dependence of superfluid density fraction. Top right inset: critical behavior near T_c.

5.2 Measurements as a Function of Magnetic Field

Making measurements of $\Delta\lambda(H)$ is somewhat more complicated than measurements of the temperature dependence. First, there is always a background signal and often a drift signal that must be subtracted from the raw data. Second, there are several considerations that need to be taken into account before the corrected signal can be deemed the true intrinsic field dependence of the sample's penetration depth. These points will be discussed in detail in the following sections. The general method for collecting the data is described next.

Measurements of $\Delta\lambda(H)$ are made by stepping the dc magnet current in small increments through successive cycles from positive to negative fields (using a Hewlett-Packard

6628A power supply under computer control), the peak amplitude of the ac field being kept at 2.5 Oersted. A Hewlett-Packard 3478A multimeter polls the current at each step, and for efficient signal averaging the outputs of the SR850 are read through an A/D converter (Advantech PCL-812PG interface card) directly mounted in one of the computer's expansion slots. Data collection at each current setting follows a 0.2 second pause to allow the dc field to come to equilibrium. Data from the initial loop is not kept as it may show hysteresis dissimilar to the subsequent loops. To limit the effects of a drift signal due to dropping cryogen levels, the amount of averaging at each field increment is kept short, $\sim$ 0.5 seconds, and is compensated for by repeating the cycles many times, typically 40. This repetition also has the advantage that any drift signal can be reliably fit as a function of time and subtracted out. The field dependent background, which is determined by a similar run with the sample extracted from the susceptometer, is also subtracted from the data. Provided the signal gain of the system does not change, a single background run can be used for several data runs. The gain of the system is monitored between runs by repeating the calibration process mentioned in Section 4.4. Control experiments show no detectable field dependent signal from the sapphire sample plate or the vacuum grease used to hold the sample.

5.2.1 Drift and Magnetic Field Dependent Background

A complete set of sample data collected in the manner described above is shown in Figure 5.3. The data is the *inductive* response (Y output on the lock-in) of the system; data from the *loss* channel (X output on the lock-in) is not shown here. The oscillations are hysteresis loops as they are swept out in time. A clear voltage drift can be seen in the raw data in the top graph; a numerical fit to the drift at each point is shown by the dashed line. This fit is calculated by determining the change between corresponding points in adjacent loops; this change is determined for the two points on either side of

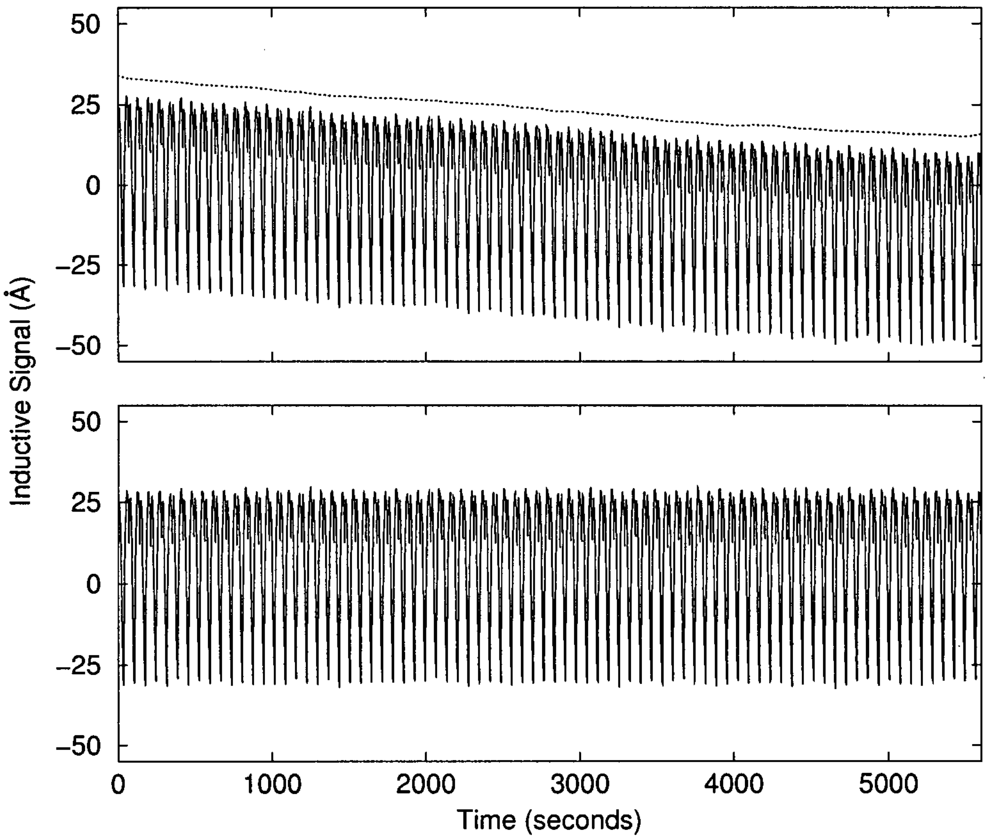

Figure 5.3: Top graph: raw data showing a drift signal; the dashed line is a numerical fit to the drift. Bottom graph: data with drift subtracted out.

the point in question as well, and an average is taken. The bottom graph of Figure 5.3 shows the data with the drift signal subtracted out. An average hysteresis loop can now be determined from this data.

Data is also collected with the sample extracted from the susceptometer to obtain the magnetic field dependent background signal. The averaged hysteresis loops for the sample data from Figure 5.3 and its background run are shown in the left graph of Figure 5.4; the two loops are offset vertically for clarity. Subtracting the background loop from the other gives the field dependent response of the sample itself, which is shown in the right graph of Figure 5.4. As was the case for this particular crystal ($YBa_2Cu_3O_{6.993}$ at 40 K),

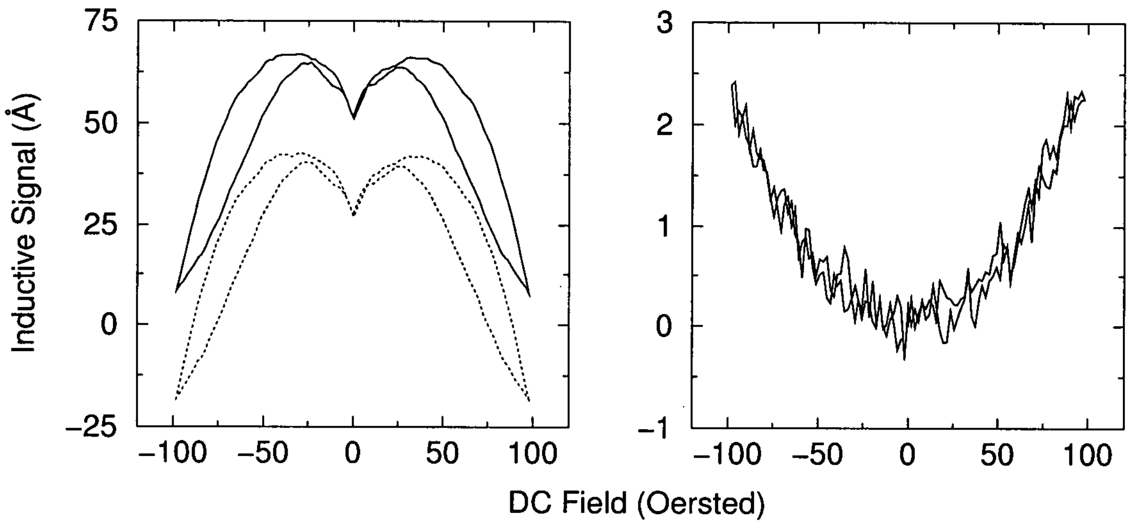

Figure 5.4: Left graph: averaged hysteresis loops for a sample run (solid line) and its background run (dashed line). Right graph: the field dependent response of the sample once the background is subtracted out.

the sample response is often hidden within a background that is larger by more than an order of magnitude. Given the amount of care taken to avoid such background signals, this fact underlines just how difficult it is to make this type of measurement.

5.2.2 Sample Hysteresis: Edge Effects

For a type II superconductor, such as $YBa_2Cu_3O_{7-\delta}$, the corrected data (background subtracted out) should not be immediately identified as $\Delta\lambda(H)$ since it may contain signals associated with flux entry and flux motion within the sample. The ac susceptometer is sensitive only to an overall magnetic moment; it cannot *see* directly if vortices are present in the sample. However, if certain precautions are taken and close attention paid to the data, one can be certain that the sample did not enter the mixed state as the dc field was increased and that such results will indeed represent the intrinsic field dependence of the Meissner state penetration depth.

First, it was found by experiment that any sharp edges or corners on the sample must be removed (for example by careful polishing). Even in the measurement geometry used here, where the fields are applied in the plane of the crystal and demagnetizing effects are small, field entry at the sharp edges of an as-grown crystal can drastically affect results. In particular, removing the edges of the crystal had a dramatic effect on the nonlinear response, and Figure 5.5 shows the importance of this procedure. Measurements of the inductive response of an $YBa_2Cu_3O_{6.95}$ single crystal at 60 K are shown for fields $\pm 45°$ to the b-axis in the *ab*-plane; the data is the average sample response at each magnitude of the applied dc field. A response that differs for the two orientations (top graph) clearly breaks the symmetry of the situation (a rectangular sample with edges aligned with the orthorhombic axes) and can be attributable only to some extrinsic effect. The sharp edges of the crystal were then removed by abrasion on a 0.1 micron grit diamond polishing pad [87]; a picture of the polished crystal[3] is also shown in Figure 5.5. After polishing, the inductive response agrees for both directions (bottom graph) as it must for a rectangular orthorhombic crystal. Also note the order of magnitude reduction in signal, which was observed to be insensitive to further polishing of the edges. One should take note of the ± 0.1Å resolution[4] achieved in these measurements.

5.2.3 Sample Hysteresis: Bulk Field of First Flux Entry

Clearly, the applied dc field should never be allowed to exceed the field of first flux entry H^* of the bulk sample. Hysteresis in the sample response due to flux pinning and/or a

[3]This is crystal YCB, as named in Chapter 6.

[4]The resolution in emu is given by $\delta m = (2A\delta\lambda)H \times 10^3$, where A is the area of the crystal ($\sim 2 \times 10^{-6}$ m^2), $\delta\lambda$ is the quoted resolution for the penetration depth ($\sim 10^{-11}$ m), H is the ac field ($\sim 2.5 \times 10^{-4}/\mu_o$ A/m), and 10^3 is the conversion from SI units. This gives $\delta m \sim 8 \times 10^{-12}$ emu. To achieve this resolution a total of 80 seconds averaging time was used per field value. For comparison, the Oxford Instruments' Magnetic Properties Probe has an RMS noise base of 2×10^{-8} emu when operating at 1000 Hz with a 1 Oe drive field and using a 3 second time constant (see www.oxinst.com/ri/measure/maglabprobes.htm). To directly compare the systems, one must scale signal-to-noise with respect to frequency, drive field, and square root of averaging time.

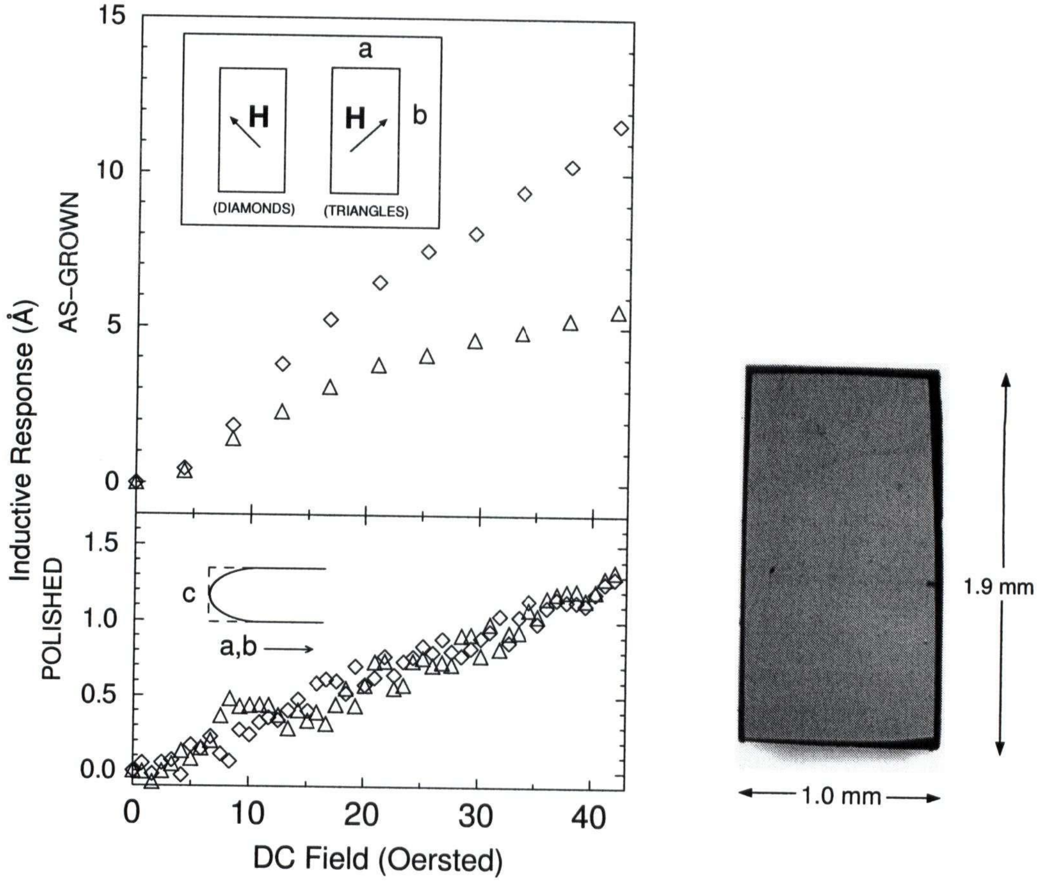

Figure 5.5: The inductive response at 60 K for H applied $\pm 45°$ to the b-axis (see inset). Top graph: results for as-grown crystal. Bottom graph: results after polishing the edges of the crystal. Also shown is the shape of an edge before and after polishing. A picture of the actual $YBa_2Cu_3O_{6.95}$ single crystal with polished edges is shown at the right.

surface barrier is a tell-tale sign that H^* has been exceeded. Even in the highest quality single crystals, this hysteresis is expected. This can be seen in Figure 5.6 where both the inductive response and the loss response of a high purity $YBa_2Cu_3O_{6.993}$ single crystal show strong hysteresis. The inductive response here still reflects the diamagnetic moment of the sample; plotted using the calibration constant of Equation 4.7, an increased signal in Angstroms corresponds to a decrease in the diamagnetic volume of the sample and can be visualized simply as an increase in some *effective* penetration depth. The loss response is associated with dissipation due to flux entry and flux motion within the sample.

The inset in Figure 5.6 shows data from the first two loops of the inductive response of the sample immediately after it had been cooled below T_c in zero field. The first points on the initial loop are indicated by the connected solid line. It is clear that the initial field response of the sample is very different here; it shows a weak monotonic increase with increasing field. However, after the applied field has exceeded $H^* \sim 35$ Oersted for the first time, the subsequent field response of the sample shows a strong decrease as the field first increases (in either direction) away from zero. This is a signature of flux being trapped in the sample due to a surface barrier; the flux having entered the sample when the applied field was in one direction does not completely exit the sample until a reverse field of sufficient magnitude is applied to drive it out.

Depending on sample geometry and the presence of a surface barrier, H^* may not be equal to the lower critical field H_{c1}. Looking again at the main graph in Figure 5.6, there is a sharp upturn in the sample response at ~ 35 Oersted, denoted as H^* the field of first flux entry. As the field is decreased from the maximum value the sample response is relatively flat until a sharp downturn at ~ 22 Oersted, denoted as H_{ex} the field at which the flux starts to exit the sample. The interpretation of this is that a surface barrier, characterized by the field $H_b = (H^* - H_{ex})/2$, prevents flux from entering (exiting) the sample at exactly the lower critical field H_{c1} as the field is increased (decreased) [88]. The value of H_b, calculated from the experimental values of H^* and H_{ex}, is roughly 7 Oersted, and looking at Figure 5.6, this agrees well with the notion that H_b should also be the reverse field required to fully drive the flux out of the sample [88]. The discussion above also implies that $H^* = H_{c1} + H_b$ and $H_{ex} = H_{c1} - H_b$, and that an experimental estimate of the in-plane lower critical field can be made using $H_{c1} = (H^* + H_{ex})/2$. For this sample then the in-plane H_{c1} at 77 K is approximately 28 Oersted, which is almost a factor of 2 smaller than what has been reported elsewhere for the slightly less oxygen

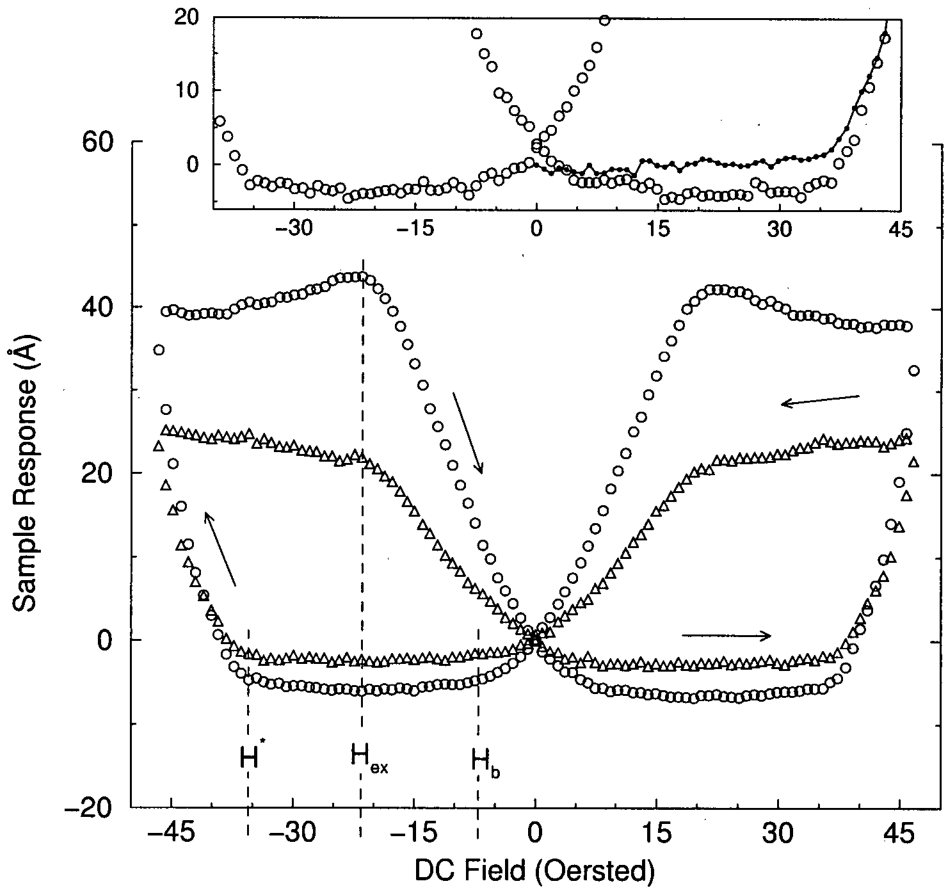

Figure 5.6: Hysteretic response of $YBa_2Cu_3O_{6.993}$ at 77 K; arrows indicate direction of field sweep. Both the inductive response (circles) and loss response (triangles) are hysteretic when the field of first flux entry H^* is exceeded. Inset: the initial hysteresis loop (solid line) of the inductive response.

doped material $YBa_2Cu_3O_{6.95}$ [41].

Because H^* may not equal H_{c1}, and because one cannot necessarily depend upon published values of the latter, it is absolutely imperative that an *in situ* determination of H^* is made for each sample and at each temperature where one hopes to measure the NLME. This process is summarized in Figure 5.7, which shows the results for the field dependent inductive response of $YBa_2Cu_3O_{6.993}$ at 40 K for several different maximum dc fields. For this sample, the area A enclosed by the hysteresis loops is roughly proportional

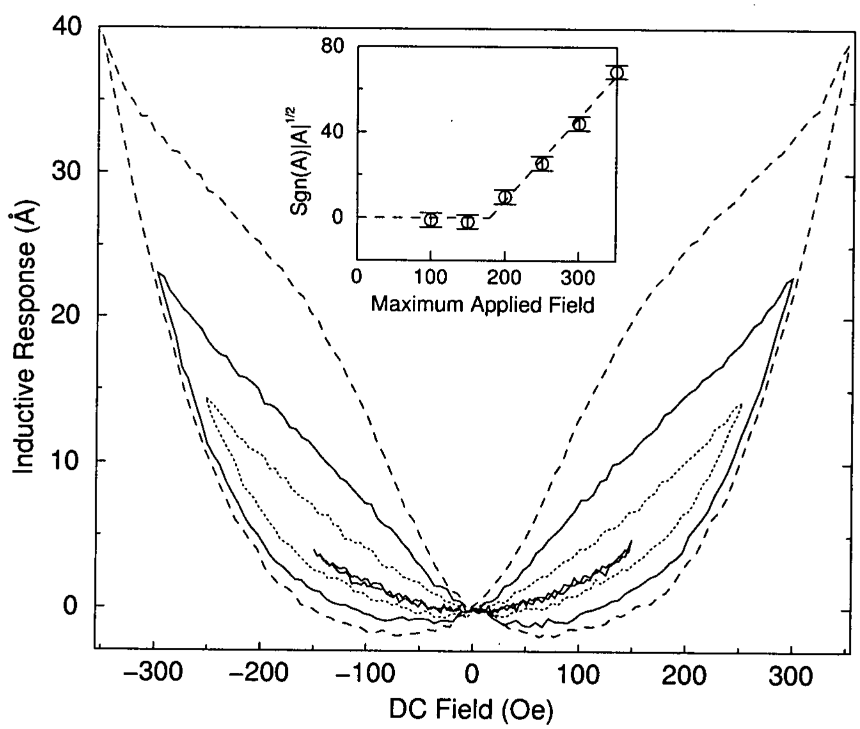

Figure 5.7: The magnetic field dependence of the inductive response of $YBa_2Cu_3O_{7-\delta}$ at 40 K. Hysteresis is present when the field of first flux entry H^* is exceeded. Inset: the square root of the area A of the hysteresis loop versus maximum applied field. The dashed lines are to guide the eye.

to H^2 at high fields. A plot of the square root of the area versus maximum applied field (inset of Figure 5.7) shows that hysteresis effects have a well defined onset, about 180 oersted at 40 K for this sample. All measurements where the maximum field is kept safely below this level show no hysteresis within the resolution of the experiment and have the same field dependence. This means the sample did remain in the Meissner state, and that the results are indeed a true measurement of $\Delta\lambda(H)$. To further corroborate this finding, it should be noted that the loss signal, which usually tracks the inductive response when the area of its hysteresis loop is finite, is zero when A is zero.

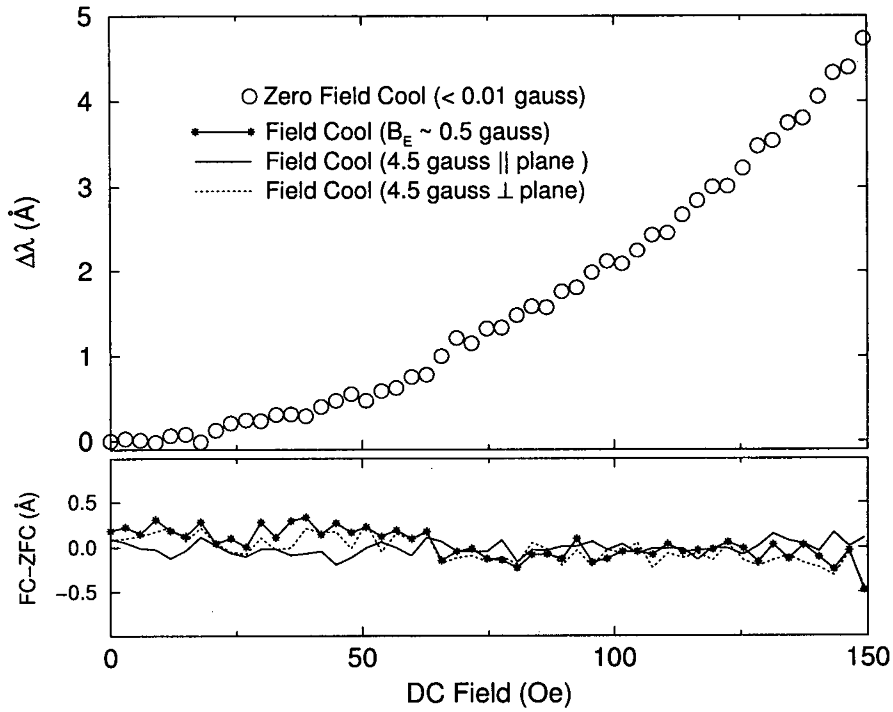

Figure 5.8: $\Delta\lambda(H)$ of $YBa_2Cu_3O_{7-\delta}$ at 4.2 K. Top Graph: results for zero field cooling (ZFC). Bottom Graph: results for various field cooled (FC) preparations plotted as FC-ZFC.

5.2.4 Cooling Sample in Small Fields

Before each run the sample is heated above T_c and cooled in zero field to limit the presence of trapped flux. To achieve *zero field*, mu-metal foil is wrapped around the dewar, which shields the earth's field, $B_E \sim 0.5$ gauss, to within 0.01 gauss (the resolution of our gaussmeter). However, because one might still question the extent to which even a very small amount of trapped flux might influence the data, repeat measurements were done with various field cooled (FC) preparations of the sample. The results for the inductive response of the sample, averaged for each absolute dc field value, are shown as $\Delta\lambda(H)$ in Figure 5.8. In addition to a zero field cooled (ZFC) measurement, the sample was measured after being field cooled in the earth's field, as well as in fields of magnitude

~ 4.5 gauss in directions both parallel and perpendicular to the plane of the crystal. It is clear from the bottom graph of Figure 5.8 that cooling in small fields does not contribute at all to the field response of the sample, which we believe has been correctly identified in the top graph as the intrinsic field dependence of the penetration depth $\Delta\lambda(H)$.

Chapter 6

Results and Discussion

Measurements of $\Delta\lambda(H)$ were made on three single crystals of $YBa_2Cu_3O_{7-\delta}$. Their characteristics are summarized in Table 6.1, which also notes the type of crucible in which the crystal was grown. Crucibles made of $BaZr0_3$ (BZO) offer higher quality crystals than ones grown in yttria-stabilized zirconia crucibles (YSZ), which tend to corrode in the crystal melt [89, 17] and lead to lower purity and poorer crystalline quality. For the experiment to have adequate resolution, it was important that the samples had large *ab*-plane dimensions; as it turned out, crystals of area significantly less than 1×1 mm^2 did not allow for meaningful results. This requirement severely limited the number of samples that were suitable for this measurement, and quite often one was forced to choose a sample with less than ideal qualities. For example, YPL was heavily twinned, and so could not be used to study the possible anisotropy in the NLME. Data from the large, detwinned samples, YCB and YCC, were used in the specific analysis and discussion of

Name	Stoichiometry	T_c (K)	Twinning	a × b × c (mm^3)	Crucible
YCB	$YBa_2Cu_3O_{6.95}$	91.8	detwinned	$1.0 \times 1.9 \times 0.056$	YSZ
YCC	$YBa_2Cu_3O_{6.993}$	88.9	detwinned	$1.9 \times 1.1 \times 0.128$	BZO
YPL	$YBa_2Cu_3O_{6.92}$	93.4	twinned	$1.1 \times 0.8 \times 0.017$	YSZ

Table 6.1: List of single crystals used for $\Delta\lambda(H)$ measurements. The table details for each crystal the stoichiometry, transition temperature, presence of twin boundaries, dimensions, and crucible type in which it was grown.

the Nonlinear Meissner Effect. Data from YPL was useful in the discussion on possible c-axis effects, and was useful as well for the discussion on the intrinsic limit of nonlinearities in thin film high-T_c devices.

6.1 Some Preliminary Experiments

As a first check of the theory, early measurements were made on conventional superconductors to see if the field dependence of λ would follow (Equation 3.13):

$$\lambda(T,H) = \lambda(T)\left\{1 + 3\beta(T)\left[\frac{H}{H_o}\right]^2\right\}$$

where the coefficient $\beta \propto e^{-\Delta/T}$ at low temperature. Some $\Delta\lambda(H)$ data for polycrystalline $Pb_{0.95}Sn_{0.05}$ is shown in Figure 6.1. A summary of these results, along with results for polycrystalline Niobium, are also shown plotted as $\ln\beta$ versus $1/T$, where β is the coefficient from a quadratic fit to the data. Measurements of $\Delta\lambda$ versus temperature for $Pb_{0.95}Sn_{0.05}$ (see Figure 1.4) show the thermally activated $e^{-\Delta/T}$ behaviour expected for an s-wave superconductor. However, it is clear from Figure 6.1, that $\Delta\lambda(H)$ measured for these samples does not disappear as $T \to 0$. At higher temperatures, it appears that the effect is thermally activated and can be fit with a reasonable choice of the energy gap[1], but this does not persist to low temperatures, and so does not agree with the prediction of Yip and Sauls [28, 30]. This may be due, in part, to the polycrystalline nature of the samples. However, measurements on single crystal niobium (type II) gave a similar result. Impurities could be playing a role here, but it is most likely that the dominant effect comes from flux entry at sharp edges and surface irregularities. Both $Pb_{0.95}Sn_{0.05}$ and Nb are very soft materials, and as a result, a satisfactory preparation of the edges and surfaces of the samples could not be achieved.

[1]For Pb, the energy gap Δ is roughly 15.5 K [25]; this should be similar for $Pb_{0.95}Sn_{0.05}$. For Nb, $\Delta \simeq 17.5$ K [25].

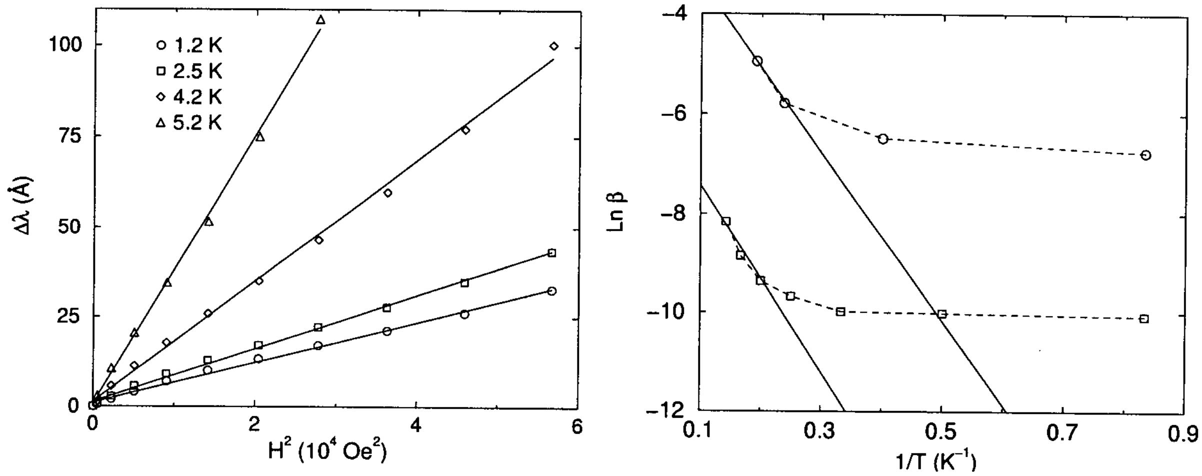

Figure 6.1: Left graph: $\Delta\lambda(H)$ for polycrystalline $Pb_{0.95}Sn_{0.05}$. Solid lines are fits to the data. Right graph: Coefficient $\beta(T)$ for polycrystalline $Pb_{0.95}Sn_{0.05}$ (circles) and Nb (squares). Solid lines are fits to data at high temperature with slopes of -17 K and -19 K, respectively; dashed lines to distinguish data points only.

A possible alternative to these superconductors could be one of the A-15 compounds, such as Nb_3Ge or V_3Si. These materials have relatively high T_c's, which is certainly an advantage if one wants to observe thermally activated behaviour. More importantly for this experiment, they are mechanically hard and brittle [90], and therefore more suitable to the polishing and other crystal preparation that needs to be done. As mentioned in Chapter 3, measurements of $\Delta\lambda(H)$ in V_3Si have been made [54], but they were far from conclusive, and the very important test of the Yip and Sauls theory on a conventional type II superconductor has yet to be been done.

The importance of removing any sharp edges on the sample was discussed in Section 5.2.2, and cannot be overstated. In that section, data was presented for YCB at 60 K (see Figure 5.5) which showed the very dramatic effect sharp edges had on field

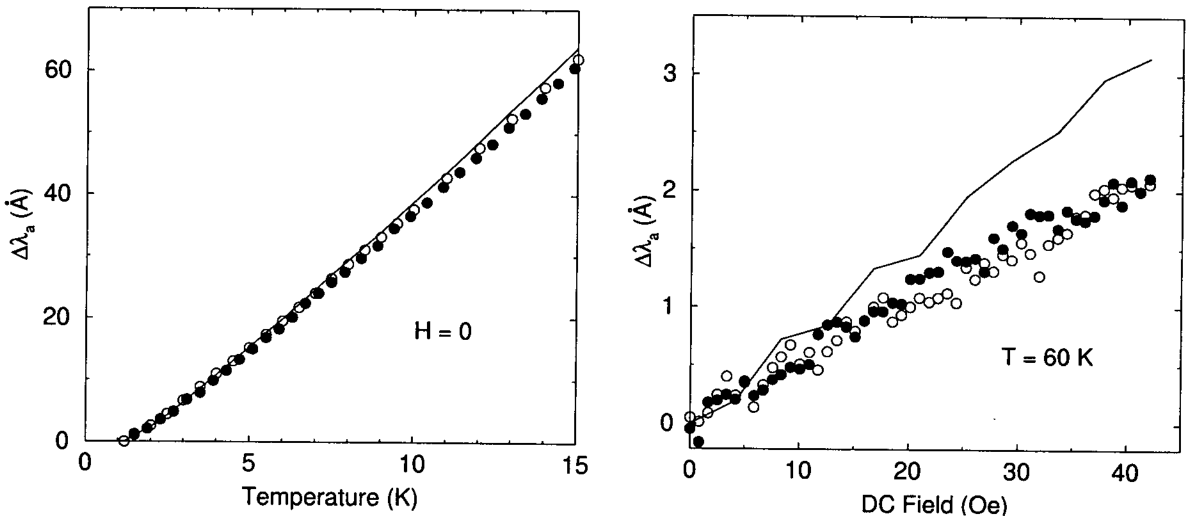

Figure 6.2: Changes in $\Delta\lambda_a(T)$ and $\Delta\lambda_a(H)$ due to polishing edges of crystal YCB. Results are shown for the crystal as it was grown (solid line), and after being polished once (open circles) and twice (filled circles).

dependent measurements made at 45° to the crystal axes; there was an order of magnitude reduction in the signal once the edges were polished off.[2] In Figure 6.2, more data related to the polishing of the crystal edges are shown for the purpose of highlighting two other important facts. First, for $\Delta\lambda(T)$, there is little change from the as-grown result, especially at low temperature, which we take as evidence that the sample was not damaged by the polishing process. Second, for $\Delta\lambda(H)$, a reduction is seen after the first polish (indicating that some edge effect did contaminate the as-grown result), but more importantly, a subsequent polish did not bring further change in $\Delta\lambda(H)$. As a result, one can be confident that sharp edges were responsible for the difference seen in the as-grown data, and furthermore a single polish to remove the sharp edges is sufficient to avoid this extrinsic signal related to flux entry.

[2]For fields along the crystal axes, the effect is not so dramatic. For example, $\Delta\lambda_a(H)$ for YCB at 60 K showed a 30% reduction after polishing the edges (see Figure 6.2).

6.2 Tests of the Nonlinear Meissner Effect

Measurements of $\Delta\lambda(H)$ from both YCB and YCC are compared with several key aspects of the NLME theory. For both samples, results show definite disagreement with prediction, and therefore the observed field dependence of λ in $YBa_2Cu_3O_{7-\delta}$ cannot be the sole consequence of the Nonlinear Meissner Effect.

6.2.1 The Evolution of $\Delta\lambda(H)$ at Low Temperature

The Yip and Sauls theory predicts that the linear field dependence of λ in a d-wave superconductor should crossover to a weaker quadratic dependence at low fields when $T \neq 0$, and furthermore, that the crossover field between these two regimes increases with increased temperature. To explore this prediction, $\Delta\lambda_a(H)$ for YCB and YCC at 1.2, 4.2 and 7.0 K has been plotted in Figure 6.3 alongside the theoretical curves for those temperatures. To produce the curves, we have used the method from Li *et al.* [33] outlined in Section 3.4.2. Considering only the local limit (for now), Equation 3.19 can be written [91] as

$$\Delta\lambda(T,H) = \frac{\lambda_o}{4}\frac{T}{\Delta_o}\sum_{l=\pm1} u^2 \left[\ln\left(e^z+1\right) + \ln\left(e^{-z}+1\right)\right] \tag{6.1}$$

where $z = u \times \sqrt{2}H\Delta_o/H_oT$, $u = |\cos\theta + l\sin\theta|$, and θ is the direction of the field with respect to an antinode.[3] The energy scale Δ_o (related to the gap maximum) is extracted from measurements of the temperature dependence of λ for each crystal by fitting Equation 6.1 with $H = 0$ to the slope of $\Delta\lambda_a(T)$ at low temperature. For example, for YCB $\mathrm{d}\Delta\lambda_a/\mathrm{d}T \sim 5$ Å/K, and using the literature value $\lambda_o = 1600$ Å [84] gives $\Delta_o = 220$ K. The characteristic field H_o is then determined by finding the best fit of

[3] It is easy to see that as $T \to 0$, Equation 6.1 reduces to the Yip and Sauls result $\Delta\lambda = \alpha\lambda_o H/H_o$, where $\alpha = (1/2\sqrt{2})\sum_{l=\pm1}|\cos\theta + l\sin\theta|^3$. In the limit $H \to 0$, Equation 6.1 reduces to the well known result $\Delta\lambda = \ln(2)\lambda_o T/\Delta_o$ for the temperature dependence of the penetration depth in a d-wave superconductor [39].

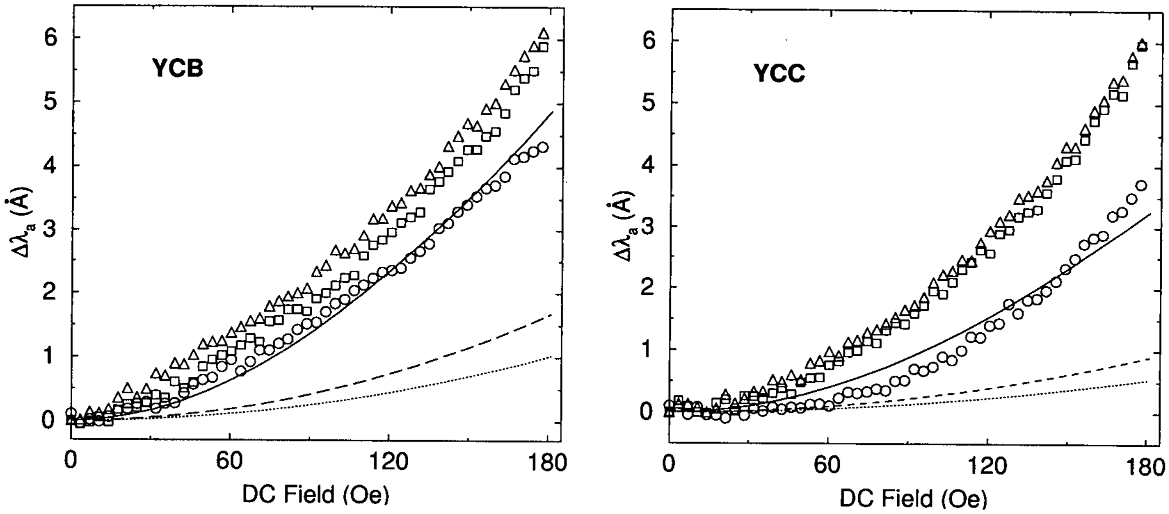

Figure 6.3: The evolution of $\Delta\lambda_a(H)$ with temperature: 1.2 K (circles), 4.2 K (squares), 7.0 K (triangles). Theoretical curves: 1.2 K (solid line), 4.2 K (dashed line), 7.0 K (dotted line).

Equation 6.1 to the $\Delta\lambda_a(H)$ data at $T = 1.2$ K. For YCB and YCC, H_o was found to be 2.0 and 2.7 T respectively. With all the parameters chosen, the theoretical curves at 4.2 and 7.0 K are then calculated to see the expected evolution of the NLME with temperature.

The values of Δ_o and H_o are close to the estimates (200 K and 2.5 T) made by Yip and Sauls [28, 30], which initially suggests that at 1.2 K these results could be the predicted NLME. However, there are clear discrepancies that can be seen in Figure 6.3. First, the data for YCC does not fit the theory very well at 1.2 K; it appears to be more quadratic in shape, a fact which will be discussed further along in Section 6.2.3. More importantly, however, data for both crystals show a small increase in $\Delta\lambda_a(H)$ with temperature,[4] which is in stark contrast with the strong suppression predicted by theory. The inclusion of nonlocal effects does not account for this difference. As discussed in Section 3.4.2,

[4]This was seen in all other measurement directions as well.

nonlocality actually leads to a greater suppression of $\Delta\lambda(H)$ with temperature, which justifies the original assumption that it could be ignored for the sake of this analysis.

6.2.2 Anisotropy at Low Temperature

The NLME also predicts a $\sqrt{2}$ anisotropy in the linear $\Delta\lambda(H)$ when the field is applied along a node as opposed to an antinode (see Equations 3.16 and 3.17). To examine this, $\Delta\lambda(H)$ was measured with the field along the a and b crystal axes, as well as $\pm 45°$ to these axes, which for a tetragonal crystal will be the nodal direction. The data is shown in Figure 6.4 along with theoretical fits. The top panels show the results for the a and b directions, while bottom panels show the 45° results (data was averaged for the two directions here). The inset in the bottom left panel gives the angular dependence of the prefactor α and is there to show that small uncertainty in sample orientation would not introduce any significant error.

The fit parameters for the $a(b)$ direction were found using the method outlined above. For YCB, these are $\Delta_o = 220(150)$ K and $H_o = 2.0(1.9)$ T, and for YCC, $\Delta_o = 230(215)$ K and $H_o = 2.7(1.8)$ T. This is important to point out, because one might naively assume that the magnitude of $\Delta\lambda(H)$ would track the value of λ_o and would therefore be smaller in the b direction, as is seen for YCB. For YCC, however, $\Delta\lambda(H)$ is larger in the b direction, and one must keep in mind that the phenomenon is also governed by an energy scale Δ_o and a characteristic field H_o. There is consistency between the two samples in as far as λ_o, Δ_o and H_o are all smaller for the b direction.

For the 45° direction, the parameter Δ_o was determined from the slope of $\Delta\lambda_{45}(T)$, while H_o was taken to be the average of the a and b values. Two curves are plotted along with the $\Delta\lambda_{45}(H)$ data in Figure 6.4. The solid line is the theoretical curve produced using the parameters for the 45° direction, but assuming that H is still along an antinode. As such, the solid curve represents the average of the a and b response, and appears to

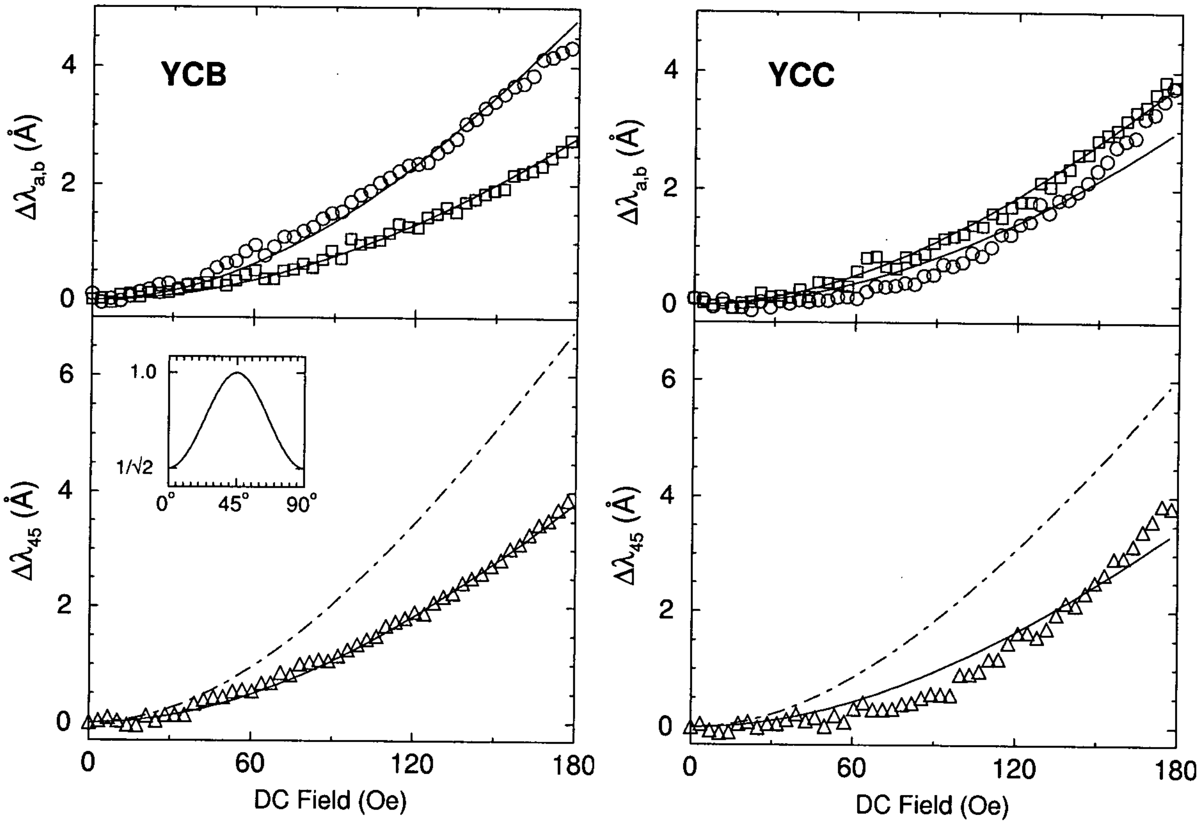

Figure 6.4: The anisotropy in $\Delta\lambda(H)$ at 1.2 K. Data: $\Delta\lambda_a$ (circles), $\Delta\lambda_b$ (squares), and $\Delta\lambda_{45}$ (triangles). Theoretical curves: along antinodes (solid lines) and along nodes (dashed lines). The inset shows how α varies with field orientation with respect to an antinode.

fit the data quite well. In contrast, the dashed line, which is the theoretical response for H along a node, suggests that there should be a much stronger effect in this direction. It appears that the predicted anisotropy is not present, and this fact was previously considered [56] to be the strongest evidence against the Yip and Sauls theory.

However, as noted in Section 3.4.3 the effects of orthorhombicity and an anisotropy in λ_o could produce a similar result [46, 47], whereby one would see a $\Delta\lambda_{45}(H)$ that looks to be the average of $\Delta\lambda_{a,b}(H)$. In an orthorhombic system, in the linear (low field) limit, λ at the 45° direction will still be the average of $\lambda_{a,b}$, but the nonlinear response need not behave with an average characteristic field.[5] The upshot of this is that in a YBCO-like system there is in general an anisotropy in the characteristic field (due to orthorhombicity and anisotropic λ_o), as well as the anisotropy in the nonlinear response (due to the NLME), and the possibility arises where these two anisotropies conspire to give an average in the nonlinear response for fields along a node. Haltermann *et al.* [46] have shown that for $YBa_2Cu_3O_{6.95}$, which has an anisotropy factor $\Lambda = \lambda_a/\lambda_b \sim 1.6$ [84], this will happen if the Fermi velocity at a node makes an angle $\phi \simeq \pi/4$ with respect to the crystal axes. They contend, therefore, that the apparent lack of the $\sqrt{2}$ anisotropy in $\Delta\lambda(H)$ is quite consistent with the NLME in YBCO. However, for a given Λ, the overall anisotropy in $\Delta\lambda(H)$ is quite sensitive to the value of ϕ (see Figure 3.7), and it remains to be seen whether this delicate balance (between orthorhombicity and the NLME) can really account for the fact that no enhancement is seen in $\Delta\lambda_{45}(H)$ for both YCB ($YBa_2Cu_3O_{6.95}$) and YCC ($YBa_2Cu_3O_{6.993}$).

In a very recent preprint, Haltermann *et al.* [47] have specifically re-analyzed the $\Delta\lambda(H)$ data of YCB (shown in Figures 3.8 and 6.4, and published in Reference [56]). Assuming an anisotropy $\Lambda \sim 1.5$, they found that the high field slope of the data could be fit in the three directions using $H_o = 0.566$ T and $\phi = \pi/4 + \pi/17$. However, this analysis cannot account for the increase that was seen in $\Delta\lambda(H)$ with increased temperature. At the moment then, one can only say that effects of orthorhombicity *may* explain the apparent lack of anisotropy in the measurements of $\Delta\lambda(H)$ in YBCO.

[5] This is why, for both samples, the value of Δ_o determined for the 45° direction was in fact the average of Δ_o in the a and b directions. This also means that the assumption above to use an average H_o in the 45° direction was tantamount to assuming the crystals to be tetragonal, which they are not.

6.2.3 Quadratic $\Delta\lambda(H)$: The Dahm and Scalapino Regime

It is clear from Figures 6.3 and 6.4 that $\Delta\lambda(H)$ for sample YCC is not well fit by a linear term that crosses over to quadratic at low fields (as is the prediction of the NLME at the low temperatures). On the other hand, the data can be quite well fit to a quadratic field dependence (of the form $\Delta\lambda = kH^2$) over the entire temperature range, 1.2 to 77 K, where data was taken. As an example, the left panel of Figure 6.5 shows $\Delta\lambda_b$ plotted versus $(H/H_{max})^2$ for a wide variety of temperatures, where H_{max} is the maximum field at which the measurements were taken. This begs the question, whether by 1.2 K the linear field dependence of the NLME has already been obscured by the thermal effects discussed in Section 3.4.1.

The NLME predicts that for a given temperature $\Delta\lambda(H)$ crosses over to a quadratic field dependence below a field $H_T \simeq (T/\Delta_o)H_o$ [30], which suggests that for $\Delta_o \sim 200$ K and $H_o \sim 2.0$ T (average values from Section 6.2.2) the cross-over at 1.2 K is $H_T \sim$ 120 Oe. This value is a significant fraction of the field range used at 1.2 K; for measurements at 4.2 K and higher, $H_T \gg H_{max}$ and theory would suggest that the signature linear $\Delta\lambda(H)$ of a $d_{x^2-y^2}$ superconductor should not be seen at all at these temperatures. Experimentally, one is restricted to fields less than H_{c1}, and cannot arbitrarily apply $H \gg H_T$ to recover $\Delta\lambda \propto |H|$. However, data can be analyzed in this high temperature range ($m\boldsymbol{v}_f \cdot \boldsymbol{v}_s \ll k_BT \ll k_BT_c$) using the work of Dahm and Scalapino [36, 37] described in Section 3.4.1. Their main prediction of an upturn in the quadratic coefficient $\beta(T)$ at low temperatures is a signature of $d_{x^2-y^2}$ superconductivity as well, and should provide an equally stringent test of the NLME.

Using Equation 3.18:

$$\Delta\lambda(T, H) = \lambda(T)\frac{\beta}{2}\left(\frac{H}{H_o}\right)^2$$

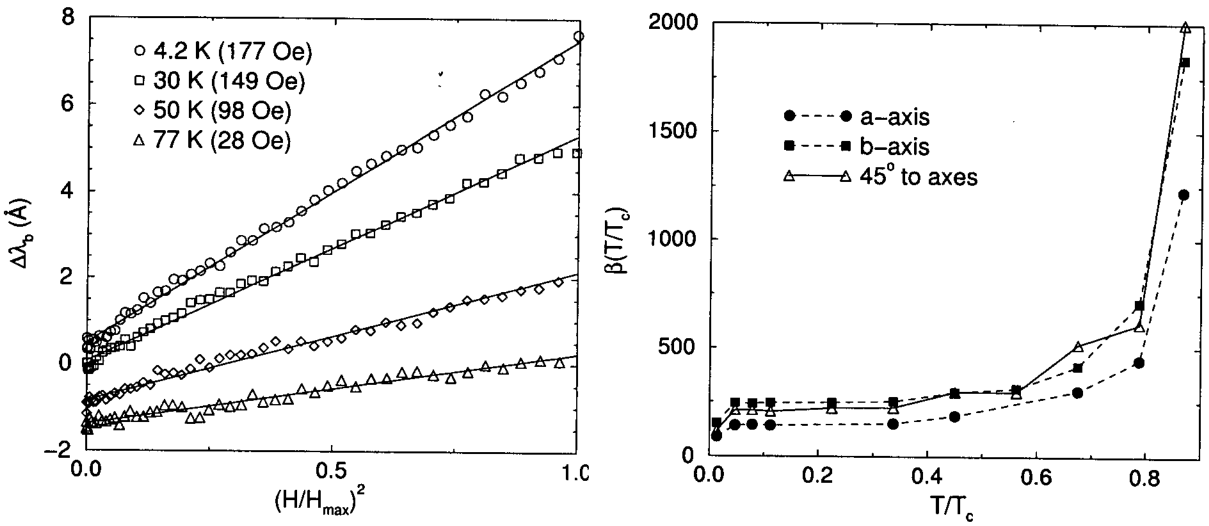

Figure 6.5: The quadratic field dependence of $\Delta\lambda(H)$ in YCC. Left panel: $\Delta\lambda_b$ versus $(H/H_{max})^2$ for several temperatures (H_{max} shown in parenthesis); data offset for clarity. Right panel: coefficient $\beta(T/T_c)$ from 1.2 to 77 K in the directions shown on plot; lines are to distinguish the data points only.

the coefficient $\beta(T)$ can be determined from the fit parameter k via the relation:

$$\beta(T) = \frac{2H_o^2}{\lambda(T)}k \tag{6.2}$$

where the characteristic field H_o is taken to be 2.5 T [30]. The values of β are plotted versus T/T_c in the right panel of Figure 6.5 for the a, b, and 45° direction, and were calculated using constant values of 1600, 1000, and 1300 Å for λ in the three directions respectively. The decision to ignore the temperature dependence in H_o and λ is not critical in this analysis, because at low temperatures, where one is looking for an upturn in $\beta(T)$, these parameters vary little and negligible error will be introduced by this assumption.

It is obvious from Figure 6.5 that there is no upturn in $\beta(T)$ as $T \to 0$. There is also a huge discrepancy in the magnitude of the coefficient; the values for YCC are two orders of magnitude larger than the prediction [36, 37], which is easily noted by a visual comparison with Figure 3.5. This, again, suggests that the Yip and Sauls mechanism is not the origin of the field dependence of the penetration depth in YBCO.

6.3 Alternative Origins for a Field Dependent Penetration Depth

6.3.1 Field Induced Suppression of the Energy Gap

Very recently, J.R. Cooper [92] has developed an empirical model to try to explain the published $\Delta\lambda(H)$ data for high-T_c superconductors. His model differs from the Yip and Sauls theory in that the energy shift $m\boldsymbol{v}_f \cdot \boldsymbol{v}_s$, due to the superfluid velocity v_s, actually destroys the superconductivity around the nodes of the $d_{x^2-y^2}$ gap (see Figure 6.6). In the original NLME theory, the low lying quasiparticles states around the nodes are only considered to be shifted in energy, but otherwise remain unaltered (see Figure 3.1). The premise of Cooper's idea is straightforward, and well understood from conventional superconductivity [11, p.125]: a critical (or *depairing*) velocity occurs when the superfluid velocity $v_s = \Delta_o/mv_f$, and at this point the energy gap goes to zero and superconductivity is destroyed. Generalizing this to a $d_{x^2-y^2}$ gap, one expects the energy gap to be pushed to zero when the condition $m\boldsymbol{v}_f \cdot \boldsymbol{v}_s \geq \Delta(k)$ is satisfied. This will first happen around the nodes, as shown in Figure 6.6.

The gist of Cooper's model may be expressed as follows. For a $d_{x^2-y^2}$ gap, $\Delta(k) = \Delta_o\,|\cos 2\theta|$ varies linearly with angle near a node. One expects, therefore, that the gap will be suppressed over a small angle $\delta\theta \propto mv_fv_s/\Delta_o$ about the node (see Figure 6.6). Furthermore, the linear density of states near a node implies that the loss in superfluid density n_s due to the suppressed gap would be proportional to $\delta\theta$. For small perturbations $\delta n_s$is also proportional to $\delta\lambda$. Therefore, at small fields $\delta\lambda \propto \delta\theta \propto v_s$, and again one arrives at a linear field dependence in the penetration depth, although by a different mechanism than that of the Yip and Sauls theory.

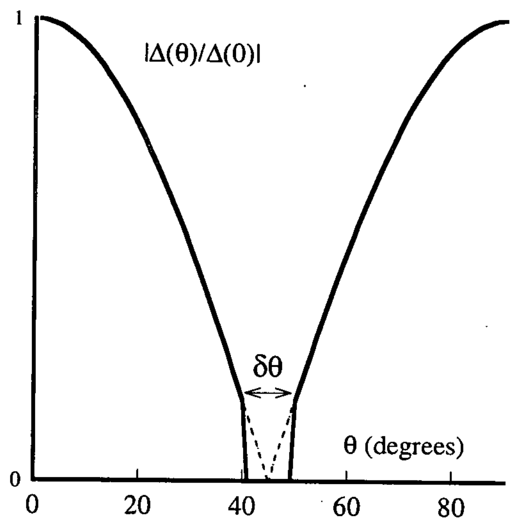

Figure 6.6: Field induced suppression of the energy gap (from Cooper [92]). In zero field (dashed line), the $d_{x^2-y^2}$ gap has a node at 45°; in finite field (solid line), the gap is zero around the node for some angle $\delta\theta$ proportional to the field.

The form given by Cooper for the field dependence of λ (with the field along an antinode) is

$$\Delta\lambda(H) = \frac{\alpha\lambda(T)}{n_s(T)} \frac{|H|}{H_c(T)} \tag{6.3}$$

where $H_c(T)$ is the thermodynamic critical field and α is a constant ~ 0.2. The same anisotropy exists here as in the NLME (ignoring orthorhombicity); for fields applied along a node, there should be a $\sqrt{2}$ enhancement in $\Delta\lambda(H)$. However, the results of the two theories differ greatly in the limit $m\boldsymbol{v}_f \cdot \boldsymbol{v}_s \ll k_B T \ll k_B T_c$; in this regime, the NLME crosses over to a weak quadratic $\Delta\lambda(H)$, while the linear field dependence of Equation 6.3 remains for this model. To account for impurity scattering and other effects that occur at zero field, it was also argued [92] that the linear field dependence $|H|$ in Equation 6.3 should be replaced by the empirical expression $\sqrt{H^2 + H_*^2} - H_*$, where H_* is a measure of the other pair-breaking processes and serves to cut off the linear dependence at low fields. The final form of $\Delta\lambda(H)$, to which fits of the data can be made, is

$$\Delta\lambda(H) = \frac{\alpha\lambda(T)}{n_s(T)H_c(T)}\left[\sqrt{H^2+H_*^2} - H_*\right] \tag{6.4}$$

Data for the sample YCB have been fit to Cooper's model over a wide temperature range. The results are shown in Figure 6.7. The main graph shows data at 1.2 and 10 K along with their best fits to the theory; for the sake of clarity, the remaining data at other temperatures was not displayed. A typical value of $H_* = 55 \pm 10$ Oe was found to fit the low temperature data quite well, and reflects the good quality of the crystal [92]. The values of the temperature dependent coefficient C_T from the data fitting are shown in the top graph in Figure 6.7, along with a theoretical curve $C_T = \alpha\lambda(T)/n_s(T)H_c(T)$ using a reasonable value of $H_c(0) = 2.0$ T for the critical field. This value gave the most suitable fit of C_T with theory, and only reconfirms what was found in Section 6.2.1, that for YCB the characteristic field (for a linear $\Delta\lambda(H)$) is of order two Tesla. This *agreement* of the magnitude of C_T with the theory is not to be taken as confirmation that the model is correct. The most significant fact here is that Cooper's model appears to have a much better feel for the temperature dependence of $\Delta\lambda(H)$ than does the NLME.

A similar analysis was also done with the YCC data. The values of H_* found here were much larger than for YCB; typically, a few hundred Oersted at the lower temperatures. It is clear from Equation 6.4 that H_* needs to be much larger than the maximum applied field to recover the quadratic $\Delta\lambda(H)$ seen in YCC. This sample is of very high purity, and X-ray diffraction measurements showed it to be of exceptional crystalline quality, two facts which seem incompatible with a large H_*. However, a routine etching procedure[6] to prepare the sample surface revealed a higher than average density of etch pits. These pits are associated with spiral defects, which are more common in thick crystals like YCC, and it is possible that this is the source of scattering reflected in the large values of H_*.

[6]YBCO samples are commonly etched in a 0.5% Br/ethanol solution, prior to measurement, to remove flux stains on their surface that are remnants of the crystal growth.

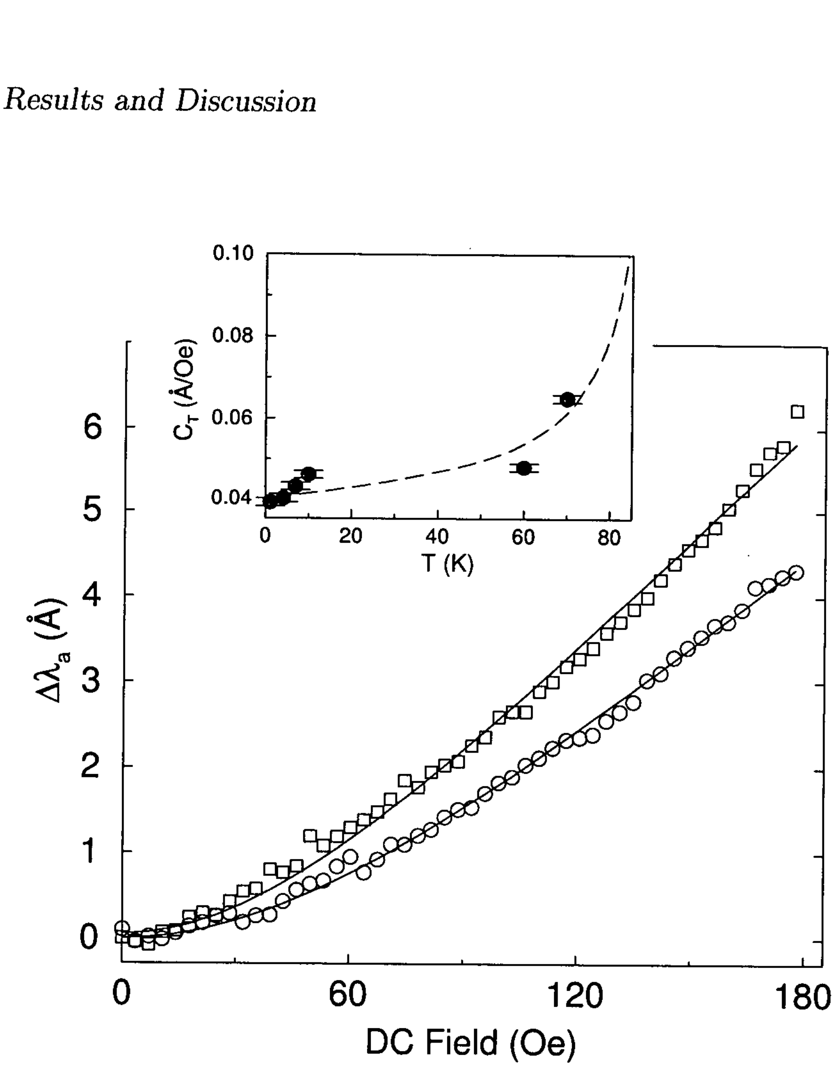

Figure 6.7: Fits of $\Delta\lambda_a(H)$ for YCB to Cooper's model. Main graph: data at 1.2 K (circles) and 10 K (squares) with theoretical fits. Top graph: values of coefficient C_T with fit to theory.

However, one must keep in mind that the effects of scattering (the difference between Equations 6.3 and 6.4) were added to this theory *by hand*, and one must be careful not to read too much into these results at the moment. To re-iterate, the most important result here is that Cooper's model, in its present form, can at least account for the evolution of $\Delta\lambda(H)$ with temperature.

6.3.2 c-axis Contribution to $\Delta\lambda(H)$

The simple slab approximation (see Appendix B) used to model platelet shaped crystals in this thesis ignores the penetration depth of the return currents flowing along the edges of the sample parallel to its thickness. For YBCO platelets, this direction is along the c-axis, and the contribution of these currents to the measured $\Delta\lambda(T, H)$ is roughly $t/w \times \Delta\lambda_c(T, H)$. The ratio of sample thickness to width, t/w, tends to be quite small for YBCO, usually much less than 0.1. On the other hand, $\Delta\lambda_c(T, H)$ may be quite large. It is very possible than that a c-axis contribution to our measurements of the field dependent penetration depth could be obscuring the NLME.

To see if this idea is justified, data for $\Delta\lambda(H)$ has been plotted in Figures 6.8 and 6.9 for all three samples, each of which has a different thickness (see Table 6). The data is shown in three panels (from left to right) to display the evolution of the $\Delta\lambda(H)$ from the thinnest sample (YPL) to the thickest (YCC), with the thickness of each sample given in microns. It is clear from just a quick glance at the data that YPL exhibits a significantly lower signal[7] at both low temperature (Figure 6.8) and high temperature (Figures 6.9). Comparison between the YCB and YCC measurements cannot be done so hastily. The data shown for these two crystals in Figure 6.8 is for the a-direction, and here the contribution from the c-axis goes as t/a. YCC is roughly twice as thick as YCB, and about twice as long in the a-direction, giving the same ratio t/a for both samples. As a result, one expects the same contribution from $\Delta\lambda_c(H)$, and assuming $\Delta\lambda_a(H)$ is the same for both crystals, there should be no difference in the overall $\Delta\lambda(H)$. This is the result seen in the measurements. The data shown in Figure 6.9 is for the b-direction, and YCC being only half as long in this direction should have a c-axis contribution here that is four times as large as for YCB. This is consistent with the data in as far as YCC

[7]The resolution is less for YPL because of its smaller surface area in the ab-plane. It is a twinned sample, so specific comparisons with the other samples in the a and b-directions will not be made.

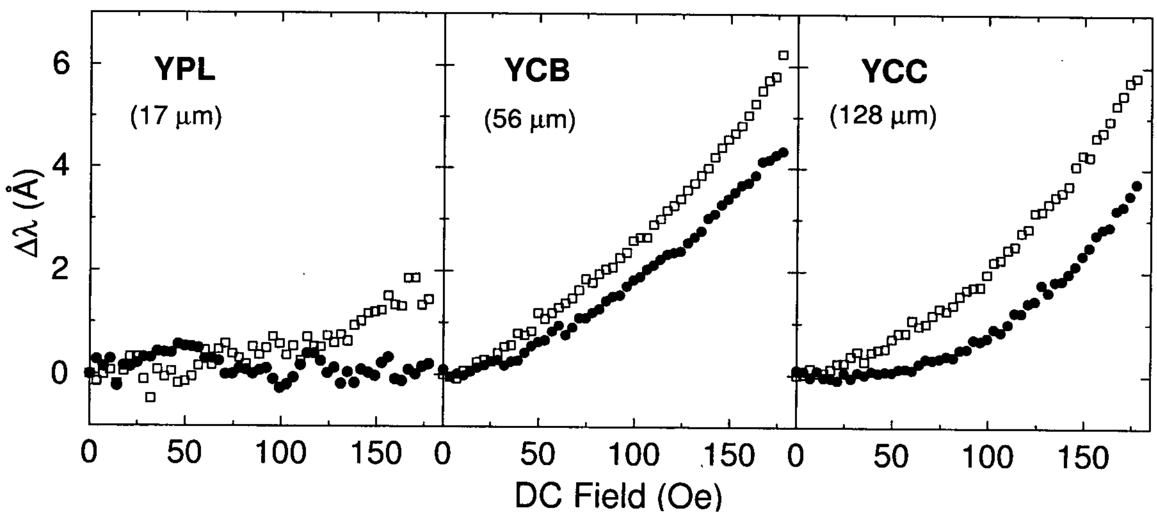

Figure 6.8: Low temperature comparison of $\Delta\lambda(H)$ between all samples: 1.2 K (circles) and 10 K (squares). Data for YCB and YCC is for the a-direction.

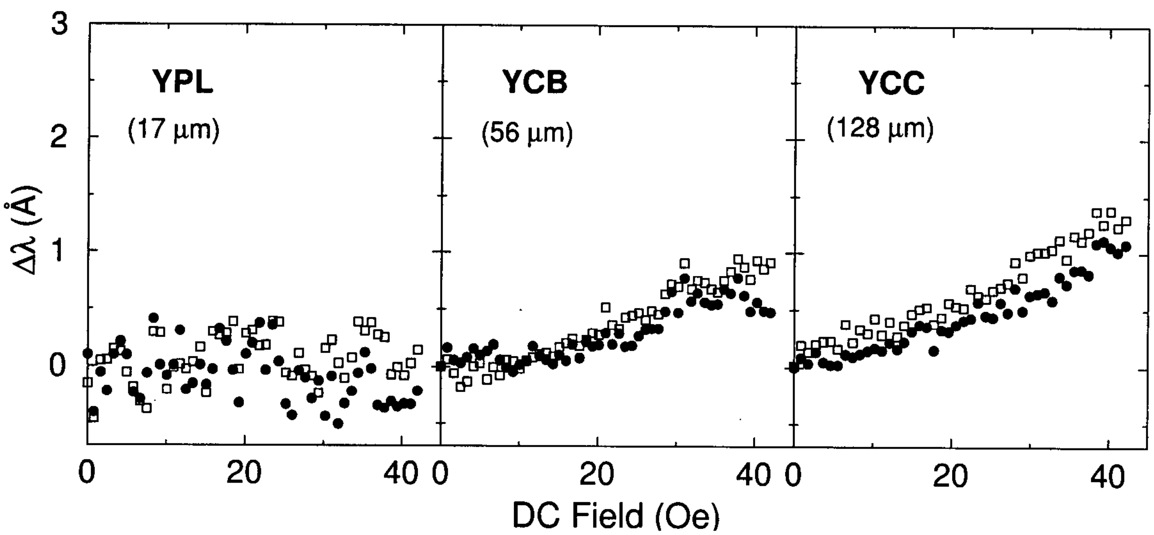

Figure 6.9: High temperature comparison of $\Delta\lambda(H)$ between all samples: 60 K (filled circles) and 70 K (open squares). Data for YCB and YCC is for the b-direction.

shows a larger overall $\Delta\lambda(H)$ in the b-direction than does YCB. This is also seen in the low temperature data (for example, the 1.2 K data shown in Figure 6.4).

So, there does appear to be reasonable experimental evidence to support the notion of a c-axis contribution to the measurements of $\Delta\lambda(H)$. How might this affect the analysis of the NLME in Section 6.2? At present, there is no theory for nonlinear Meissner screening in the c-direction, so there is no straightforward answer. It can only be said that $\Delta\lambda_c(H)$, if present, will result in an apparent NLME that is too large. At 1.2 K, $\Delta\lambda(H)$ does agree quantitatively with the Yip and Sauls theory. However, the strongest evidence against this theory at the moment is that it predicts $\Delta\lambda(H)$ to weaken with temperature, quite contrary to experiment. It was shown in Figure 2.2 that the temperature dependence of the c-axis penetration depth remained quite flat at low temperatures, before increasing at a rate much greater than the $\Delta\lambda_{a,b}(T)$, and one must wonder if something similar might not be happening in the field dependence as well. This scenario is depicted in Figure 6.10 for the Dahm and Scalapino regime, where the NLME predicts a quadratic field dependence that falls off as $1/T$. To give qualitative agreement with the experimental results in Figure 6.5, the nonlinear c-axis response must rise sharply (as the NLME decreases) and then taper off. Of course, this is completely speculative, and such a perfect interplay seems quite unlikely. Still, measurements to extract $\Delta\lambda_c(H)$ should be possible (by cleaving the sample into several pieces to multiply up the c-axis contribution, as described in Reference [26]), and would go a very long way in sorting out the $\Delta\lambda(H)$ measurements made in this thesis.

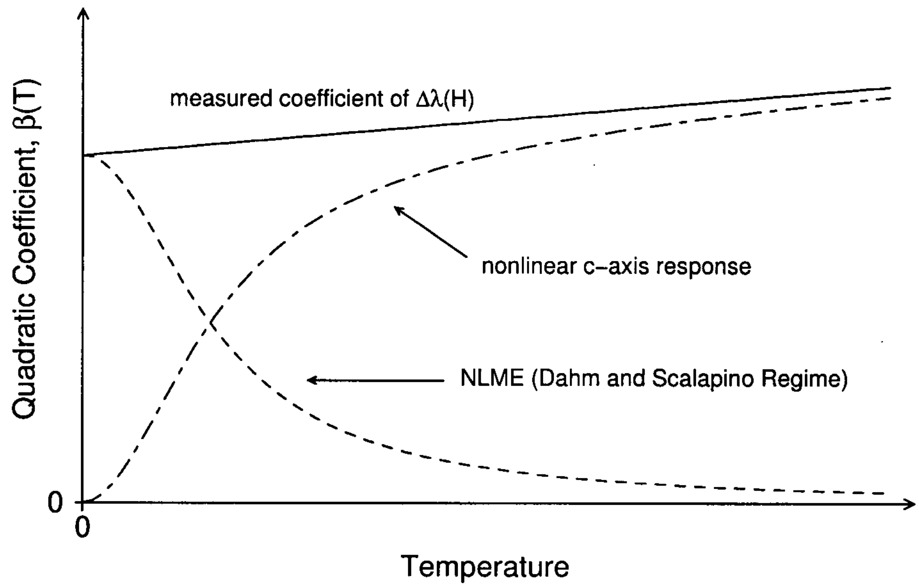

Figure 6.10: Hypothesized scenario of c-axis contributions to $\Delta\lambda(H)$: the NLME is obscurred by $\Delta\lambda_c(H)$.

6.4 The Intrinsic Limit of Intermodulation and Harmonic Generation in high-T_c Devices

As mentioned in Section 3.5.2, there is a significant research effort in the area of nonlinear electrodynamics in high-T_c thin films. The great majority of this work is concerned with the practical consequences of nonlinearities in electrical devices, such as microwave filters, that can be made from these thin films. Nonlinearities can give rise to unwanted effects due to intermodulation or harmonic generation. For example, in a filter circuit, intermodulation between different frequencies within the band width of the filter can produce spurious signals that are also inside the pass band. From this point of view, one would like to suppress the nonlinear behaviour in the thin films, which at some point is ultimately limited by the intrinsic behaviour of the thin film material itself. At present, it appears that extrinsic effects, such as vortices in weak links, are the origin of the nonlinearity (see Section 3.5.2). Presumably, with improved techniques for film growth and processing, these defects will be avoidable and thin films could eventually reach single crystal quality. In this regard, the measurements of $\Delta\lambda(H)$ in this thesis also represent an important initial study on the intrinsic limit of intermodulation and harmonic generation in YBCO thin film devices.

Booth *et al.* [67] studied the geometry dependence of nonlinear effects in micowave transmission lines they fabricated from YBCO thin films. These devices were found to exhibit third harmonic power generation that scaled with geometry and could therefore be characterized by a single geometry-independent parameter J_o. Their analysis was based on the work of Dahm and Scalapino [36], which considers the origin of the 3:1 behaviour[8] to be a nonlinear penetration depth of the form

$$\Delta\lambda(T,J) = \frac{\lambda(T)}{2}\left(\frac{J}{J_o(T)}\right)^2 \tag{6.5}$$

where J is the supercurrent density in the film. Assuming no particular mechanism for the J dependent penetration depth, the parameter J_o is just the nonlinear scaling current density and depends only on the thin film material. Booth *et al.* [67] found an average value of $J_o = 3.0 \times 10^7$ A/cm^2 for their YBCO thin films at 77 K.

From Ampere's Law, the current density in a superconductor is $J = H/\lambda$, so Equation 6.5 can be written in terms of H as

$$\Delta\lambda(T,H) = \frac{\lambda(T)}{2}\left(\frac{H}{H_o(T)}\right)^2 \tag{6.6}$$

with $H_o(T) = \lambda(T)J_o$. A quadratic field dependence was seen in our measurements of $\Delta\lambda(H)$, especially in the sample YCC. Fitting our data to Equation 6.6 allows for a direct comparison with the results for thin films. Using a reasonable value of $\lambda(77\text{ K}) = 2500$ Å,

[8] See Appendix B for the definition of 3:1 and 2:1 behaviour.

data for YCC and YCB give an average $H_o(77\text{ K}) = 0.09$ T or $J_o = 2.9 \times 10^7$ A/cm^2. This seems to be surprising; J_o for the crystals is slightly less than the 3.0×10^7 A/cm^2 seen in the films. However, we know that the crystals have a much higher crystallinity and much weaker pinning [24], so the fact that the nonlinear effects are comparable to thin films simply indicates that effects other than crystallinity come into play, possibly the c-axis. If the same analysis is applied to YPL, where $\Delta\lambda(H)$ at high temperatures could not be measured above the resolution of 0.3 Å (see Figure 6.9), one arrives at a conservative value of $H_o(77\text{ K}) = 0.18$ T or $J_o = 5.7 \times 10^7$ A/cm^2. This is a factor of two larger than what was seen in the films, which means that nonlinear effects in devices will be suppressed by a factor of four if YBCO films can be made to the same quality as single crystals.

Chapter 7

Conclusion

Measurements of the nonlinear Meissner state electrodynamics provide a good testing ground for present ideas about high temperature superconductivity; in particular, there exist very distinct predictions for the magnetic field dependence of the penetration depth in a d-wave superconductor. These nonlinearities, however, cannot not be induced to arbitrarily large magnitude, because one is cutoff by the vortex state which occurs at relatively low fields in these materials. As a result, such measurements require an instrument that is capable of resolving very small changes in the sample's magnetic moment. In this thesis, a high precision ac susceptometer was developed that is capable of measuring the change in the penetration depth of a typical sized $YBa_2Cu_3O_{7-\delta}$ single crystal to within a few tenths of an Angstrom. Measurements can also be made as a function of temperature with a similar resolution, which allows for a useful characterization of the sample in the linear limit.

It is critical that the sample remain in the Meissner state during these measurements for there to be any meaningful comparison of the results with theory. We have identified several keys steps that must be taken to ensure that this happens. First, the sharp edges of the sample must be polished round. Even in geometries where the demagnetization factor is small, the field at a sharp edge on a sample can become much larger than the applied field and flux may prematurely enter the sample here. Second, the bulk field of first flux entry H^* should be identified for each sample at each measurement temperature; this allows one to have confidence that subsequent field dependent measurements were done completely in the Meissner state. We have shown that this can be done by monitoring the hysteresis of both the inductive and loss response of the sample as a function of the maximum applied field. Due to pinning and a surface barrier, the hysteresis loops show a finite area if flux enters the sample. The onset of this behaviour, at H^*, is quite distinct, and can therefore be avoided once it has been identified. Other groups have not kept such stringent control over these concerns, and as a result the measurements presented in this thesis represent, in our opinion, the most convincingly intrinsic data on the field dependence of the penetration depth in $YBa_2Cu_3O_{7-\delta}$.

Measurements of $\Delta\lambda(H)$ were made on three high quality samples of single crystal $YBa_2Cu_3O_{7-\delta}$. Results for the two detwinned crystals, YCB and YCC, were used for direct comparison with the theory of the Nonlinear Meissner Effect. The temperature dependence of $\Delta\lambda(H)$ and its anisotropy with respect to field orientation in the *ab*-plane both disagree with the basic theory of Yip and Sauls. The anisotropy *can* be reconciled within the greater context of the NLME if one includes the effects of orthorhombicity. However, the temperature dependence remains in stark contrast with all aspects of the theory. Limiting the discussion to the low temperature data (where the signatures of the NLME should be most pronounced), $\Delta\lambda(H)$ is seen to increase slightly with temperature. If this data is interpreted in the low temperature limit of the NLME, where $kT \ll m\boldsymbol{v}_f \cdot \boldsymbol{v}_s \ll k_B T_c$, it disagrees with the prediction of a strong suppression in the linear field dependence and a cross-over to a weak quadratic dependence as temperature is increased. On the other hand, if the data is interpreted in the hight temperature limit, $m\boldsymbol{v}_f \cdot \boldsymbol{v}_s \ll kT \ll k_B T_c$, then the data fails to show a quadratic field dependence that increases with decreasing temperature. Furthermore, the size of the measured effect is roughly two orders of magnitude larger than what theory predicts in this regime. Overall, this has led us to conclude that the mechanism suggested by Yip and Sauls in the theory of the Nonlinear Meissner Effect cannot be sole origin of the field dependent penetration depth measured here in $YBa_2Cu_3O_{7-\delta}$.

A possible explanation for the temperature dependence seen in $\Delta\lambda(H)$ is that the quasi-particle states are not simply shifted in energy, but rather that the energy shift destroys the superconductivity around the nodes in the gap. This field induced suppression of the gap predicts a linear field dependence in λ that increases in temperature. The agreement with the existing data is not that good in several regards, but the theory does predict the direction of the temperature dependence correctly. However, as for the standard NLME theory, one cannot consider this theory to be the sole explanation for our measurements of $\Delta\lambda(H)$.

We have also shown that there exists the distinct possibility of a c-axis contribution to our data. Differences between the magnitude of $\Delta\lambda(H)$ in all three crystals is qualitatively consistent with the presence of a measurable $\Delta\lambda_c(H)$. Therefore, the possibility exists that this signal is obscuring the observation of the NLME in our measurements. We suggest that further studies are made whereby $\Delta\lambda_c(H)$ is determined directly by measuring $\Delta\lambda(H)$ before and after cleaving the sample.

Bibliography

[1] H. Kamerlingh Onnes, Leiden Comm. **120b, 122b, 124c** (1911).

[2] W. Meissner and R. Ochsenfeld, Naturwissenschaften **21**, 787 (1933).

[3] F. London and H. London, Proceedings of the Royal Society (London) **A149**, 71 (1935).

[4] J. Bardeen, L.N. Cooper and J.R. Schrieffer, Physical Review **108**, 1175 (1957).

[5] B.D. Josephson, Physics Letters **1**, 251 (1962).

[6] I. Giaever, Physical Review Letters **5**, 147, 464 (1960).

[7] J.G. Bednorz and K.A. Müller, Zeitschrift für Physik **B64**, 189 (1986).

[8] Charles P. Poole, Jr., *Handbook of Superconductivity* (Academic Press, San Diego, 2000).

[9] A.B. Pippard, Proceedings of the Royal Society (London) **A216**, 547 (1953).

[10] V.L. Ginzburg and L.D. Landau, Zhurnal Eksperimental'noi i Teoreticheskoi Fiziki **20**, 1064 (1950).

[11] Michael Tinkham, *Introduction to Superconductivity*, 2nd edition (McGraw-Hill International Editions, Singapore, 1996).

[12] L.N. Cooper, Physical Review **104**, 1189 (1956).

[13] E. Maxwell, Physical Review **78**, 477 (1950); C. Reynolds, B. Serin, W.H. Wright, and L.B. Nesbitt, Physical Review **78**, 487 (1950).

[14] T. Timusk and B. Statt, Reports of Progress in Physics **62**, 61 (1999).

[15] J.E. Crow and N.-P. Ong, in *High Temperature Superconductivity*, ed. J.W. Lynn (Springer-Verlag, New York, 1990).

[16] P. Schleger, W.N. Hardy and B.X. Yang, Physica C **176**, 261 (1991).

[17] Ruixing Liang, D.A. Bonn and W.N. Hardy, Physica C **304**, 105 (1998).

[18] D.M. Ginsberg, in *Physical Properties of High Temperature Superconductors, Vol. I*, ed. D.M. Ginsberg (World Scientific, Singapore, 1989) pp. 14-15.

[19] D.A. Wollman, D.J. van Harlingen, W.C. Lee, D.M. Ginsberg, and A.J. Leggett, Physical Review Letters **71**, 2134 (1993);D.A. Wollman, D.J. van Harlingen, J. Giapintzakis and D.M. Ginsberg, Physical Review Letters **74**, 797 (1995).

[20] J.R. Kirtley, C.C. Tsuei, J.Z. Sun, C.C. Chi, Lock See Yu-Jahnes, A. Gupta, M. Rupp, and M.B. Ketchen, Nature **373**, 225 (1995).

[21] C.C. Tsuei and J.R. Kirtley, Review of Modern Physics **72**, 969 (2000).

[22] W. N. Hardy, D. A. Bonn, D. C. Morgan, Ruixing Liang, and Kuan Zhang, Physical Review Letters **70**, 3999 (1993).

[23] D.A. Bonn, S. Kamal, Kuan Zhang, R. Liang, D.J. Baar, E. Klein and W.N. Hardy, Physical Review B **50**, 4051 (1994).

[24] D.A. Bonn and W.N. Hardy, in *Physical Properties of High Temperature Superconductors, Vol. V*, ed. D.M. Ginsberg (World Scientific, Singapore, 1996).

[25] Neil W. Ashcroft and N. David Mermin, *Solid State Physics* (Saunders College Publishing, Orlando, 1976).

[26] A. Hosseini, S. Kamal, D.A. Bonn, R. Liang and W.N. Hardy, Physical Review Letters **81**, 1298 (1998)

[27] A. Hosseini, R. Harris, Saeid Kamal, P. Dosanjh, J. Preston, Ruixing Liang, W. N. Hardy and D. A. Bonn, Physical Review B **60**, 1349 (1999).

[28] S. K. Yip and J. A. Sauls, Physical Review Letters **69**, 2264 (1992).

[29] Z.-X. Shen, D.S. Dessau, B.O. Wells, D.M. King, W.E. Spicer, A.J. Arko, D. Marshall, L.W. Lombardo, A. Kapitulnik, P. Dickinson, S. Doniach, J. Dicarlo, A.G. Loeser, and C.H. Park, Physical Review Letters **70**, 1553 (1993).

[30] D. Xu, S. K. Yip and J. A. Sauls, Physical Review B **51**, 16 233 (1995).

[31] Fritz London, *Superfluids, Volume 1*, 2nd revised edition (Dover Publications, New York, 1961).

[32] John Bardeen, Physical Review Letters **1**, 399 (1958).

[33] M.-R. Li, P.J. Hirschfeld, and P. Wölfle, Physical Review Letters **81**, 5640 (1998).

[34] Branko P. Stojković and Oriol T. Valls, Physical Review B **51**, 6049 (1995).

[35] Igor Žutić and Oriol T. Valls, Physical Review B **56**, 11 279 (1997).

[36] T. Dahm and D.J. Scalapino, Journal of Applied Physics **81**, 2002 (1997); Applied Physics Letters **69**, 4248 (1996).

[37] T. Dahm and D.J. Scalapino, Physical Review B **60**, 13 125 (1999).

[38] Ioan Kosztin and Anthony J. Leggett, Physical Review Letters **79**, 135 (1997).

[39] Peter J. Hirschfeld and Nigel Goldenfeld, Physical Review B **48**, 4219 (1993).

[40] Mei-Rong Li, P.J. Hirschfeld, and P. Wölfle, Physical Review B **61**, 648 (2000).

[41] Ruixing Liang, P. Dosanjh, D.A. Bonn, W.N. Hardy and A.J. Berlinsky, Physical Review B **50**, 4212 (1994).

[42] James F. Annett, Nigel Goldenfeld and Anthony J. Leggett in *Physical Properties of High Temperature Superconductors, Vol. V*, ed. D.M. Ginsberg (World Scientific, Singapore, 1996).

[43] Igor Žutić and Oriol T. Valls, Physical Review B **54**, 15 500 (1996).

[44] Igor Žutić and Oriol T. Valls, Physical Review B **58**, 8738 (1998).

[45] Klaus Halterman and Oriol T. Valls, Physical Review B **62**, 5904 (2000).

[46] Klaus Halterman, Oriol T. Valls and Igor Žutić, *preprint* cond-mat/0007510 (2000). To appear in Physical Review B **63** (2001).

[47] Klaus Halterman, Oriol T. Valls and Igor Žutić, *preprint* cond-mat/0011021 (2000).

[48] A.B. Pippard, Proceedings of the Royal Society (London) **A203**, 210 (1950).

[49] M. Spiewak, Physical Review Letters **1**, 136 (1958).

[50] M.P. Garfunkel, Physical Review **173**, 516 (1968).

[51] S. Sridhar, Dong-Ho Wu, and W. Kennedy, Physical Review Letters **63**, 1873 (1989).

[52] A. Maeda, Y. Iino, T. Hanaguri, N. Motohira, K. Kishio and T. Fukase, Physical Review Letters **74**, 1202 (1995). A. Maeda, T. Hanaguri, Y. Iino, S. Masuoka, Y. Kokata, J. Shimoyama, K. Kisio, H. Asaoka, Y. Matsushita, M. Hasegawa and H. Takei, Journal of the Physical Society of Japan **65**, 3638 (1996).

[53] A. Maeda, H. Yasuda and T. Hanaguri, Journal of the Physical Society of Japan **68**, 594 (1999).

[54] T. Hanaguri, Y. Iino, A. Maeda and T. Fukase, Physica C **246**, 223 (1995).

[55] A. Carrington, R.W. Giannetta, J.T. Kim, and J. Giapintzakis, Physical Review B **59**, R14 173 (1999).

[56] C.P. Bidinosti, W.N. Hardy, D.A. Bonn, and R. Liang, Physical Review Letters **83**, 3277 (1999).

[57] C.P. Bidinosti and W.N. Hardy, Review of Scientific Instruments **71**, 3816 (2000).

[58] J. Buan, B.P. Stojkovic, N.E. Israeloff, A.M. Goldman, C.C. Huang, O.T. Valls, J.Z. Liu and R. Shelton, Physical Review Letters **72**, 2632 (1994); J. Buan, B.P. Stojkovic, N.E. Israeloff, A.M. Goldman, C.C. Huang, O.T. Valls, T. Jacobs, S. Sridhar, C.R. Smith, H.D. Yang, J.Z. Liu and R. Shelton, Physical Review B. **54**, 7462 (1996).

[59] A. Bhattacharya, D.E. Grupp, A.M. Goldman and U. Welp, Applied Physics Letters **69**, 1792 (1996).

[60] A. Bhattacharya, I. Žutič, O.T. Valls, A.M. Goldman, U. Welp, and B. Veal, Physical Review Letters **82**, 3132 (1999).

[61] T. Dahm and D.J. Scalapino, Journal of Applied Physics **82**, 464 (1997).

[62] R. B. Hammond, E. R. Soares, B.A. Willemsen, T. Dahm, D. J. Scalapino and J. R. Schrieffer, Journal of Applied Physics **84**, 5662 (1998).

[63] T. Dahm, D.J. Scalapino and B.A. Willemsen, Journal of Applied Physics **86**, 4055 (1999).

[64] J. Orenstein, J. Bokor, E. Budiarto, J. Corson, R. Mallozzi, I. Bozovic and J.N. Eckstein, Physica **282C-287C**, 252 (1997).

[65] B.A. Willemsen, K.E. Kihlstrom and T. Dahm, Applied Physics Letters **74**, 753 (1999).

[66] B.A. Willemsen, K.E. Kihlstrom, T. Dahm, D.J. Scalapino, B. Gowe, D.A. Bonn and W.N. Hardy, Physical Review B **58**, 6650 (1998).

[67] J.C. Booth, J.A. Beall, D.A. Rudman, L.R. Vale and R.H. Ono, Journal of Applied Physics **86**, 1020 (1999).

[68] J.H. Classen, J.C. Booth, J.A. Beall, D.A. Rudman, L.R. Vale and R.H. Ono, Applied Physics Letters **74**, 4023 (1999).

[69] H. Hoshizaki, N. Sakakibara and Y. Ueno, Journal of Applied Physics **86**, 5788 (1999).

[70] M. I. Tsindlekht, E. B. Sonin, M. A. Golosovsky, D. Davidov, X. Castel, M. Guilloux-Viry, and A. Perrin, Physical Review B **61**, 1596 (2000).

[71] W.N. Hardy, S. Kamal, and D.A. Bonn, in *The Gap Symmetry and Fluctuations in High-T_c Superconductors*, ed. J. Bok, G. Deutscher, D. Pavuna, and S.A. Wolf (Plenum Press, New York, 1998).

[72] D. Shoenberg, Proceedings of the Cambridge Philosophical Society **33**, 559 (1937).

[73] Fedor Gömöry, Superconductor Science and Technology **10**, 523 (1997). And references therein.

[74] T. Ishida and R. B. Goldfarb, Physical Review B **41**, 8937 (1990).

[75] M. Nikolo, American Journal of Physics **63**, 57 (1995).

[76] S. Sridhar and W.L. Kennedy, Review of Scientific Instruments **59**, 531 (1988). D.L. Rubin, K. Green, J. Gruschus, J. Kirchgessner, D. Moffat, H. Padamsee, J. Sears, Q.S. Shu, L.F. Schneemeyer, and J.V. Waszczak, Physical Review B **38**, 6538 (1988).

[77] Cernox^{TM} resistor, model CX-1050-BG, was purchased from Lake Shore Cryotronics, Inc. of 575 McCorkle Boulevard, Westerville, Ohio 43082 USA.

[78] S.T. Smith and D.G. Chetwynd, *Foundations of Ultraprecision Mechanism Design* (Gordon and Breach Science Publishers, Philadelphia, 1992), p. 102.

[79] Sapphire rod was purchased from Crystal Systems, Inc. of 27 Congress Street, Salem, Massachusetts 01970 USA. The sapphire was certified to be of optical quality, 99.996% pure, and with crystal axis $\pm 2°$ along the rod. Precision grinding of the form was done by Imetra, Inc. of 200 Clearbrook Road, Elmsford, NY 10523 USA.

[80] The niobium wire, 0.003″ in diameter with formvar coating, was purchased from Supercon, Inc. of 830 Boston Turnpike, Shrewsbury, MA 01545 USA. The copper wire, 99.99% pure, 0.004″ in diameter with formvar coating, was purchased from California Fine Wire Co. of Grover Beach, CA 93433 USA.

[81] The core is made from VITROVAC^{TM} 6025 F a high permeability material produced by Vacuumschmelze GMBH of Grüner Weg 37, P.O. Box 2253, D-6450 Hanau 1, Germany.

[82] R. B. Goldfarb and J. V. Minervini, Review of Scientific Instruments **55**, 761 (1984).

[83] A. F. Khoder and M. Couach, Cryogenics **31**, 763 (1991).

[84] D.N. Basov, R. Liang, D.A. Bonn, W.N. Hardy, B. Dabrowski, M. Quijada, D.B. Tanner, J.P. Rice, D.M. Ginsberg and T. Timusk, Physics Review Letters **74**, 598 (1995). This reference gives $\lambda_{a,b}(T = 0) = 1600, 1030$ Å for optimally doped $YBa_2Cu_3O_{6.95}$ single crystals.
J.L. Tallon, C. Bernhard, U. Binninger, A. Hofer, G.V.M. Williams, E.J. Ansaldo, J.I. Budnick and Ch. Niedermayer, Physical Review Letters **74**, 1008 (1995). This reference gives $\lambda_{a,b}(T = 0) = 1600, 800$ Å for overdoped $YBa_2Cu_3O_{6.993}$ single crystals.

[85] S. Kamal, R. Liang, A. Hosseini, D.A. Bonn, and W.N. Hardy, Phys. Rev. B **58**, R8933 (1998).

[86] D.S. Fisher, M.P.A. Fisher, and D.A. Huse, Phys. Rev. B **43**, 130 (1991), especially section IV.

[87] The polishing pads were purchased from Buehler of 41 Waukegan Road, Lake Bluff, IL 60044 USA.

[88] Ruixing Liang, *private communication.*

[89] A. Erb, E. Walker and R. Flükiger, Physica C **245**, 245 (1995); Physica C **258**, 9 (1996).

[90] *Encyclopedia of Materials Science and Engineering. Supplementary volume*, ed. R. W. Cahn and M. B. Bever (Pergamon Press, New York, 1986), pp. 1, Volume 1.

[91] P.J. Hirschfeld, *private communication*, 1999.

[92] J.R. Cooper, *preprint* cond-mat/0008270 (2000).

[93] Mary L. Boas, *Mathematical Methods in the Physical Sciences*, 2nd edition (John Wiley & Sons, Singapore, 1983).

Appendix A

Solutions to the Nonlinear London Equation

In general one seeks a solution to the differential equation (Equation 3.8)

$$\nabla^2 \boldsymbol{v}_s = \frac{\mu_o n_s e^2}{m} \boldsymbol{v}_s (1 - \alpha \left| \boldsymbol{v}_s \right| - \beta \boldsymbol{v}_s^2 - ...)$$

with the appropriate boundary conditions. For the semi-infinite superconductor (occupying the positive z half-space) in an uniform applied field H, this reduces to an equation of the form $v_s'' = \lambda^{-2} f(v_s)$ with $v_s' = eH/c$ at the surface and $v_s' = v_s = 0$ as $z \to \infty$. The general method [93] for solving a differential equation of the form $y'' = f(y)$ is as follows: multiply by y' to give $y' \mathrm{d}y' = f(y)\mathrm{d}y$, and following integration $\frac{1}{2} y'^2 = \int f(y)\mathrm{d}y + C$. Rearranging for y' and intergrating for a second time gives the appropriate solution subject to the boundary conditions. The pertinent details of this calculation for both the s-wave and d-wave case are given below.

A.1 s-wave Superconductor

From Equation 3.12 for the nonlinear current in an s-wave superconductor, the nonlinear London equation for the semi-infinite slab becomes

$$\frac{\mathrm{d}^2 v_s}{\mathrm{d}z^2} = \frac{1}{\lambda^2} v_s \left[1 - \beta \left(\frac{v_s}{v_c} \right)^2 \right] \tag{A.1}$$

The first integration gives

$$\frac{1}{2} \left(\frac{\mathrm{d}v_s}{\mathrm{d}z} \right)^2 = \frac{1}{\lambda^2} v_s^2 \left[\frac{1}{2} - \frac{\beta v_s^2}{4 v_c^2} \right] + C \tag{A.2}$$

where the constant of integration C must obviously be equal to zero to satisfy the condition that v_s goes to zero deep inside the superconductor. Rearranging for v_s' gives

$$\frac{\mathrm{d}v_s}{\mathrm{d}z} = -\frac{1}{\lambda}v_s\left[1-\frac{\beta v_s^2}{4v_c^2}\right] \tag{A.3}$$

where only the negative root is chosen (as v_s must decay), and, in the limit of small v_s, the term $\sqrt{1-\beta v_s^2/2v_c^2}$ has been approximated as $(1-\beta v_s^2/4v_c^2)$. Integrating for the second time and rearranging for v_s gives

$$v_s = v\left[\frac{\beta v^2}{4v_c^2}+\left(1-\frac{\beta v^2}{4v_c^2}\right)e^{2z/\lambda}\right]^{-1/2} \tag{A.4}$$

where v is the superfluid velocity at the surface. The magnetic field inside the sample is given by

$$\begin{aligned} H(z) &= \frac{c}{e}\frac{\mathrm{d}v_s}{\mathrm{d}z} \\ &= -\frac{cv}{e\lambda}\left(1-\frac{\beta v^2}{4v_c^2}\right)e^{2z/\lambda}\left[\frac{\beta v^2}{4v_c^2}+\left(1-\frac{\beta v^2}{4v_c^2}\right)e^{2z/\lambda}\right]^{-3/2} \end{aligned} \tag{A.5}$$

At $z=0$, the boundary condition requires that the field at the surface of the superconductor is $H = -(cv/e\lambda)\,(1-\beta v^2/4v_c^2)$, which gives $v \simeq -(e\lambda H/c)\,(1-\beta(e\lambda H/cv_c)^2)$ for small v and the final solution can be written as

$$H(z) \simeq He^{2z/\lambda}\left[\frac{\beta H^2}{H_o^2}+\left(1-\frac{\beta H^2}{H_o^2}\right)e^{2z/\lambda}\right]^{-3/2} \tag{A.6}$$

where the constant $H_o = 2cv_c/e\lambda$. It is clear that in the limit $H \to 0$ the solution to the linear London equation, $H(z) = He^{-z/\lambda}$, is recovered.

In the original work on the NLME [28, 30], the penetration depth is defined by the initial rate of decay of the magnetic field inside the sample, and is given as $\lambda^{-1} \equiv -H^{-1}\,\mathrm{d}H(z)/\mathrm{d}z|_{z=0}$. For a volume exclusion experiment, a more appropriate definition is $\lambda \equiv H^{-1}\int_0^\infty H(z)\,dz$, and is the one used in this thesis. Using Equation A.6, the former definition gives a field dependent penetration depth,

$$\lambda(T,H) = \lambda(T)\left\{1 + 3\beta(T)\left[\frac{H}{H_o}\right]^2\right\} \tag{A.7}$$

while the latter definition gives the result

$$\lambda(T,H) = \lambda(T)\left\{1 + \beta(T)\left[\frac{H}{H_o}\right]^2\right\} \tag{A.8}$$

which is a factor of three smaller than the Yip and Sauls value. However, it is shown in Appendix B that an ac measurement (of a quadratic $\lambda(H)$) will result in a signal that is three times as large as a dc measurement. Therefore, the expected coefficient from a measurement such as ours will be numerically equivalent to the Yip and Sauls value.

A.2 d-wave Superconductor

From Equation 3.14 for the nonlinear current in an $d_{x^2-y^2}$ superconductor, the nonlinear London equation for the semi-infinite slab becomes[1]

$$\frac{\mathrm{d}^2 v_s}{\mathrm{d}z^2} = \frac{1}{\lambda^2} v_s \left[1 - \alpha\frac{|v_s|}{v_o}\right] \tag{A.9}$$

The first integral gives

$$\frac{\mathrm{d}v_s}{\mathrm{d}z} = -\frac{1}{\lambda} v_s \sqrt{1 - \frac{\alpha v_s}{3v_o}} \tag{A.10}$$

and upon integrating again, the superfluid velocity is

$$v_s = -\frac{3\alpha}{v_o}\left(1 - \tanh^2(Z)\right) \tag{A.11}$$

where $Z = \tanh^{-1}\sqrt{1 - 2\alpha v/3v_o} + z/2\lambda$ and v is the value of v_s at the surface. Using the identity $\tanh(x+y) = (\tanh(x) + \tanh(y))/(1 + \tanh(x)\tanh(y))$, this can be rearranged

[1]This equation is only strictly true for fields applied along a node or antinode where there is no component of the backflow current perpendicular to v_s. A slightly more general solution to the nonlinear London equation (for any orientation of the field in the plane of a $d_{x^2-y^2}$ superconductor) can be found in Appendix B of Reference [30].

to give

$$v_s = -\frac{v}{\frac{\alpha v}{3v_o} + \left(1 - \frac{\alpha v}{3v_o}\right)\cosh(z/\lambda) + \sqrt{1 - \frac{2\alpha v}{3v_o}}\sinh(z/\lambda)} \tag{A.12}$$

Taking the derivative $\frac{c}{e}dv_s/dz$ gives the magnetic field inside the sample as

$$H(z) = \frac{cv}{e\lambda}\frac{\left(1 - \frac{\alpha v}{3v_o}\right)\sinh(z/\lambda) + \sqrt{1 - \frac{2\alpha v}{3v_o}}\cosh(z/\lambda)}{\left[\frac{\alpha v}{3v_o} + \left(1 - \frac{\alpha v}{3v_o}\right)\cosh(z/\lambda) + \sqrt{1 - \frac{2\alpha v}{3v_o}}\sinh(z/\lambda)\right]^2} \tag{A.13}$$

and from this the boundary condition $H(0) = H = (cv/e\lambda)\sqrt{1 - 2\alpha v/3v_o}$ is found. In the limit of small H, the boundary condition can be written as $H \simeq (cv/e\lambda)(1 - \alpha v/3v_o)$ or $v \simeq (e\lambda H/c)(1 + \alpha e\lambda H/3cv_o)$, and field inside the sample becomes

$$H(z) \simeq He^{-z/\lambda}\left[1 + 2\alpha\frac{|H|}{H_o}\left(1 - e^{-z/\lambda}\right)\right] \tag{A.14}$$

where $H_o = 3cv_o/2e\lambda$. Again, the linear London equation is recovered in the limit $H \to 0$.

Using Equation A.14, the differential definition of the penetration depth gives

$$\lambda(T,H) = \lambda(T)\left\{1 + \alpha\frac{|H|}{H_o}\right\} \tag{A.15}$$

while the integral definition gives the result

$$\lambda(T,H) = \lambda(T)\left\{1 + \frac{\alpha}{2}\frac{|H|}{H_o}\right\} \tag{A.16}$$

For a d-wave superconductor then, the integral penetration depth is a factor of two smaller than the Yip and Sauls result. In this case, Appendix B shows that an ac measurement (of the linear $\lambda(H)$) will result in a signal that is two times as large as a dc measurement. Again the coefficient we would measure in our apparatus is numerically equivalent to the Yip and Sauls value.

Appendix B

Magnetic Moment of a Flat Slab in a Parallel Field

Consider a conducting slab of thickness t in a parallel uniform magnetic field B_o. If the z direction is taken to be along the thickness of the slab, with $z = \pm t/2$ defining the edges of the slab, then in light of Equation 2.4 the field inside the slab must vary as

$$B(z) = C\left(e^{(z-t/2)\gamma} + e^{-(z+t/2)\gamma}\right)$$

subject to the boundary condition $B(\pm t/2) = B_o$. A little algebra determines the coefficient C and the field inside the slab can be shown to be

$$B(z) = B_o \cosh{(\gamma z)}/\cosh{(\gamma t/2)} \tag{B.1}$$

The magnetization M of the slab can be written as $M = B/\mu_o - H$, where for this geometry H is a constant equal to B_o/μ_o. The magnetic moment is given as $m = \int M \mathrm{d}V$, and substituting from above is equal to

$$\begin{aligned} m &= \int (B - B_o)/\mu_o \,\mathrm{d}V \\ &= \frac{AB_o}{\mu_o}\int_{-t/2}^{t/2} \left(\cosh{(\gamma z)}/\cosh{(\gamma t/2)} - 1\right)\mathrm{d}z \\ &= -\frac{VB_o}{\mu_o}\left(1 - 2/\gamma t \tanh{(\gamma t/2)}\right) \end{aligned} \tag{B.2}$$

where V is the sample volume and A its cross-sectional area. This is identical to the result quoted in Chapter 4, except that it has been generalized to the case where the propagation constant γ is complex.

B.1 General Calibration of the ac Susceptometer

For completeness, a general expression for the ac susceptometer signal that includes losses due to the normal fluid response is developed here. Losses associated with the mixed state are not covered by this analysis. As a practical matter, at $f = 12$ kHz, the losses in single crystals of $YBa_2Cu_3O_{7-\delta}$ are very small except in a narrow region around T_c, and the simple relationship of Equation 4.8 to determine $\Delta\lambda$ remains valid until a few tenths of a Kelvin below T_c . As the sample goes through T_c , the contribution from σ_1 cannot be ignored and the full solution given below must be used to extract λ and δ.

As discussed in Section 2.3, a superconductor has a complex conductivity $\sigma = \sigma_1 - i\sigma_2$ and the behavior of a magnetic field at its surface is characterized by the propagation constant $\gamma = \sqrt{1/\lambda^2 + 2i/\delta^2}$. At sufficiently low frequency ω, and assuming local electrodynamics, $\delta = \sqrt{2/\mu_o\omega\sigma_1}$ and $\lambda = \sqrt{1/\mu_o\omega\sigma_2}$. In the superconducting state, λ is just the penetration depth of the magnetic field and δ characterizes losses associated with σ_1 (the normal fluid). Above T_c, λ diverges with the disappearance of σ_2 (the superfluid) and δ is just the normal state skin depth.

To develop a general expression for the ac susceptometer signal that includes losses due to the normal fluid response, one starts again with the signal voltage proportional to dm/dt. A change in the sample's moment Δm is detected as the voltage

$$\Delta v(t) = \frac{1}{k} i e^{i\omega t} \Delta m$$

where $1/k$ is the calibration constant to be determined. If changes are measured from the base temperature, zero dc field, setting then

$$\Delta v(t) = \frac{1}{k} \left(i \cos(\omega t) - \sin(\omega t) \right) \left[2\lambda_o/t \tanh(t/2\lambda_o) - 2/\gamma_2 t \tanh(\gamma_2 t/2) \right]$$

using the definition of m from Equation B.2 and letting $\gamma_1 = 1/\lambda_1(T) \simeq 1/\lambda_o$, noting that at low frequencies the loss in the superconductor is negligible so the propagation constant at the initial point γ_1 is the reciprocal of the penetration depth at this point $\lambda_1(T)$, which is essentially just the zero temperature penetration depth λ_o. Now, after absorbing the constant term $(-2/t)$ into $1/k$, the real part of the voltage signal can be written as

$$\begin{aligned}\Delta v(t) &= \frac{-1}{k}\cos(\omega t)\,\mathrm{Im}\left[1/\gamma_2 \tanh(t\gamma_2/2)\right] \\ &\quad + \frac{1}{k}\sin(\omega t)\left\{\mathrm{Re}\left[1/\gamma_2 \tanh(t\gamma_2/2)\right] - \lambda_0 \tanh(t/2\lambda_0)\right\}\end{aligned}$$

The first term is in-phase with the drive field, but remembering that $v(t) \propto \mathrm{d}m/\mathrm{d}t$ it is clear that this term represents the out-of-phase response of the sample, which is due to dissipation. The second term represents the inductive response of the sample. The voltages measured by the two channels of the lock-in will be

$$\mathrm{X} = \frac{-1}{k}\mathrm{Im}\left[1/\gamma_2 \tanh(t\gamma_2/2)\right] \tag{B.3}$$

$$\mathrm{Y} = \frac{1}{k}\left\{\mathrm{Re}\left[1/\gamma_2 \tanh(t\gamma_2/2)\right] - \lambda_0 \tanh(t/2\lambda_0)\right\} \tag{B.4}$$

Equations B.3 and B.4 are a generalization of Equation 4.6 and must be solved simultaneously to extract λ and δ. The phase setting and calibration follow exactly the discussion in Section 4.4, and given the same conditions on λ_0 and t, the calibration constant k is still given by Equation 4.7.

B.2 The Nonlinear Magnetic Moment

Well below T_c and at the low frequency (12 kHz) of the ac susceptometer, losses are negligible in a superconductor and one can ignore the contribution of σ_1 to the magnetic moment. Furthermore, for the average sized $YBa_2Cu_3O_{7-\delta}$ single crystal $\lambda(T)$ will be much smaller than the crystal thickness t. This is the limit in which all NLME experiments were done, and in this regime the magnetic moment can be written as

$$m = -H(V - 2A\lambda)$$

where λ is a function of H. The magnetic moment is calculated below for an applied field of the form $H(t) = H + H_1 \cos(\omega t)$, a dc field superimposed by a single tone ac field,such as that used in the ac susceptometer. Also, for the purpose of developing the idea of intermodulation, the moment is magnetic moment is worked out for a field with two tones of the form $H(t) = H_1 (\cos(\omega_1 t) + \cos(\omega_2 t))$. This will be done for the case of both linear and quadratic changes in λ with H.

Case 1: The linear $\lambda(H)$

Consider the penetration depth of Equation 3.15, $\lambda(H) = \lambda\{1 + \alpha |H| / H_o\}$. For a dc field plus single tone, the magnetic moment (in the region $H > H_1$) is

$$\begin{aligned} m &= -H\left(V - 2A\lambda - \frac{\alpha A\lambda |H|}{H_o}\right) + \frac{\alpha A\lambda H_1^2}{H_o} \\ &\quad -H_1\left(V - 2A\lambda - \frac{4\alpha A\lambda |H|}{H_o}\right)\cos(\omega t) \\ &\quad +\frac{\alpha A\lambda H_1^2}{H_o}\cos(2\omega t) \end{aligned} \tag{B.5}$$

The last coefficient in the $\cos(\omega t)$ term is the quantity that would be measured by the technique used in this thesis. Notice that it is a factor of 2 larger than the corresponding dc term. One could also measure the coefficient of the second harmonic $\cos(2\omega t)$ with the ac susceptometer, however sweeping the magnitude of H_1 rather than H_o would present its own set of experimental difficulties and the expected signal here would only be half of what will be seen at the fundamental.

For a field with two tones of equal magnitude, $H(t) = H_1\left(\cos(\omega_1 t) + \cos(\omega_2 t)\right)$, one can write

$$|H(t)| = 2H_1 \cdot |\cos(\omega_o t)| \times |\cos(\omega_d t)|$$

where $\omega_1 = \omega_o - \omega_d$ and $\omega_2 = \omega_o + \omega_d$. In this form, each absolute value term can be written in a Fourier series, which then allows one to write m as an expansion of cosine terms. The final result is given below, rewritten in terms of the original variables ω_1 and ω_2; only the fundamental, third order intermodualtion, and third harmonic terms are shown respectively.

$$\begin{aligned} m \;\simeq\; & -H_1\left(V - 2A\lambda - \frac{256\alpha A\lambda H_1}{9\pi H_o}\right)\cos(\omega_1 t), \cos(\omega_2 t) \\ & + \frac{256\alpha A\lambda H_1^2}{45\pi H_o}\cos((2\omega_1 - \omega_2)t), \cos((2\omega_2 - \omega_1)t) \\ & + \frac{64\alpha A\lambda H_1^2}{45\pi H_o}\cos(3\omega_1 t), \cos(3\omega_2 t) \end{aligned} \tag{B.6}$$

The coefficients of the third order products are quadratic in H_1; this is referred to as $2:1$ behaviour.

Case 2: The quadratic $\lambda(H)$

Consider the penetration depth of Equation 3.13, $\lambda(H) = \lambda\left\{1 + \beta(T)H^2/H_o^2\right\}$. For a dc field plus single tone, the magnetic moment is

$$\begin{aligned} m \;=\; & -H\left(V - 2A\lambda - \frac{2\beta A\lambda H^2}{H_o^2} - \frac{3\beta A\lambda H_1^2}{H_o^2}\right) \\ & -H_1\left(V - 2A\lambda - \frac{6\beta A\lambda H^2}{H_o^2} - \frac{3\beta A\lambda H_1^2}{2H_o^2}\right)\cos(\omega t) \\ & + \frac{3\beta A\lambda H H_1^2}{H_o^2}\cos(2\omega t) + \frac{\beta A\lambda H_1^3}{2H_o^2}\cos(3\omega t) \end{aligned} \tag{B.7}$$

The third coefficient in the $\cos(\omega t)$ term is the quantity that would be measured by the technique used in this thesis. Here, it is a factor of 3 larger than the corresponding dc term. Again, there is no apparent advantage to measuring the nonlinear effects at higher harmonics.

For a field with two tones of equal magnitude, the fundamental, third order intermodulation, and third harmonic terms of the magnetic moment are

$$\begin{aligned} m &= -H_1\left(V - 2A\lambda - \frac{9\beta A\lambda H_1^2}{2H_o^2}\right)\cos(\omega_1 t), \cos(\omega_2 t) \\ &\quad + \frac{3\beta A\lambda H_1^3}{2H_o^2}\cos((2\omega_1 - \omega_2)t), \cos((2\omega_2 - \omega_1)t) \\ &\quad + \frac{\beta A\lambda H_1^3}{2H_o^2}\cos(3\omega_1 t), \cos(3\omega_2 t) \end{aligned} \tag{B.8}$$

Here the third order products show $3:1$ behaviour; their coefficients are cubic in H_1.